A Comprehensive Study of Broad Absorption Line Quasars: I. Prevalence of He I* Absorption Line Multiplets in Low-Ionization Objects

Wen-Juan Liu[1,2], Hongyan Zhou[2,1], Tuo Ji[2,1], Weimin Yuan[3], Ting-Gui Wang[1], Ge Jian[4], Xiheng Shi[2], Shaohua Zhang[2], Peng Jiang[1,2], Xinwen Shu[5], Huiyuan Wang[1], Shu-Fen Wang[1,2], Luming Sun[1,2], Chenwei Yang[1], Bo Liu[1,2], and Wen Zhao[1]

ABSTRACT

Neutral Helium multiplets, He I* $\lambda\lambda 3189, 3889, 10830$ are very useful diagnostics to the geometry and physical conditions of the absorbing gas in quasars. So far only a handful of He I* detections have been reported. Using a newly developed method, we detected He I*$\lambda 3889$ absorption line in 101 sources of a well-defined sample of 285 Mg II BAL quasars selected from SDSS DR5. This has increased the number of He I* BAL quasars by more than one order of magnitude. We further detected He I*$\lambda 3189$ in 50% (52/101) quasars in the sample. The detection fraction of He I* BALs in Mg II BAL quasars is $\sim$35% as a whole, and increases dramatically with increasing spectral signal-to-noise ratios, from $\sim$18% at S/N $\leq$ 10 to $\sim$93% at S/N $\geq$ 35. This suggests that He I* BALs could be detected in most Mg II LoBAL quasars, provided spectra S/N is high enough. Such a surprisingly high He I* BAL fraction is actually predicted from photo-ionization calculations based on a simple BAL model. The result indicates that He I* absorption lines can be used to search for BAL quasars at low-z, which cannot be identified by ground-based optical spectroscopic survey with commonly seen UV absorption lines. Using He I* $\lambda 3889$, we discovered 19 BAL quasars at $z < 0.3$ from available SDSS spectral database. The fraction of He I* BAL quasars is similar to that of LoBAL objects.

Subject headings: galaxies: active — quasars: absorption lines — quasars: general

[1]Key Laboratory for Research in Galaxies and Cosmology, Department of Astronomy, University of Sciences and Technology of China, Chinese Academy of Sciences, Hefei, Anhui 230026, China, zoey@mail.ustc.edu.cn

[2]Polar Research Institute of China, 451 Jinqiao Rd, Shanghai 200136, China, zhouhongyan@pric.org.cn, ji-tuo1982@gmail.com

[3]National Astronomical Observatories, Chinese Academy of Sciences, 20A Datun Road, Beijing 100012, China

[4]Astronomy Department, University of Florida, 211 Bryant Space Science Center, P.O. Box 112055, Gainesville, FL 32611, USA

[5]CEA Saclay, DSM/Irfu/Service d'Astrophysique, Orme des Merisiers, 91191 Gif-sur-Yvette Cedex, France

1. Introduction

Broad absorption line quasars are a small yet important population of active galactic nuclei (AGNs) that have a continuous broad absorption trough spanning a large range of velocities up to several times 10^4 km s^{-1} (Weymann et al. 1991; Trump et al. 2006; Gibson et al. 2009). The broad absorption lines are generally blueshifted with respect to the systematic redshift of their emission counterparts by up to 0.1-0.2 of light speed (e.g. Weymann et al. 1991; Korista et al. 1992, 1993; Hamann et al. 2013). Traditionally, BAL quasars are classified into three subcategories depending on which absorption features are seen. Hi-ionization BAL quasars (HiBALs) show absorption in N V $\lambda\lambda 1238, 1242$, Si IV $\lambda\lambda 1393, 1402$ and C IV $\lambda\lambda 1548, 1550$, and comprise about 85% of the BAL quasars. Low-ionization quasars (LoBALs) show, besides all the HiBAL features, absorption troughs in low-ionization species like Mg II $\lambda\lambda 2796, 2803$, Al III $\lambda\lambda 1854, 1862$ (hereafter N V, Si IV, C IV, Mg II, Al III), and comprise about 15% of the whole BAL population (e.g. Tolea et al. 2002; Reichard et al. 2003b; Hewett & Foltz 2003). Additionally, a rare class of LoBAL termed FeLoBAL quasars, show absorption features arising from excited-state of Fe II.

BALs are generally believed to be associated with AGN outflows from an accretion disk (e.g. Murray et al. 1995). Outflows may carry away huge amounts of material, energy, and angular momentum, and are believed to be one of the most important feedback processes that connects AGNs and their host galaxies (e.g. Di Matteo et al. 2005; Elvis 2006; Dunn et al. 2010; Farrah et al. 2012). Regarding the origin of BALs in quasars, there are two theoretical scenarios. The first is that BAL quasars are essentially normal quasars viewed along a line of sight that penetrates the outflow gas (Elvis 2000). The second is an evolution scenario, in which BALs are associated with youthful quasars enshrouded heavily with gas and dust (e.g. Williams et al. 1999). Observationally, multi-wavelength comparisons find basically no intrinsic difference between BALs and non-BALs, except that BAL quasars, particularly the LoBAL ones, typically have redder ultraviolet (UV) continua than non-BAL quasars (Weymann et al. 1991; Reichard et al. 2003b; Lewis et al. 2003; Gallagher et al. 2007). This fact is consistent with both the orientation and evolutionary scenarios. Recently, evidence has mounted that LoBAL quasars, and FeLoBAL ones in particular, are highly reddened objects with high IR luminosities, associated with ultraluminous infrared galaxies (ULIRGs) in some way (Farrah et al. 2007, 2009; Glikman et al. 2012). This leads to the interpretation that LoBALs may be just at a transition phase of the evolutionary sequence from major mergers of galaxies to star-bursting ULIRGs, dust-enshrouded BAL quasars, and finally to unobscured luminous quasars (e.g. Sanders et al. 1988; Gregg et al. 2002; Shen & Ménard 2012). Therefore, the study of BALs has important implications to understanding both the structure and emission/absorption physics of AGNs and the co-evolution of AGNs and their host galaxies.

Absorption lines provide abundant information about the outflows of quasars, such as velocity, column density, ionization state and density, and furthermore distances from the central black

holes and even kinetic energy. Column densities could be determined by simply integrating over the apparent optical depth profile for unsaturated absorption lines (e.g. Savage & Sembach 1991). Two or more lines from the same lower level are very helpful to jointly determine the column density and covering factor of the outflow (e.g. Hamann 1997; Arav et al. 2005). However, the commonly seen absorption lines, such as C IV and Mg II are easily saturated when the ion column densities are high. Furthermore the wavelength separations of the C IV and Mg II doublets are less than 10 Å, so blending is a serious problem for BALs. By contrast, the He I* absorption lines offer a number of advantages in determining the physical conditions of outflow gas. The metastable $2s$ state in the Helium triplet, He I*, which is populated via recombination of He$^+$ ions, are photo-ionized by photons with energies of $h\nu \geq 24.56$ eV. He I* has multiple upward transitions in a wide wavelength span from UV to NIR, which are easy to observe. The strongest three transitions are 10830, 3889 and 3189 Å from metastable state to 2p, 3p, 4p state respectively. Since these transitions are widely separated, there is no blending problem. Compared to C IV and Mg II ions, the He I* atoms have much smaller abundance, and the optical depth, $\tau \propto \lambda f_{ik} N_{ion}$, is much smaller than those of C IV and Mg II ions. Therefore the He I* may remain optically thin even when C IV and Mg II lines are saturated (Leighly et al. 2011). The He I* absorption lines are also sensitive to the ionization state of the outflow gas, and thus they can, combined with other lines, set a tight constraint on the outflow (e.g. Arav et al. 2001; Ji et al. 2014). Because the wavelength coverage of the He I* lines are between NUV and NIR, it is convenient to search more low redshift BAL AGNs via the He I* absorption lines, which can be potentially used to study the host galaxy properties of BALs quasars.

However, the valuable He I* absorption lines have received little attention for a long time. Known He I* BAL quasars are very rare to date, with only eleven being reports in the literature: Mrk 231 (e.g., Rudy et al. 1985; Leighly et al. 2014), FBQS J1151+3822 (Leighly et al. 2011; Lucy et al. 2014), NGC 4151 (e.g., Anderson 1974; Storchi-Bergmann et al. 2009), NVSS J2359−1241 (Brotherton et al. 2001; Arav et al. 2001, 2008; Korista et al. 2008; Bautista et al. 2010), AKARI J1757+5907 (Aoki et al. 2011), LBQS 1206+1052 (Ji et al. 2012), IRAS 14026+4341 (Jiang et al. 2013), SDSS J080248.18+551328.9 (Ji et al. 2014), SDSS J030000.56+004828.0 (Hall et al. 2002, 2003), SDSS J151249.29+111929.36 (Borguet et al. 2012, 2013), SDSS J110645.05+193929.1 (Borguet et al. 2013)), which are summarized in Table 1. Having investigating these well studied objects, we noticed with surprise that all of these show the Mg II absorption troughs at the corresponding velocities of He I*. This suggests that the He I* and Mg II absorption lines may have some physical connections. Given the aforementioned merits of He I* absorption, it is important to find more He I* BAL quasars, yet we even don't know whether He I* BAL quasars are intrinsically rare or not. In light of these considerations, as a first step, we carry out a systematic search campaign for the He I*λ3889 absorption line among Mg II LoBAL quasars.

This paper is arranged as follows. In §2, a parent sample of Mg II LoBAL quasars is con-

structed and the pair-matching method is introduced. We then adopt this method to compile a He I* λ3889 sample. In §3, we present discussion on the fraction of the He I* absorption line in Mg II BALs, which is found to be strongly dependent on the S/N of the spectra. In §4, we calculate a series of photoionization models to investigate the physical conditions of the He I* absorption gas and give a physical explanation to the high fraction of the He I* in Mg II BALs. We show one example of determining the physical condition of the outflow gas by jointly using He I*$\lambda\lambda$10830, 3889, 3189 lines. We also compile a sample of 19 low-z ($z < 0.3$) BAL candidates selected by detecting the He I*λ3889 absorption line. The summary and future works are given in §5. The details of supportive NIR observations and other results are described in Appendix. Throughout this work we use a cosmology with $H_0 = 70$ km s^{-1} Mpc^{-1}, $\Omega_M = 0.3$, and $\Omega_\Lambda = 0.7$.

2. Sample of He I*λ3889 BAL Quasars

2.1. Existing samples of Mg II LoBAL quasars

We start with existing samples in the literature of Mg II BAL quasars at $0.4 \leq z \leq 1.35$. The redshift cutoffs are chosen such that both He I*λ3889 and Mg II fall in the wavelength coverage of the SDSS spectrograph (3800–9200Å), which enables us to use Mg II BALs as a reference in this first systematic search for He I*λ3889 BALs.

There were more studies on the C IV BAL than on Mg II BAL in previous studies. Among the existing BAL samples, Trump et al. (2006, hereafter T06), Gibson et al. (2009, hereafter G09) and Zhang et al. (2010, hereafter Z10) have conducted systematic searches for Mg II BALs in the SDSS data set. T06 identified 4784 BAL quasars in SDSS DR3 quasar catalog, and G09 identified 5039 from the SDSS DR5, in C IV and/or Mg II. Specifically aimed at Mg II BALs, Z10 compiled 68 Mg II BAL quasars in the SDSS DR5 at $0.4 \leq z \leq 0.8$. Those samples were compiled by using different spectral fitting procedures and somehow different BAL definitions (see Appendix A.1 for the detail). We find considerable discrepancies among the three samples: 32% objects of T06, 19.5% of G09, and 11.4% of Z10, respectively, are not included in the other two samples, reflecting to what a extent of the incompleteness of the samples could be caused by their different selection procedures and criteria. We combined these samples into a merged Mg II BAL quasar sample, from which we build our parent sample of this work. Selection biases in the individual samples, which are partially complementary to one another, are also reduced to some extent in the combined sample.

The main uncertainty caused by the selection procedure lies in determining the unabsorbed spectrum (the intrinsic quasar continuum and/or emission lines). There are basically two schemes in the literature. One scheme is to use some kinds of quasar composite spectra to model the un-

absorbed spectrum (e.g., Reichard et al. 2003a, T06) in light of the striking global similarity of ultraviolet/optical spectra of most quasars (e.g., Richards et al. 2001; Vanden Berk et al. 2001). With the advantages of simplicity and fast speed, the disadvantage of this scheme is also obvious: on the wavelength scale as far as the BAL features are concerned, there are considerable object-to-object variations in the quasar continuum shape, broad emission line profile, iron emission multiplets (pseudo-continuum) and Balmer continuum shape, etc., which cannot be incorporated in a single composite spectrum. The other scheme is to recover the unabsorbed continuum and emission lines via χ^2–minimization fitting with (analytic) models (e.g., Tolea et al. 2002, G09, Z10). In this case, the unabsorbed UV/optical continuum is modeled with a single or a broken power law or polynomial, emission lines with Gaussian(s) or Lorentzian(s), and iron emission with tabulated or analytic templates (e.g. Boroson & Green 1992; Dong et al. 2011). The advantages are the flexibility of fitting individual spectral components, as well as its quick speed. Yet there are still several disadvantages. For example, some spectral components (such as Balmer continua) are hard to constrain by fitting (cf. Wang et al. 2009); particularly, the Fe II multiplet emissions are considerably diverse among quasars and are hard to be fitted well in many cases using the existing Fe II templates, because those templates are all based on the famous NLS1, I Zw 1 (see a recent discussion in Dong et al. 2011). To sum up, though the two traditional schemes have an advantage of being fast in computation, the best-fit model of the unabsorbed spectrum is not necessarily the real one, and—even worse—this *systematic error* is not accounted for.

A better method is required, and actually some attempts have been made. Leighly et al. (2011) used about a dozen quasar NIR spectra as templates to measure the He I*λ10830Å BAL of the quasar FBQS J1151+3822. They deemed the best matched template spectrum as the intrinsic spectrum underlying the He I* BAL and the variation in the best-fits with those different templates as the *systematic uncertainty*. We have developed a pair-matching method to select C IV BALs (Zhang et al. 2014), which is similar to those used in the studies of extinction curves in the literature (e.g. Wang et al. 2012). The postulate of the pair-matching method is the similarity of continua and emission line profiles between BAL and non-BAL quasars except the (possible) dust reddening effect (see, e.g., Weymann et al. 1991; Ganguly et al. 2007). Therefore, we can always find one or more non-BAL quasars whose spectra resemble the spectral features surrounding the BAL of a given BAL quasar, provided the library of the non-BAL quasar spectra is large enough. In order to investigate the He I* λ3889 BALs, which are much weaker than the usually studied BALs in C IV and Mg II, we improve the pair-matching method on two aspects. First, we refine carefully the matching procedure to suit the case of He I*λ3889 absorption; second, we implement its merit of being able to quantify the systematic error.

Combining all together the Mg II BAL quasars detected by T06, G09 and Z10, regardless of

their own selection criteria, we obtain a large sample of 351 distinct Mg II BAL quasars.[1] In the following subsection, we will first apply the pair-matching method to the Mg II BAL quasars, and obtain measurements of the BAL properties uniformly by this method; meanwhile the method will be described in detail. Then, based on our own measurements, we will build the parent Mg II BAL sample which comprises 285 objects (see below).

2.2. Mg II BAL measurements by the pair-matching method

First of all, we apply the pair-matching method to the 351 objects compiled above to measure the Mg II BALs. Our purpose is two-fold: (1) to test our pair-matching method (including the BAL selection procedure and criteria) with Mg II BALs, which is much stronger and easier to measure than He I*λ3889; (2) to measure Mg II BAL parameters uniformly and in the same way as we will do with the He I*λ3889 BAL in § 2.3. The SDSS spectra[2] are corrected for the Galactic extinction using the extinction map of Schlegel et al. (1998) and the reddening curve of Fitzpatrick (1999), and transformed into the rest frame using the redshifts provided by Schneider et al. (2010). Our automated procedure consists of the following steps.

1. **Build up the library of unabsorbed quasar spectra as templates.** The unabsorbed quasar spectra for the template library are all selected from the SDSS DR7 quasar catalog (Schneider et al. 2010). Only quasars at $0.4 \leq z \leq 2.2$ are considered to ensure Mg II lies in the spectral coverage. We use only spectra with median S/N > 25 pixel^{-1} in the 2400-3000 Å region, and exclude any possible BAL quasars in previous BAL catalogs. Finally, a library of 1343 quasar spectra are selected as templates, which are visually examined to have no Mg II absorption features.

2. **Loop over the templates for target BAL quasars.** For each of the target BAL quasars, we fit the continuum and emission lines with each template in a looping way. We picked up acceptable fits with reduced $\chi^2 < 1.5$. To fit the spectrum of a target quasar ($f_{obj}(\lambda)$), the template spectrum ($f_t(\lambda)$) is multiplied by a second-order polynomial, accounting for possible reddening and flux calibration problem, and finally yields a best-matched spectrum $f_{t'}(\lambda)$. This

---

[1]The published Mg II BALs in Z10 are only at $0.4 \leq z \leq 0.8$, so we use the same pipeline of Z10 to enlarge this sample to 175 Mg II BALs at $0.4 \leq z \leq 1.35$ in the SDSS DR5.

[2]This parent sample is compiled from the SDSS DR5, yet here we use the spectral data reduced by the improved SDSS pipeline, version *rerun 26*, as released since the SDSS DR7 (downloadable at http://das.sdss.org/spectro/ss_tar_26/), instead of the data reductions archived in the SDSS DR5 (version *rerun 23*).

can be expressed analytically as follows,

$$f_{\text{obj}}(\lambda) \;=\; f_{t'}(\lambda) \;=\; f_t(\lambda) \cdot (a + b\lambda + c\lambda^2) \;, \tag{1}$$

where a, b and c are free variables in the fitting.

In the case of searching for Mg II BALs, only the spectral region in the range of 2400–3200 Å is used. Bad pixels identified by the SDSS reduction pipeline and absorption troughs are masked out. Initially, the wavelength range of 2613–2809 Å is masked out as a possible absorption-affected region; A refined absorption-masking region, as described below, will be obtained according to the best-fit unabsorbed spectrum, and the fitting is then re-done in iteration. Generally for a object spectrum there are more than 20 acceptable fittings with reduced $\chi^2 \leq 1.5$. However, in some spectra with iron absorption and/or peculiar Fe II emission surrounding Mg II, the number of acceptable fittings is less than 20. For such objects, we carefully mask out those features until we get about 20 acceptable fittings.

Then we make a mean model spectrum ($f_{model}(\lambda)$) of all the acceptable fits ($f_{t'}(\lambda)$), and normalize the object spectrum with it:

$$I(\lambda) = \frac{f_{\text{obj}}(\lambda)}{f_{\text{model}}(\lambda)} \;. \tag{2}$$

In order to determine the region of possible absorption trough, we smooth $I(\lambda)$ to reduce noise and unresolved absorption features. The smoothing is performed with a 5-point wide Savitsky-Golay filter of degree 2. The absorption trough region, as defined by the minimum velocity (v_{min}) and maximum velocity (v_{max}),[3] is determined as pixels with flux densities lower than unity by twice the root-mean-square (rms) fluctuation; i.e., $I(\lambda) < 1 - 2\,\text{rms}$, where the rms is calculated in the 2400–2600 and 2900–3000 Å regions of $I(\lambda)$. The absorption width, W_{abs}, is defined as $|v_{\text{max}} - v_{\text{min}}|$. Likewise, the absorption depth (d_{abs}), defined as the maximum depth in the trough,[4] is calculated.

As described in the above, the thus calculated absorption region serves as part of the masking regions to feed the fitting routine for a better iterated fit. The convergence criterion is set to be that both W_{abs} and d_{abs} change less than 10% between iterations. Normally, two iterations are enough to get convergent results.

---

[3]Zero velocity is defined by using the improved redshifts for SDSS quasars provided by Hewett & Wild (2010), with 2798.75 Å for Mg II and 3889.74 Å for He I* (vacuum wavelength).

[4]Note that here for convenience we define d_{abs} to be the deepest point as measured from the smoothed spectra and use it throughout the paper. We would caution that this d_{abs} is easily affected by smoothing, noisy pixels and spectral resolution. In this work, as the noisy pixels are masked and smoothed out, and the absorption trough is broad enough to be insensitive to the smoothing and the spectral resolution, this d_{abs} is robust; otherwise, the absorption-averaged depth of the trough is a better definition for the depth of trough.

We note that in previous studies on C IV and Mg II BALs the BAL region is usually set to be the continual pixels deeper than 10% of the normalized continuum (e.g. Weymann et al. 1991). However, it is *not proper for weak absorption troughs* based on our following tests (e.g., in the case of He I*λ3889 generally). So we adopt the above criterion that is set by trial and error, and by which the contrast (significance) of the absorption is *with respect to the spectral quality instead of to the continuum strength*. Anyway, the previous treatment (10% of the continuum strength) is just for the ease to handle, yet not physically or statistically meaningful.

3. Identify and measure BALs. For each of the targets, there are $\gtrsim 20$ best-fit models of the unabsorbed spectrum. In practice, we deem all those models equally possible (in terms of their reduced χ^2 being ≤ 1.5).[5]

For each accepted model $f_{t',i}(\lambda)$, the absorber rest-frame EW of the possibly existing BAL can be calculated as follows,

$$EW_i = \int_{\lambda_l}^{\lambda_u} [1 - I_i(\lambda)]d\lambda \; , \tag{3}$$

where λ_u and λ_l are the wavelength corresponding to the v_{max} and v_{min} as described in the above in rest wavelength frame, and $I_i(\lambda) = f_{obj}(\lambda)/f_{t',i}(\lambda)$.

Then the mean of all the EW_i values, $\overline{EW}$, is a good estimate of the true value (EW), and the standard deviation indicates the systematic error of this pair-matching method (σ_{sys}), as discussed in § 2.1 (see also Leighly et al. (2011)). On the other hand, we can estimate the purely statistical error ($\sigma_{n,i}$; i.e., caused by random noises) for every EW_i. We follow the same way of T06 to calculate $\sigma_{n,i}$, accounting for both the error in the fit of the unabsorbed spectrum and the measurement error in every pixel comprising the absorption trough. Then we take the mean of the $\sigma_{n,i}$ values as the final random error (σ_n). The total measurement error of the BAL EW is thus estimated as

$$\sigma_{total} = \sqrt{\sigma_{sys}^2 + \sigma_n^2} \; , \tag{4}$$

Based on the above calculated quantities, we set the criteria of *bona fide* BALs as follows:

(i) EW $\geq 2\,\sigma_{total}$ (the intensity criterion) ,

---

[5]According to our experiment, the fit of the unabsorbed spectrum predicted from the unabsorbed regions with minimum reduced χ^2 is not necessarily the real one underlying the absorption region. This is because there is essentially no ideal, well-defined relationship of quasar spectra between different wavelength regions to a very precise degree; this is even true for the local AGN continuum usually modeled with a power-law. According to our trial and error (cf. Appendix A.2), the best-fit models with reduced $\chi^2 \lesssim 1.5$ are basically indistinguishable.

(ii) $|v_{\max} - v_{\min}| \geq 1600\text{km s}^{-1}$ (the width criterion) .

    The whole fitting and identification procedures are summarized in Figure 1. Six Mg II BALs are chosen as examples to show the fitted continua in Mg II and He I* region in Figure 2. The acceptable fits for each source are shown by green dotted lines, and the composite spectrum built from these fits is shown by red solid line. The standard deviation of the acceptable fits is thus the systematic error of this method. Among the 351 sources in the combined sample, 53 sources are rejected according to our criteria, 285 Mg II BAL quasars are culled as our parent sample, and the left 13 sources cannot be categorized because their intrinsic spectra are unusual and difficult to be fitted well by the template quasars. Those 13 objects, some of which have been studied by Hall et al. (2002), are listed in Table 7 (see Appendix A.3) and not included in our parent Mg II BAL sample.

    Figure 3 is the direct comparison of the measurements of EWs (AIs), $v_{\max}$, W_{abs} and d_{abs} among T06, G09, Z10 and our sample. Basically our parameter measurements are consistent with those of T06, G09 and Z10, especially for the BAL quasars that detected by all the three samples (red dots). Apparent discrepancies are mostly shown in maximum velocities and widths of FeLoBALs (blue dots), for which the boundary of the Mg II absorption lines are easy to be contaminated by Fe II absorption lines. Four FeLoBAL quasars are shown in Figure 2 (J074554.74+18187.0; J080248.18+551328.8; J084044.41+363327.8; J104459.60+365605.1), which are also marked in Figure 3 by green pentagrams.

    Before applying the pair-matching method to the detection of He I*$\lambda3889$, we perform a series of tests to evaluate the pair-matching method (see Appendix A.2) both for Mg II and He I*. The tests show that spectral S/N and absorption depth (d_{abs}) are the primary factors that affect absorption detection. Figure 4 shows the contour plots of the relative error of the absorption EW and recovered detected fraction in the S/N and d_{abs} space. From this figure, with increasing S/N and d_{abs}, the relative error decreases and the detection fraction increases. This figure shows that the relative error decreases and the detection fraction increases with increasing S/N and d_{abs}. An important implication is that we can estimate the accuracy (relative error of the absorption EW) and efficiency (detection fraction of the BAL) of the pair-matching method as long as we know the spectral S/N and d_{abs} of a given absorption line. The detection by the pair-matching method is almost complete for absorption troughs with high S/N (≥35) or large absorption depth ($d_{\mathrm{abs}} \geq 0.5$). For absorption troughs with either a low S/N (~10) or a small depth (~0.15), which is common for He I* $\lambda3889$, the detection rate can be still as high as $\sim60\%$.

2.3. The He I*λ3889 BAL sample

Now we use the pair-matching method to search for He I*λ3889 absorption troughs in the parent sample of 285 Mg II BAL quasars. The procedure to identify He I*λ3889 absorption is essentially the same as described in Section 2.2 for Mg II BALs. As He I*λ3889 absorption is much weaker than Mg II, we make a few minor adjustments suitable to detect weak absorption troughs (e.g., the templates of unabsorbed quasars, the masking regions, and a loosening of the width criterion). The details are as follows.

A template library of 316 unabsorbed quasar spectra at $0.4 \leq z \leq 1.35$ is compiled from the SDSS DR7 quasar catalog, which are selected to have median S/N >25 pixel^{-1} in 3500-4000 Å region and have no any absorption features.[6] Each of the Mg II BAL quasars spectra is fitted with the 316 templates. Only the line-free continuum region in the spectral range of 3500–4000 Å is used. Bad pixels are masked out according to the tags by the SDSS pipeline. We carefully mask the regions contaminated by the [O II]λ3727 and [Ne III]λ3869 emission lines to make sure that the placement of AGN continuum around He I*λ3889 will not be affected by those nearby narrow emission lines. Initially the possible He I* absorption region is masked out according to the measured Mg II absorption region, and later on in the iterated fittings it is masked out according to the calculated v_{min} and v_{max}. Other absorption lines such as Ca II$\lambda\lambda$3949, 3969 and high order Balmer absorption lines, if present, are also masked. Following the procedure as described in Section 2.2 (see also Figure 1), fittings with reduced χ^2 smaller than 1.5 for each candidate are picked up as acceptable, and the v_{min}, v_{max}, d_{abs}, EW, and σ_{total} are calculated for the (possible) He I*λ3889 absorption. Then the intensity criterion is applied to select *bona fide* He I* BALs. The width criterion is not applied to He I*λ3889, because under the typical ionization parameter (U) and hydrogen column density (N_H) conditions the optical depth of He I*λ3889 is much smaller than that of Mg II (cf., Leighly et al. 2011, their Figure 15). Although the observed widths of He I*λ3889 absorption troughs are narrower than the conventional definition of BAL, we still refer to them as He I* BALs in this paper, given most likely that they are physically associated with the BAL outflows as shown in this work.

As a sanity check, we visually inspect the SDSS spectra of the selected He I* BALs. The presence of He I*λ3189 and/or even higher order He I* absorption lines in many objects is a strong support for the genuineness of our measured He I*λ3889 absorption trough. And a few spurious objects are excluded as they are mimicked by absorption features from H9, H10 or H11 Balmer absorption lines. Finally we obtain 101 He I*λ3889 BAL quasars, which are listed in Table 4.

---

[6]Some template spectra have strong [O II]λ3727 and [Ne III]λ3869 emission lines, we apply models of one polynomial plus one or two Gaussian profiles to fit the spectra locally, and subtract these two emission lines from the template spectra.

We further apply the pair-matching method to detect He I*λ3189 absorption line, and 52 objects out of the He I*λ3889 BAL sample pass the intensity criterion. The measurements of the 52 He I*λ3189 BAL subsample are summarized in Table 5.

On the other hand, the optical depth ($\tau \propto \lambda f_{ik} N_{ion}$) of He I*$\lambda$10830 is 23.5 times that of He I*λ3889 (according to Table 2), so absorption trough of He I*λ10830 should be much stronger than that of He I*λ3889. Thus, if we detect BALs in He I*λ10830, the detection probability should be higher. As a check, we have made NIR spectroscopic observations for five sources in this present He I*λ3889 BAL sample. It turns out that all of them show evident He I*λ10830 BALs. The details of the NIR observations and data are presented in A.6.

Based on our measurements of the Mg II and He I*λ3889 absorption troughs using the same technique, we present a direct comparison of the two in Figure 5. The parameters such as the EW, d_{abs}, v_{max} and W_{abs} of He I*λ3889 are smaller than those of Mg II consistently. Moreover, the absorption-weighted average velocity (v_{avg}, namely the velocity centroid) for Mg II and He I*λ3889 agrees fairly well, with a very small scatter. These facts indicate a dynamical connection between the gas producing the two absorption lines.

3. Fraction of He I*λ3889 Absorption in Mg II BAL Quasars

3.1. The measured fraction of He I* λ3889 BALs

There are 101 (35.4%) He I*λ3889 BAL quasars in the parent 285 Mg II BAL quasar sample. Such a high detection rate of He I* BALs in Mg II BAL quasars is unexpected, particularly considering the scarceness of He I* BALs reported so far.

According to the aforementioned tests (see Appendix A.2) using simulated spectra, the detection probability of absorption lines depends mainly on two factors: the spectral S/N and d_{abs} (Figure 22 and Figure 4). Now we carry out a quick investigation of the effect of the spectral S/N to the measured fraction of He I* BALs in the Mg II BAL sample, $f(\text{He I} * |\text{Mg II})$. We divide the Mg II BAL sample into four S/N bins, with roughly equal number of objects in every bins (S/N < 10, $10 <$ S/N < 20, $20 <$ S/N < 30, and $30 <$ S/N < 50), and then calculate the $f(\text{He I} * |\text{Mg II})$ of every bins. Here the S/N refers to the median spectral S/N per pixel around He I* line (3700–4000 Å), and we take the mean S/N of every bins as the fiducial one. The measurement uncertainty of the faction values is estimated using a bootstrap technique. For every an aforementioned bin, we extract randomly a considerable number of objects from it and calculate the He I* BAL fraction in these extracted objects, f_i. This process is repeated for 100 times, and the standard deviation of the f_i values is regarded as the 1-σ error to the He I* BAL fraction of this bin. The observed $f(\text{He I} * |\text{Mg II})$, as a function of spectral S/N, is shown in Figure 6. We find that $f(\text{He I} * |\text{Mg II})$

increases monotonically from 18.1% at S/N $\sim$ 6.5 to 92.9% at S/N $\sim$ 35.5.

As a comparison, the fraction $f(\mathrm{He\,I*}|\mathrm{Mg\,II})$ with respect to the spectral S/N has been predicted in our tests with simulated spectra (see the Appendix A.2 and Figure 7, left panel). The steeply rising trend of the observed one (Figure 6) is well consistent with that of the tests using both assumed Gaussian absorption profiles and actual absorption profiles. It is worth noting that the fraction in low S/N bins predicted by the tests is much higher than the what is observed. This can be understood in the following way. Right panel of Figure 7 shows the detection probability of the pair-matching method for absorption troughs with different d_{abs} under different S/N bins, which is marked by different colors. For absorption troughs with d_{abs} larger than 0.5, the detections are almost complete in all the S/N bins using the pair-matching method. While according to measurements for real sample, the distribution of He I*λ3889 absorption troughs peaks at $\sim$ 0.2, and few of them reach d_{abs} $\sim$ 0.5 (Figure 5). This is also proved by the photoionization models in §4. Under normal ionization condition ($\log U \sim$ -1.5), the d_{abs} of He I*λ3889 trough is much weaker than that of Mg II. We infer that essential number of He I*λ3889 absorption line with large d_{abs} should be smaller than the one with small d_{abs}. Compared with the uniform distribution of d_{abs} in the simulations, it is expected that the predicted fraction is much higher than the real sample in low S/N bins. It is also remarkable that in the bins of S/N $\geq$ 30, the fractions of both real sample and simulation are higher than 90%. As shown in the right panel of Figure 7, the recovered percentage is very high even for $d_{\mathrm{abs}} \sim$ 0.1 in the bin of S/N $\geq$ 25. Therefore the distribution of d_{abs} has little effect on the fraction of He I*λ3889 in high S/N bins. That is to say, in high S/N bins, the measured fraction of He I*λ3889 absorption line is very close to its intrinsic value. Our results imply that He I*λ3889 absorption in fact has a fairly high incidence in Mg II LoBAL quasars.

3.2.   Unveiling the He I*λ3889 absorption in low-S/N spectra

As shown above, the detection of the He I*λ3889 absorption troughs in the SDSS spectra of the Mg II BAL quasars is seriously hindered by the low spectral S/N (e.g., $\lesssim$ 20). In order to test our hypothesis that most, if not all, Mg II BAL quasars have He I* BAL features, in this subsection we examine possible He I*λ3889 absorption troughs that are below our detection threshold in the low-S/N SDSS spectra. For this purpose we take two approaches: one is by combining the multiple observations in the SDSS legacy survey and/or the SDSS-III/BOSS; the second is by stacking spectra of low S/N.

In the parent Mg II BAL sample, 61 sources have repeated spectroscopic observations in the SDSS Legacy programme and/or in the SDSS DR10 (SDSS-III/BOSS; Ahn et al. 2014) which are summarized in Table 10. Some interesting sources with repeated observations are commented in Appendix A.5, including several variable sources (e.g., J14264704.7+401250.8). Combining the

multiple spectra of one source could enhance the spectral S/N. Moreover, the BOSS spectra have longer exposure time than the SDSS ones, and therefore higher S/N generally; their S/N is typically $\sqrt{2}$ times that of the SDSS DR7 spectra. According to the analysis of their SDSS DR7 spectra (see Section 2), 34 of the 61 sources do not have detected He I*λ3889 absorption troughs. Twenty-one of the 34 objects have combined spectra with S/N $>$ 15, which is sufficient to detect He I*λ3889 absorption line according to our simulation. We apply the same procedure of the pair-matched method to the 21 combined spectra. It turns out that 4 more sources pass the He I*λ3889 BAL criteria, which are shown in Figure 8. Among the rest 17 sources that we still do not detect He I* absorption, 5 have strong [Ne III]λ3869 emission line, which hinders the detection of He I*λ3869 absorption; 4 sources have a flat and shallow Mg II absorption trough, so the potential He I*λ3889 would be too shallow to be detected (cf. Figure 5); For the rest 8 sources, we failed to detect He I*λ3889 absorption line even in the combined spectra.

Secondly, we stack respectively the sources with and without detection of He I*λ3889 absorption in every S/N bins. As there are only 2 non-detection sources in the highest S/N bin ($30 <$ S/N < 40), we coalesce that bin and the $20 <$ S/N < 30 one. The two kinds of stacked spectra in every bins are shown in Figure 9. We can see that now the absorption troughs emerges apparently in the stacked spectrum of non-detections in each bin. The d_{abs} of those emerging He I*λ3889 troughs is around 0.05, which is too weak to detect in spectra of moderate S/N level (S/N $\lesssim$ 15; Figure 4). Note that the d_{abs} decreases in the bins with increasing S/N; this is because the higher S/N, the higher completeness of detection in individual sources, and thus the weaker absorption troughs in the non-detections. These results, therefore, strongly support our conclusion that the He I* absorption line has a high incidence in Mg II LoBAL quasars.

3.3. Spectral S/N or luminosity?

We would like to mention in passing that a similar trend that the BAL fraction increases with increasing S/N and luminosity has also been found for C IV and Mg II BAL quasars in the literature (e.g., G09; Z10). Ganguly et al. (2007) also suggested that the most luminous quasars are more likely to show BALs. As to our sample, there is also a dependence of the He I* BAL fraction on luminosity, which is shown in the upper-left panel of Figure 10. The He I* BAL fraction is growing up slowly between $44.5 <$ LogL_λ(3000 Å) < 46 erg s^{-1}, and increases sharply in the highest L_λ(3000 Å) bin. As a check, the upper-right panel of Figure 10 shows the relation between spectral S/N and luminosity. A clear edge appears in the spectral S/N-luminosity plane, which indicates that each spectral S/N corresponds to a minimum luminosity. While for the sources with highest luminosities (LogL_λ(3000 Å) > 46 erg s^{-1}), their spectral S/N are all larger than 25. Because the spectral S/N and luminosities are somewhat degenerate, it is important to know which

is the major factor. In order to test this, we select two subsamples from the parent Mg II BAL sample. The two subsamples are selected in a narrow bin of luminosity/spectral S/N, so as to check the dependence of fraction on the other parameter. The first subsample is selected as sources in luminosity bin of $45.4 < \mathrm{Log}L_\lambda(3000\,\text{Å}) < 46$ erg s^{-1} (see the dotted lines), in which the spread of spectral S/N is equivalent to the parent sample. The sample size is 184, which is large enough to do the statistical analysis. For this subsample, luminosity is taken as the controlled factor, and we can see the He I* BAL fraction has no significant dependence on luminosity. But the He I* BAL fraction still has a strong dependence on spectral S/N, which is similar to that of parent sample (see Figure 6). The second subsample is selected as sources in median spectral S/N bin of $5 <$ median S/N < 11 (see the dashed lines), in which the spread of luminosity covers from 10^{44} to 10^{46} erg s^{-1}. As the lower-right panel of Figure 10 shows, though the He I* BAL fraction is growing slowly with increasing of spectral S/N in this subsample, we can approximatively think spectra S/N has a limited influence on the fraction for this subsample. We do not find any significant dependence of He I* BAL fraction on luminosity in this subsample. This test strongly suggests that the spectral S/N is the major factor in determining the He I* BAL fraction. [7]

In order to further test our hypothesis, we perform direct comparisons of the absorption-line, emission-line and continuum properties between our He I* BAL sample and those without detection of He I* absorption in the parent Mg II BAL sample (hereinafter, dubbed as 'non-He I* sample'). The fittings of optical and UV continuum and emission lines are performed with the routines as described by Dong et al. (2008) and Wang et al. (2009); the results are presented in Appendix A.4. As shown in Figure 11, the Mg II BAL properties (EW and d_abs, v_max, and W_abs) between the two samples display no significant difference, which is confirmed by the Kolmogorov-Smirnov (K-S) test with all the chance probabilities $P_\mathrm{null} > 0.01$ or even close to 1. The chance probabilities are also denoted in each panel of this figure. We also compare the continuum and emission-line properties between the two samples. Again, there are no any differences in the UV and optical continuum luminosities, widths of broad Mg II and Hβ emission lines, optical and UV Fe II strength, [O III]$\lambda 5007$ strength, and continuum slope, which are apparent in Figure 12 and confirmed by the K-S test.

As a reference, we also show the distributions for non-BAL quasars in Figure 12. We se-

---

[7]It is worth noting that the problem of the He I* BAL fraction in Mg II BAL is very different with that of C IV or Mg II BAL fraction in all quasars. There is a very strong physical connection between Mg II and He I* absorption lines, which is strongly indicated by both the observation and the photoionization models (see §4). In other words, the probability f(HeI*|MgII) is so high that finding He I* absorption line in Mg II BAL may be only a problem of detection. The C IV or Mg II BAL fraction in all quasars is a much more complex problem. Whether a quasar is classified a BAL quasar or not depends on many factors, which involves the physical condition for a quasar to have high-speed outflows to produce absorption lines, the chance of the outflow gas in our line of sight and if the absorption lines are strong enough for us to detect.

lect the non-BAL quasar sample from SDSS DR7 to match the Mg II BAL sample in redshift and spectra S/N. Therefore the distribution of luminosities of non-BALs agrees well with that of BAL sample. Besides luminosity, non-BAL quasar have different continuum and emission-line properties with the BAL sample, which is confirmed by the K-S test. The most significant difference is the distributions of $\beta_{[3k,4k]}$, that LoBAL quasars have redder UV continue than non-BAL quasars, which have been proved by many previous studies. Our results are in accordance with theirs.

4. Interpretation of the Observed He I* Absorption

4.1. Theoretical modeling

We generate a series of over-simplified photo-ionization models using CLOUDY (c13.03; c.f. Ferland et al. 1998) to investigate the physical relationships between He I*λ3889 and Mg II absorption lines. We start by considering a gas slab, illuminated by a quasar, with a density of n_e and total column density of N_H. Sources in our sample have various absorption intensities for He I*λ3889 and Mg II and some of them also show Fe II, H Balmer, Ca II and even Na I absorption lines, and these imply the detailed physical condition of outflow gases are very different. According to previous studies on the outflows of known He I* BALs (see Table 1), the n_e spans the range of $10^{3.75} \sim 10^8$ cm^{-3} and the log$U$ is varying from -2.42 $\sim$ -0.5. To fully covered the parameter space of our sample, we calculated a grid of models with logn_e varying from 3 to 9 with step of 1 and log$U$ varying from -2.5 to -0.1. We adopt optically thick models to generate a fully developed ionization front, and the stop column densities are setted as as $N_H = 10^{24}$ cm^{-2}. All these models are assuming solar abundance, which can satisfactorily reproduce the observed N_{ion} in previous studies on individual He I* absorbers (e.g. Arav et al. 2001; Ji et al. 2014). The SED incident on the outflowing gas has important consequences for the ionization and thermal structures within the outflow. The commonly used AGN SED is the one constructed by Mathews & Ferland (1987) (hereafter MF87), which is given as Table AGN in CLOUDY package. Subsequent UV and X-ray observations thenceforth have indicated that the FUV slopes of radio quiet quasars are generally softer than MF87 (see detailed discussion in section 4.2 of Dunn et al. 2010. Here we calculated a grid of models of ionized clouds using a realistic, UV-soft SED, which is a superposition of a blackbody "big bump" and power laws. This UV-soft SED is set to be the default parameter given in the `Hazy` document of CLOUDY as follow: $T = 150,000$ K, $\alpha_{ox} = -1.4$, $\alpha_{uv} = -0.5$, $\alpha_x = -1$, and the UV bump of which peaks at around 1 Ryd, softer than the MF87 one. For comparison, we also calculated CLOUDY models using MF87 SED. In the case of the MF87 SED, HeI 2^3S grows steeper before the ionization front of hydrogen, and Mg$^+$ also grows steeper around ionization front than those in the case of the UV-soft SED. However, the differences between the two sets of models is small when we consider only the properties of He I* absorption, especially in

optically thick clouds as considered in this work. In this paper, we use only the results of CLOUDY modelling with the UV-soft SED. We would like to mention in passing that ionizing SED would be more important in optically thin clouds or for jointly considering other absorption lines (Arav et al. 2001), and this need a series of work on case studies.

Figure 13 shows the overview of the models. The Mg II and He I* show different behaviours nearby the hydrogen ionization front. $N_{\mathrm{Mg\,II}}$ increases sharply around the ionization front of hydrogen, while $N_{\mathrm{He\,I*}}$ grows in the front of the ionization front of hydrogen and stops growing behind of that. This is consistent with the result of Arav et al. (2001, see their Figure 8) and Ji et al. (2014, see their Figure 7). Therefore, as absorption gas grows thicker, the He I* and Mg II absorption lines will appear in order. It is also worth noting that N_{ion} of different models set apart from each other according to ionization parameter (U), while models with the same U but different n_e show no large divergences. This indicates that He I* and Mg II are more sensitive to ionization state, which agrees well with Ji et al. (2014).

Our goal is to compare the measurements for observed sample with the results of calculated models. To realize this, we are going to transform the relationship between $N_{\mathrm{Mg\,II}}$ and $N_{\mathrm{He\,I}}$ of models to the relationship between absorption depths. To simplify the discussion, we assume that the absorption gas fully covers the incident continua, so that the apparent column densities (N_{ion}) can be derived from an apparent optical depth profile $\tau = -\ln(I_r)$ directly, where I_r is the normalized residual intensity of the absorption trough. That is

$$N_{ion} = \frac{m_e c}{\pi e^2 f \lambda} \int \tau(\upsilon) d\upsilon = \frac{3.7679 \times 10^{14}}{f \lambda} \int \tau(\upsilon) d\upsilon \;\; (cm^{-2}) \qquad (5)$$

where λ is the transition's wavelength and f is the oscillator strength, and where the velocity is measured in km s^{-1}. As a reference, we provide a table for first 5 He I* lines, Mg II and C IV doublets, including their wavelengths, oscillator strengths (see Table 2).

According to the measurements for He I* sample, v_{avg} of the He I*$\lambda3889$ and Mg II absorption lines have strong correlation, which indicates the two lines are associated dynamically (Figure 5). In the sample, measured He I* is much narrower than Mg II for most sources. This is because, on one hand, Mg II absorption lines we measured are a blend of Mg II doublets, and on the other hand, the shape of absorption feature of low ionization lines is usually different from that of high ionization lines for BALs. Here we roughly build up the relation of Mg II and He I* absorption profile from the sample. Four composites for Mg II absorption profile were constructed in four width (W_{abs}) ranges: 1600< width < 2500, 2500 < width < 3500, 3500 < width < 4500 and width > 5000. Simultaneously, composites for He I*$\lambda3889$ absorption line are also built up. The followings are the procedure for the simulation. A series of Mg II absorption profiles with different d_{abs} are generated based on these composites. In each bin of (n_{H}, U, $d_{\mathrm{abs,MgII}}$), we calculated $N_{\mathrm{Mg\,II}}$ by integrating the Mg II absorption profile, and $N_{\mathrm{He\,I*}}$ was also obtained according to relationship of

$N_{\rm Mg\,II}$ and $N_{\rm He\,I*}$ predicated by models. Then the corresponding He I*λ3889 absorption profile was generated, and we measured its $d_{\rm abs}$. Figure 14 shows the simulated procedures for a model with parameters of BAL outflow gas: $\log n_{\rm e} = 7.0$, $\log U = -1.5$. Figure 15 shows the relationship between Mg II and He I*λ3889 absorption depths of the simulation. In the left panel, we can see that results of simulation well coincide with the measurements of our sample (gray dots). In the right panel, $d_{\rm abs}$ of He I*λ3889 produced by outflows with different $n_{\rm e}$ only show slight differences. While in the middle panel, $d_{\rm abs}$ of He I*λ3889 absorption line are layered according to ionization parameter (U). These again indicate that the $d_{\rm abs}$ of He I*λ3889 absorption line is sensitive to the ionization parameter but insensitive to $n_{\rm e}$. Outflows with large U will produce He I*λ3889 absorption trough with depths equal to or even larger than that of Mg II.

Figure 16 shows the ionization structure in a cloud slab of C IV, Mg II and He I*predicated by the photoionization models we described before. Here we adopt models with $\log n_{\rm H}({\rm cm}^{-3}) = 7$ as the example. The distance from the illuminated surface of the cloud (r, thickness of the cloud) is represented by Hydrogen column density ($N_{\rm H}$) that is the total column density of Hydrogen integrated from the illuminated surface to r. The column densities of other species are calculated in the same way. We can see that the column density of respective species (thus absorption strength) depends on ionization parameter (U) and the cloud/outflow thickness (namely the cloud's column density, $N_{\rm H}$). When the $N_{\rm H}$ of an outflow is too small to develop a Hydrogen ionization front (the case of optically thin clouds), $N_{\rm MgII}$ decrease with increasing U; when the cloud has a sufficiently large $N_{\rm H}$ (optically thick), both high and low ionization absorption lines would be detected. Based on the simulation for the He I*λ3889 absorption depths, we can investigate the possible $N_{\rm Mg\,II}$ and $N_{\rm He\,I}$ range that can be observed. Using the composites for Mg II and He I*λ3889 we constructed for the simulation, we calculated the ionic column densities corresponding to absorption trough with $d_{\rm abs} \sim 0.05$, which is the minimum $d_{\rm abs}$ we can detect using pair-matching method. Therefore, these ion column densities are the boundary of detection for each absorption line. Red, orange and black shades in this figure represent the detection boundary for He I*λ3889, He I*λ10830 and Mg II respectively. According to the figure, as an outflow is growing thick, He I*λ10830 absorption line will be detected first. In the outflow with low ionization parameter (e.g., $\log U = -2$), Mg II absorption line will be detected before He I*λ3889, while in the outflow with intermediate (e.g., $\log U = -1.2$) and high (e.g., $\log U = -0.5$) ionization parameter, He I*λ3889 absorption line will be detected before Mg II. This sequence explain the why the He I*λ3889 absorption lines so prevalent in Mg II BAL quasars. We may also expect that if we observe Mg II BALs in its near infrared band, the fraction of He I* BALs appear in Mg II LoBALs will be much higher. According to this figure and Figure 15, there should be a kind of BAL with obvious He I*λ3889 or strong He I*λ10830 absorption line but without Mg II absorption lines. In fact we did have found three such cases SDSS J0352-0711, J1413+4400 and J0936+5331, which are shown in Appendix A.6. SDSS J0352-0711 is a BAL quasar rejected by T06, G09 and Z10 due to the weakness of Mg II absorption. However,

as Figure 29 shows, they have significant C IV absorption line and He I*$\lambda\lambda$3889, 10830 absorption lines. In spectra of low-z BALs J1413+4400 and J0936+5331, we can hardly find Mg II absorption lines, but He I*$\lambda\lambda$3889, 10830 are significant, which are associated with C IV absorption trough. In addition, the published He I* BAL SDSS J1512+1119 (Borguet et al. 2012, 2013) is also in this case. The strength of He I*λ2946 absorption line is roughly same as Mg IIλ2796 absorption line (Borguet et al. 2012, Figure 3), so He I*λ3889 or He I*λ10830 absorption lines should be much stronger.

4.2. Case study: deriving physical conditions of the outflow gas using He I*

The He I* absorption lines are important diagnostics of the physical conditions of the AGN outflows. The metastable state He I* has multiple upward transitions in a large wavelength span from UV to NIR band, and these absorption troughs are well separated. Particularly, the very small abundance of the metastable state (with a number abundance of about 6×10^{-7}) makes He I* lines hard to saturate, valuable to probe outflows of high column density. The different oscillator strengths of the He I* lines allow us to determine the real optical depth and covering factor of the He I* absorbers (e.g., Leighly et al. 2011), as well as the ionization state of the outflow gas.

Here we present an individual FeLoBAL quasar FBQS 0840+3633 in our He I* BAL sample to exemplify the power of the He I* absorption lines in probing the physical condition of the outflows. Its UV spectrum, taken by Keck/HIRES, has been studied detailedly by de Kool et al. (2002). According to their measurements, the outflow covers a range of velocities from -700 to -3500 km s^{-1} (negative values denoting blueshift), with two main components centered at -900 and -2800 km s^{-1}, respectively. The physical conditions of the two components are found to be significantly different, the low-velocity gas being of lower density ($n_e < 500$ cm^{-3}) and farther away from the active nucleus (~ 230 pc) than the high-velocity one. $N_{\mathrm{HeI*}}$ is growing fast before the ionization front, therefore both the detection and non-detection of He I* absorption lines can place a strong constrain on column density of the gas. In light of the absence of He I*λ2830 absorption line in Keck/HIRES spectrum, they set an upper limit to the hydrogen column density, $N_{\mathrm{H}} \lesssim 2 \times 10^{21}$ cm^{-2}.

We detect significant He I*λ3889 and He I*λ3189 absorption lines in its SDSS spectrum. Then we obtain a NIR spectrum by the Triple-Spec spectrograph on the P200 telescope on 2014 January 17 to measure the expected broad He I*λ10830 absorption line (see Appendix A.6). We apply the pair-matching method to measure Mg II and He I*$\lambda\lambda$3189, 3889, 10830 absorption lines. To fit He I*λ10830, a NIR spectral library of 76 high-S/N unabsorbed quasars from Glikman et al. (2006), Riffel et al. (2006) and Landt et al. (2008) is built up. Our measurements show that the He I*λ10830 absorption covers from -1300 to -4400 km s^{-1}, roughly corresponding to the high-

velocity gas in de Kool et al. (2002), with which the He I*λ3889 and He I*λ3189 troughs agree well. Figure 17 shows the fitting results for Mg II and He I*$\lambda\lambda$3189, 3889, 10830 absorption troughs. The left panels show the best-fit local continuum (blue) for each line and right panels show the zoomed-in normalized absorption troughs.

We use the He I* absorption lines to explore the partial coverage situation for the outflow gas. The optical depth ($\propto \lambda f_{ik} N_{ion}$) of He I*$\lambda$10830 is over 23 times that of He I*λ3889, therefore He I*λ10830 should be heavily saturated provided the observed depth of He I*λ3889 trough. The non-zero flux in the 10830 trough infers a partial coverage situation for the He I* absorber (see Leighly et al. 2011 for the arguments in detail). Besides, since the contribution of residual flux of 10830 trough to the spectrum is lager than the contribution of broad emission lines, the absorber should only cover a fraction of the accretion disk. Therefore, we should subtract the emission lines and normalize the involved part of spectrum with respect to the AGN continuum only. The observed, normalized spectrum can be expressed as follows,

$$R = (1 - C_f(v)) + C_f(v)e^{-\tau(v)}. \tag{6}$$

Here $C_f(v)$ is the cover fraction, and the τ ratios ($\propto \lambda \, f_{ik} N_{ion}$) of He I*$\lambda\lambda$10830, 3889, 3189 are 23.5:1:0.33. Following the methodology of Leighly et al. (2011), we derive the covering fraction, the optical depth and column density of He I*, and their 1-σ uncertainties, as a function of velocity (see Figure 18). The He I* column density and its uncertainty is calculated by integrating, which is $\log N_{\rm He I*} = 14.9 \pm 0.07$ cm^{-2}. The velocity-averaged covering fraction is $\sim 50\%$. According to relation between the $N_{\rm He I*}$ and ionization parameter obtained by Ji et al. (2014, see their Figure 8), we estimate the ionization parameter $\log U$ is between -1.7 and -1.5. Assuming the $n_{\rm He I 2^3 S}/n_{\rm He II} \sim 6 \times 10^{-6}$(de Kool et al. 2002), we estimate the total hydrogen column density N_H to be $\approx 1.36 \times 10^{21}$ cm^{-2}.

A second approach is taken to probe the physical conditions of the outflow gas, in the cases of the presence of BALs of low-ionization species such as Fe II. Besides the covering fraction, He I* and total hydrogen column densities and ionization parameter derived by the first approach, this second approach can further constrain the electron density of the gas. The strategy, called "synthetic-spectra fitting", is as follows (see Shi et al. 2014 submitted to APJ, for the detail). Assuming that the absorption of lowly-ionized metal ions shares the same profile as He I*, we run a grid of photoionization simulations with Cloudy 13.03 to produce synthetic spectra that cover the full space of the above-mentioned parameters, and match them to the observed spectrum (including the continuum, emission lines, and particularly all the absorption lines of interest); Then from the best-matched synthetic spectrum we derived the physical parameters of the absorbing gas. We apply this approach to FBQS 0840+3633, and derive Hydrogen column density $\log N_H =22$ cm^{-2} and ionization parameter $\log U$=-1.7, that are consistent with those obtained by the first approach, and the electron density $\log n_e$=7.5 cm^{-3}. Figure 19 displays the best-matched synthetic spectra, in

the NUV region (left panel) and NIR region (right panel), respectively.

In our He I*λ3889 BAL sample, more than half sources have He I*λ3189 absorption lines, and a few of them also have higher order He I* lines. We can also obtain He I*λ10830 with followup NIR spectroscopic observations. Thus we can derive important physical parameters of the outflow gas such as the covering factor (C_f), He I* column density ($N_{\mathrm{He\,I*}}$) using He I* absorption lines directly. Since He I* absorption lines are sensitive to ionization state of clouds, ionization parameter (U) can be determined by He I* lines alone provide optically thick and in a moderate range of n_e (Ji et al. 2014), or by joint use of He I* and lowly ionized absorption lines such as Mg II. The electron density (n_e) of the outflow gas can be determined by absorption lines sensitive to n_e, such as absorption lines from excited Fe II state. With the above parameters, we can further locate the outflows from the AGN central engine, which is very important to study the connection between SMBH growth and host-galaxy buildup.

4.3. Searching for low-z BAL AGNs via He I*λ3889

So far low-z BAL AGNs are still very rare due to the difficulty of carrying out UV spectroscopic observations for the absorption lines such as C IV and Mg II. Yet low-z BAL AGNs (particularly the high-luminosity version, quasars) are of great importance. First of all, their proximity enables us to investigate not only the properties of their host galaxies but also the spatially resolved outflows per se on the host galaxy scale and the interplay between the outflows and the host-galaxy ISM. Additionally, a number of important spectral diagnostics can be obtained easily through optical spectroscopic observations, e.g., narrow emission lines to calculate the ISM temperature, and broad emission lines to estimate the SMBH mass.

Here we demonstrate the power of using He I*λ3889 absorption troughs to select low-z BAL AGNs by the pair-matching method. We simply set the redshift cutoff to be $z < 0.3$, and start from all the quasar catalogs of the SDSS-I, II, and III (Schneider et al. 2010; Pâris et al. 2014). The selection procedure follows the method as described in Section 2. Note that it is more difficult to identify He I*λ3889 absorption lines without the reference of Mg II absorption. As the result of our above He I* BAL sample shows, the measured widths of He I*λ3889 absorption troughs are narrower than those of the corresponding Mg II BALs. So we set the width criteria to be $|V_{max} - V_{min}| > 800$ km s^{-1} for low-z He I*λ3889 BALs. Then, we carefully examine the candidate spectra that pass the He I* BAL selection criteria. As for the He I*λ3889 absorption of those low-z objects, the high-order Balmer absorption lines from host-galaxy starlight are the principal contamination. Once we find Balmer absorption lines in a spectrum, we omit the object from the sample. Besides, some other absorption lines located at the same velocities as the candidate He I*λ3889 absorption, such as He I*λ3189, He I*λ2946, and even Na D absorption in some spectra, are useful for our

identification. Finally, 19 low-z He I* BALs are identified, which are summarized in Table 6. Note that we only included the most secure detection of broad He I*λ3889 line. The real number of He I* BAL quasars might be much larger than this. For the typical data quality of SDSS spectra, the detection fraction of He I* BAL is about 35%. This suggests that there might be at least 54 low-z He I* BAL quasars. Thus we can roughly estimate the fraction of He I* BALs. There are 2539 quasars with $z < 0.3$ in Schneider et al. (2010) for SDSS DR7 and Pâris et al. (2014) for BOSS DR10 in total. The conservative fraction of He I*λ3889 BAL quasars is about 2.13%. This value is similar to Mg II LoBAL quasar fraction. [8]

The combination of He I*$\lambda\lambda$3889, 10830 is very useful to determine the physical properties of absorption gas. We carried out NIR spectroscopic observations for 5 low-z He I*λ3889 BAL AGNs, namely J0752+1935, J0936+5331, J1535+564406.5, J1634+2049 and J2220+0109, using the Triple-Spec spectrograph on the Palomar 200-inch Hale telescope. All the 5 objects show evident He I*λ10830 absorption features, which confirms our detection of He I*λ3889. Nearly full coverage is found in four of the five absorbers. The rest one, J0752+1935, is about 50%.

The details of the NIR observation and data are described in Appendix A.6. In addition, J0936+5331 and J1305+1819 have archival FUV and NUV spectra, taken by the COS and STIS spectrographs aboard *Hubble Space Telescope* (HST). J0936+5331 shows C IV BAL, while the Mg II absorption feature is absent in its NUV spectra; it is thus another example of HiBAL quasar discussed in Section 4. J1305+1819 show both C IV and Mg II BALs at the same velocities of our identified He I*λ3889.

5.   Summary and Future Works

The primary findings of this work are as follows.

1. We have carried out the first systematic search for He I* broad absorption line (BAL) quasars, yielding a sample of 101 quasars with He I*λ3889 absorption troughs culled from the SDSS DR5 data set. This increases the number of the quasars with any He I* absorption lines—all discovered serendipitously in the literature and including those found via He I*λ10830 line—by more than an order of magnitude. Besides, 52 objects of this He I*λ3889 BAL sample have even He I*λ3189 absorption detected from their SDSS spectra.

2. We have developed an effective pair-matching method and selection procedure, aiming at to select uniformly weak/shallow BALs. Careful treatments are given to the definition of the

---

[8]The observed C IV BAL fraction in quasars has been calculated as $\sim$ 15% (e.g., Hewett & Foltz 2003; Reichard et al. 2003b; G09), and LoBALs comprise $\sim$ 15% of C IV BAL quasars (e.g., Weymann et al. 1991)

absorption region (namely the maximum and minimum velocities of the absorbing outflows) and to the BAL criteria by invoking several statistical measures, particularly taking advantage of the statistical merit of being able to estimate the *systematic error* of the pair-matching method. This methodology, with minor adaption, can be applied to detect other weak spectral features that are highly blended with their complicated surrounding components.

3. This search for He I*λ3889 BALs is based on a large parent sample of Mg II BAL quasars compiled from the literature, with the information of the Mg IIabsorption used as auxiliary reference to guarantee the genuineness of He I*λ3889. We find that the observed fraction of He I*λ3889 BAL quasars in the parent Mg II sample is 35.4%. When only the spectra with S/N > 30 are considered, the fraction is 93%, which is surprisingly high. According to our simulations, we conclude that the observed overall fraction is mainly affected by spectral S/N, and we suggest that (almost) all LoBAL quasars have associated He I* BAL lines.

4. We demonstrate the power of the He I* absorption line as a probe of the physical parameters of AGN outflows by performing a case study on FeLoBAL FBQS 0840+3633. Through detailed analysing the He I*$\lambda\lambda$3189, 3889, 10830 absorption lines, we estimate the covering factor ($\sim 50\%$), Hydrogen column density ($N_H = 1.36 \times 10^{21}$ cm^{-2}) and ionization parameter (log$U$=-1.7$\sim$-1.5) of the outflow gas. We also run a grid of photoionization models using Cloudy 13.03 to produce synthetic spectra, and match them to the observed spectrum. According to the best-matched synthetic spectrum, we derive the physical parameter log$N_H = 22$ cm^{-2}, log$U$=-1.7, which are consistent with the estimation above. Specially, the electron density is determined as log$n_e = 7.5$ cm^{-3} in this way.

5. As another extended application of the He I* absorption lines, we have conducted a pilot search for low-z BAL AGNs via He I*λ3889 in all the SDSS spectroscopic archives. Those AGNs have to be free of host-galaxy starlight (e.g., the stellar high-order Balmer absorption lines) in their SDSS spectra. Finally we find 19 AGNs at $z < 0.3$ with He I*λ3889 absorption troughs. These low-z BAL AGNs are valuable in studying the outflow launching mechanism, the interplay between the AGN outflow and the host-galaxy ISM, the properties of the host galaxies, and the AGN feedback.

There are several lines of fruitful work for the future. First of all, follow-up NIR observation for the He I*λ10830 absorption lines would be instructive to confirm their BAL nature. Moreover, the joint use of He I*$\lambda\lambda$10830, 3889 absorption lines will enable us to determine the covering factor, column density and the ionization parameter of the outflow. In the optical band, by exploiting the huge volume data set of spectra with sufficient S/N and spectral resolution (e.g., the SDSS), we can further develop elaborate procedures to carefully separate stellar absorption features and identify He I*λ3889 BALs. This would be very useful for identifying BALs in AGNs at low redshifts whose spectra are contaminated by starlight.

REFERENCES

Ahn, C. P., Alexandroff, R., Allende Prieto, C., et al. 2014, ApJS, 211, 17

Anderson, K. S. 1974, ApJ, 189, 195

Aoki, K., Oyabu, S., Dunn, J. P., et al. 2011, PASJ, 63, 457

Arav, N., Brotherton, M. S., Becker, R. H., et al. 2001, ApJ, 546, 140

Arav, N., Kaastra, J., Kriss, G. A., et al. 2005, ApJ, 620, 665

Arav, N., Moe, M., Costantini, E., et al. 2008, ApJ, 681, 954

Bautista, M. A., Dunn, J. P., Arav, N., et al. 2010, ApJ, 713, 25

Becker, R. H., Gregg, M. D., Hook, I. M., et al. 1997, ApJ, 479, L93

Boroson, T. A., & Green, R. F. 1992, ApJS, 80, 109

Brotherton, M. S., Tran, H. D., van Breugel, W., Dey, A., & Antonucci, R. 1997, ApJ, 487, L113

Borguet, B. C. J., Edmonds, D., Arav, N., Benn, C., & Chamberlain, C. 2012, ApJ, 758, 69

Borguet, B. C. J., Arav, N., Edmonds, D., Chamberlain, C., & Benn, C. 2013, ApJ, 762, 49

Brinkmann, W., Wang, T., Matsuoka, M., & Yuan, W. 1999, A&A, 345, 43

Brotherton, M. S., Arav, N., Becker, R. H., et al. 2001, ApJ, 546, 134

Cushing, M. C., Vacca, W. D., & Rayner, J. T. 2004, PASP, 116, 362

de Kool, M., Becker, R. H., Arav, N., Gregg, M. D., & White, R. L. 2002, ApJ, 570, 514

Di Matteo, T., Springel, V., & Hernquist, L. 2005, Nature, 433, 604

Dong, X., Wang, T., Wang, J., et al. 2008, MNRAS, 383, 581

Dong, X.-B., Ho, L. C., Wang, J.-G., et al. 2010, ApJ, 721, L143

Dong, X.-B., Wang, J.-G., Ho, L. C., et al. 2011, ApJ, 736, 86

Dunn, J. P., Bautista, M., Arav, N., et al. 2010, ApJ, 709, 611

Elvis, M. 2000, ApJ, 545, 63

Elvis, M. 2006, Mem. Soc. Astron. Italiana, 77, 573

Ferland, G. J., Korista, K. T., Verner, D. A., et al. 1998, PASP, 110, 761

Farrah, D., Lacy, M., Priddey, R., Borys, C., & Afonso, J. 2007, ApJ, 662, L59

Farrah, D., Connolly, B., Connolly, N., et al. 2009, ApJ, 700, 395

Farrah, D., Urrutia, T., Lacy, M., et al. 2012, ApJ, 745, 178

Fitzpatrick, E. L. 1999, PASP, 111, 63

Gallagher, S. C., Hines, D. C., Blaylock, M., et al. 2007, ApJ, 665, 157

Ganguly, R., Brotherton, M. S., Cales, S., et al. 2007, ApJ, 665, 990

Gibson, R. R., Jiang, L., Brandt, W. N., et al. 2009, ApJ, 692, 758

Glikman, E., Helfand, D. J., & White, R. L. 2006, ApJ, 640, 579

Glikman, E., Urrutia, T., Lacy, M., et al. 2012, ApJ, 757, 51

Gregg, M. D., Lacy, M., White, R. L., et al. 2002, ApJ, 564, 133

Hall, P. B., Anderson, S. F., Strauss, M. A., et al. 2002, ApJS, 141, 267

Hall, P. B., Hutsemékers, D., Anderson, S. F., et al. 2003, ApJ, 593, 189

Hamann, F. 1997, ApJS, 109, 279

Hamann, F., Chartas, G., McGraw, S., et al. 2013, MNRAS, 435, 133

Hewett, P. C., & Foltz, C. B. 2003, AJ, 125, 1784

Hewett, P. C., & Wild, V. 2010, MNRAS, 405, 2302

Ji, T., Wang, T.-G., Zhou, H.-Y., & Wang, H.-Y. 2012, Research in Astronomy and Astrophysics,
      12, 369

Ji, T., Zhou, H., Jiang, P., et al. 2014, arXiv:1412.2881

Jiang, P., Zhou, H., Ji, T., et al. 2013, AJ, 145, 157

Joshi, R., Chand, H., Gupta, A. C., & Wiita, P. J. 2011, MNRAS, 412, 2717

Korista, K. T., Weymann, R. J., Morris, S. L., et al. 1992, ApJ, 401, 529

Korista, K. T., Voit, G. M., Morris, S. L., & Weymann, R. J. 1993, ApJS, 88, 357

Korista, K. T., Bautista, M. A., Arav, N., et al. 2008, ApJ, 688, 108

Landt, H., Bentz, M. C., Ward, M. J., et al. 2008, ApJS, 174, 282

Leighly, K. M., ietrich, M., & Barber, S. 2011, ApJ, 728, 94

Leighly, K. M., Terndrup, D. M., Baron, E., et al. 2014, ApJ, 788, 123

Lewis, G. F., Chapman, S. C., & Kuncic, Z. 2003, ApJ, 596, L35

Lucy, A. B., Leighly, K. M., Terndrup, D. M., Dietrich, M., & Gallagher, S. C. 2014, ApJ, 783, 58

Lusso, E., Decarli, R., Dotti, M., et al. 2014, MNRAS, 441, 316

Malkan, M. A., Green, R. F., & Hutchings, J. B. 1987, ApJ, 322, 729

Mathews, W. G., & Ferland, G. J. 1987, ApJ, 323, 456

Meusinger, H., Hinze, A., & de Hoon, A. 2011, A&A, 525, A37

Meusinger, H., Schalldach, P., Scholz, R.-D., et al. 2012, A&A, 541, A77

Murray, N., Chiang, J., Grossman, S. A., & Voit, G. M. 1995, ApJ, 451, 498

Pâris, I., Petitjean, P., Aubourg, É., et al. 2014, A&A, 563, AA54

Reichard, T. A., Richards, G. T., Schneider, D. P., et al. 2003, AJ, 125, 1711

Reichard, T. A., Richards, G. T., Hall, P. B., et al. 2003, AJ, 126, 2594

Richards, G. T., Fan, X., Schneider, D. P., et al. 2001, AJ, 121, 2308

Riffel, R., Rodríguez-Ardila, A., & Pastoriza, M. G. 2006, A&A, 457, 61

Rudy, R. J., Stocke, J. T., & Foltz, C. B. 1985, ApJ, 288, 531

Sanders, D. B., Soifer, B. T., Elias, J. H., et al. 1988, ApJ, 325, 74

Savage, B. D., & Sembach, K. R. 1991, ApJ, 379, 245

Schlegel, D. J., Finkbeiner, D. P., & Davis, M. 1998, ApJ, 500, 525

Schneider, D. P., Hall, P. B., Richards, G. T., et al. 2005, AJ, 130, 367

Schneider, D. P., Richards, G. T., Hall, P. B., et al. 2010, AJ, 139, 2360

Shen, Y., & Ménard, B. 2012, ApJ, 748, 131

Shi, Zhou, H.-Y., Wang, H.-Y., Jiang, P., Ji, T., Liu, W.-J. 2014, submitted to APJ

Storchi-Bergmann, T., McGregor, P. J., Riffel, R. A., et al. 2009, MNRAS, 394, 1148

Tolea, A., Krolik, J. H., & Tsvetanov, Z. 2002, ApJ, 578, L31

Trump, J. R., Hall, P. B., Reichard, T. A., et al. 2006, ApJS, 165, 1

Tsuzuki, Y., Kawara, K., Yoshii, Y., et al. 2006, ApJ, 650, 57

Tytler, D., & Davis, C. 1995, ApJ, 438, 420

Vacca, W. D., Cushing, M. C., & Rayner, J. T. 2003, PASP, 115, 389

Vanden Berk, D. E., Richards, G. T., Bauer, A., et al. 2001, AJ, 122, 549

Véron-Cetty, M.-P., Joly, M., & Véron, P. 2004, A&A, 417, 515

Wang, J.-G., Dong, X.-B., Wang, T.-G., et al. 2009, ApJ, 707, 1334

Wang, J.-G., Zhou, H.-Y., Ge, J., et al. 2012, ApJ, 760, 42

Wang, T. G., Wang, J. X., Brinkmann, W., & Matsuoka, M. 1999, ApJ, 519, L35

Weedman, D., Sargsyan, L., Lebouteiller, V., Houck, J., & Barry, D. 2012, ApJ, 761, 184

Weymann, R. J., Morris, S. L., Foltz, C. B., & Hewett, P. C. 1991, ApJ, 373, 23

Williams, R. J. R., Baker, A. C., & Perry, J. J. 1999, MNRAS, 310, 913

Zhang, S., Wang, T.-G., Wang, H., et al. 2010, ApJ, 714, 367

Zhang, S., Wang, H., Wang, T., et al. 2014, ApJ, 786, 42

Every Mg II BALs
from T06, G09 and Z10

Quasars in DR7 with:
1. $0.4 < z < 2.2$
2. median S/N > 30 in 2400-3000 A
3. no absorption features

Mask Region
(Initially: $2613 \sim 2819$ Å)

Template quasar $\times (ax^2 + bx + c)$

1343 fittings

1343 non-BAL quasars as
the templates

Acceptable fitting : $\chi^2 \leq 1.5$
Num. of good fittings: $n \geq 20$

Composite normalized
spectra;
Calculating absorption
region, width & depth

example

Iteration

Convergent?

N

Y

Calculating: EW_i and $\sigma_{noise,i} (i=0,...,n)$

EW of the target:
$$EW = \overline{EW_i} \ (i = 0,..,n)$$
$$\sigma_{total} = \sqrt{\sigma_{sys}^2 + \sigma_{noise}^2}$$
$$\sigma_{noise} = \overline{\sigma_{noise,i}} \ ; \ \sigma_{sys} = \text{SD. of } EW_i$$

example

abs. region > 1600 km s^{-2}
$EW \geq 2\sigma_{total}$

yes

Mg II BAL

Normalized Flux

d_{abs}
2rms
v_{max} W_{abs} v_{min}

d_{abs}
2rms
v_{max} W_{abs} v_{min}

Rest Wavelength

Mean
distr. of EW
σ σ
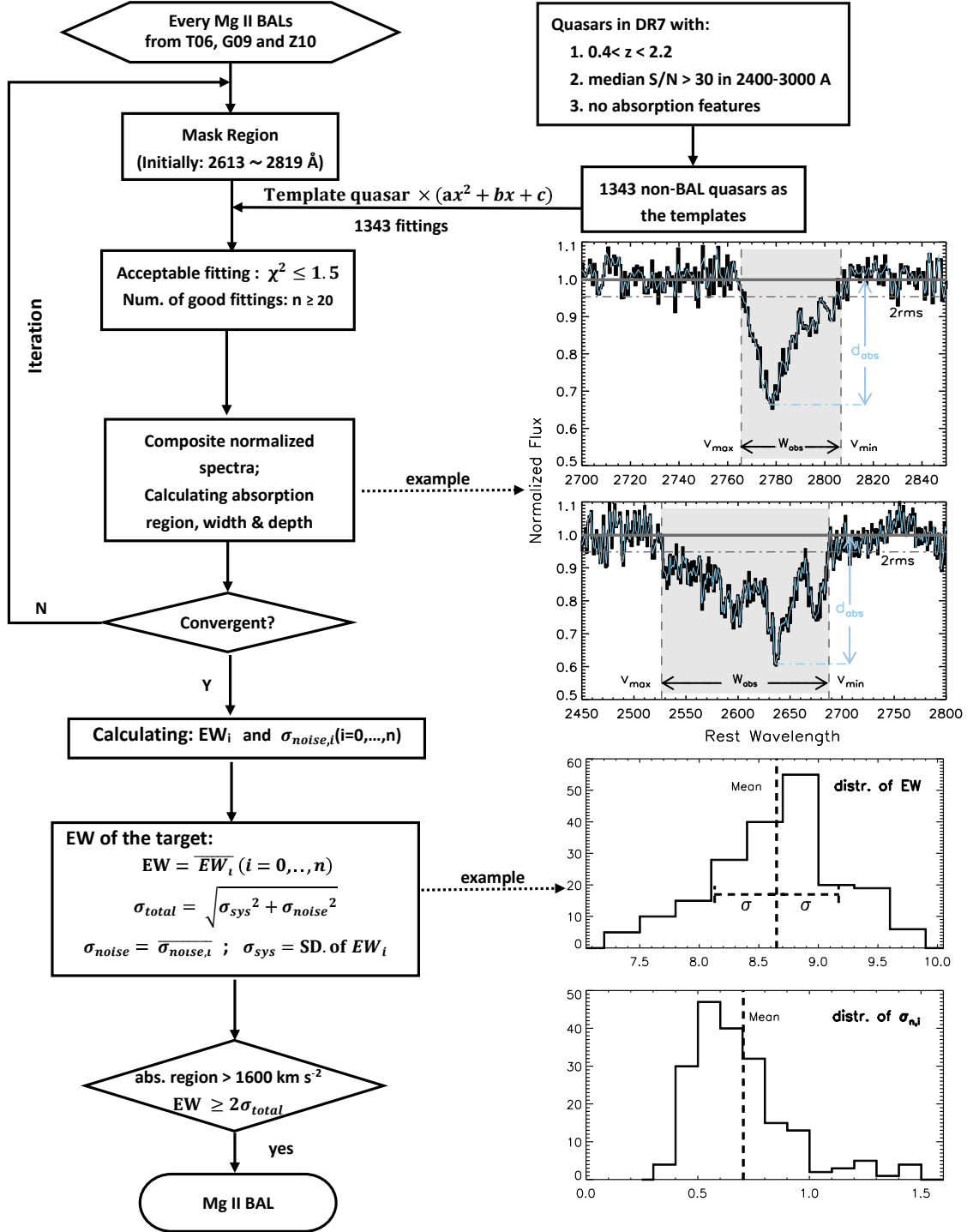
Mean
distr. of $\sigma_{n,i}$

Fig. 1.— Flowchart of the procedure to select broad absorption lines using the pair-matching method (see §2.2 for details). The Blue solid line is the absorption line smoothed with a 5-point wide Savitsky-Golay filter of degree 2, and absorption depth (d_{abs}) are determined as the maximum depth of this.
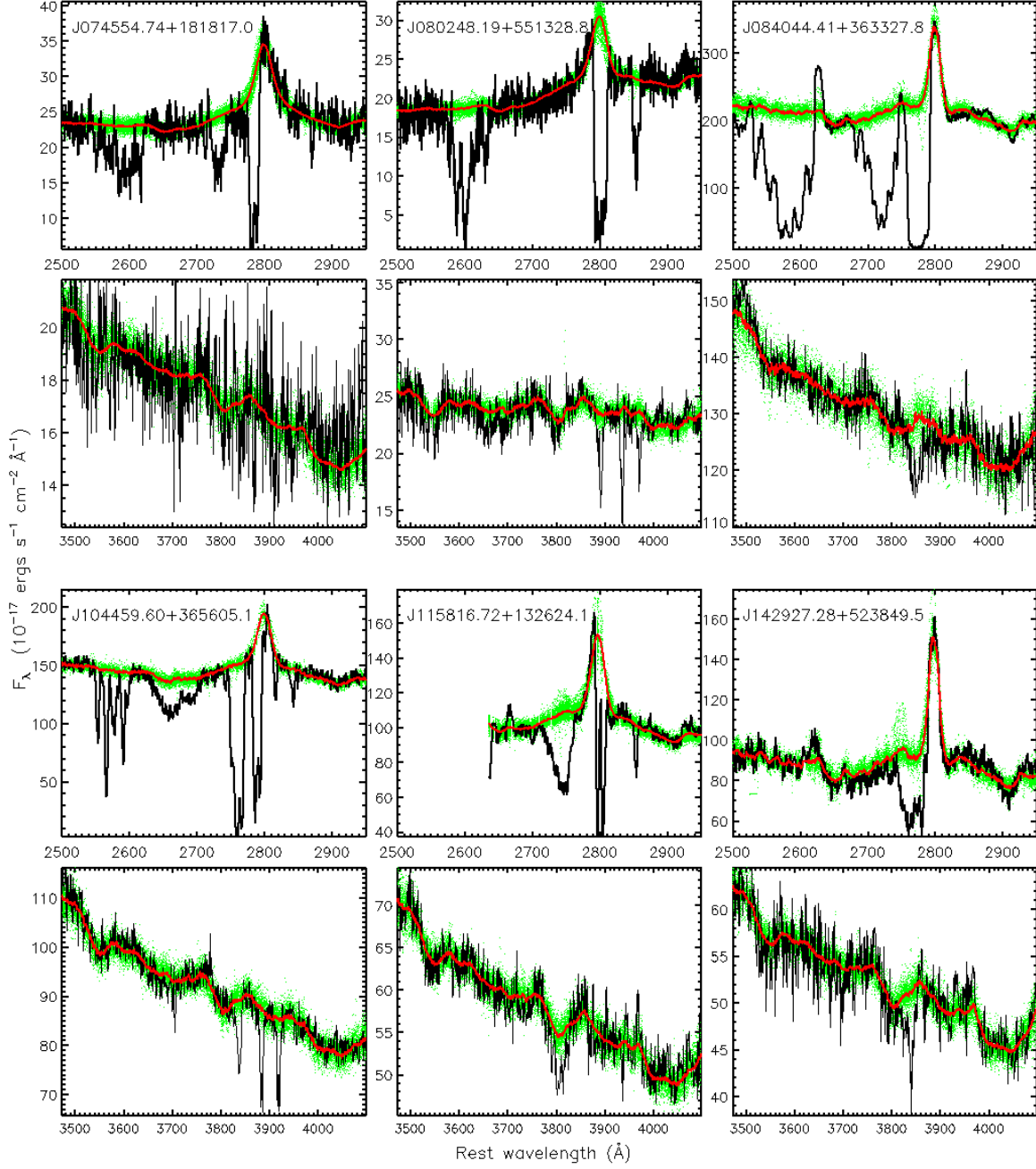
Fig. 2.— Example SDSS spectra of six He Iλ3889 BAL quasars. For every objects, the fittings in the Mg II region (upper panel) and in the He I*λ3889 region (bottom panel) are shown. The acceptable fits of the unabsorbed spectrum in every panels are denoted as green dotted lines, the mean of these acceptable fits are denoted as the red solid line. Note that J0745+1818, J0802+5513, J0840+3633 and J1044+3656 are FeLoBAL quasars.
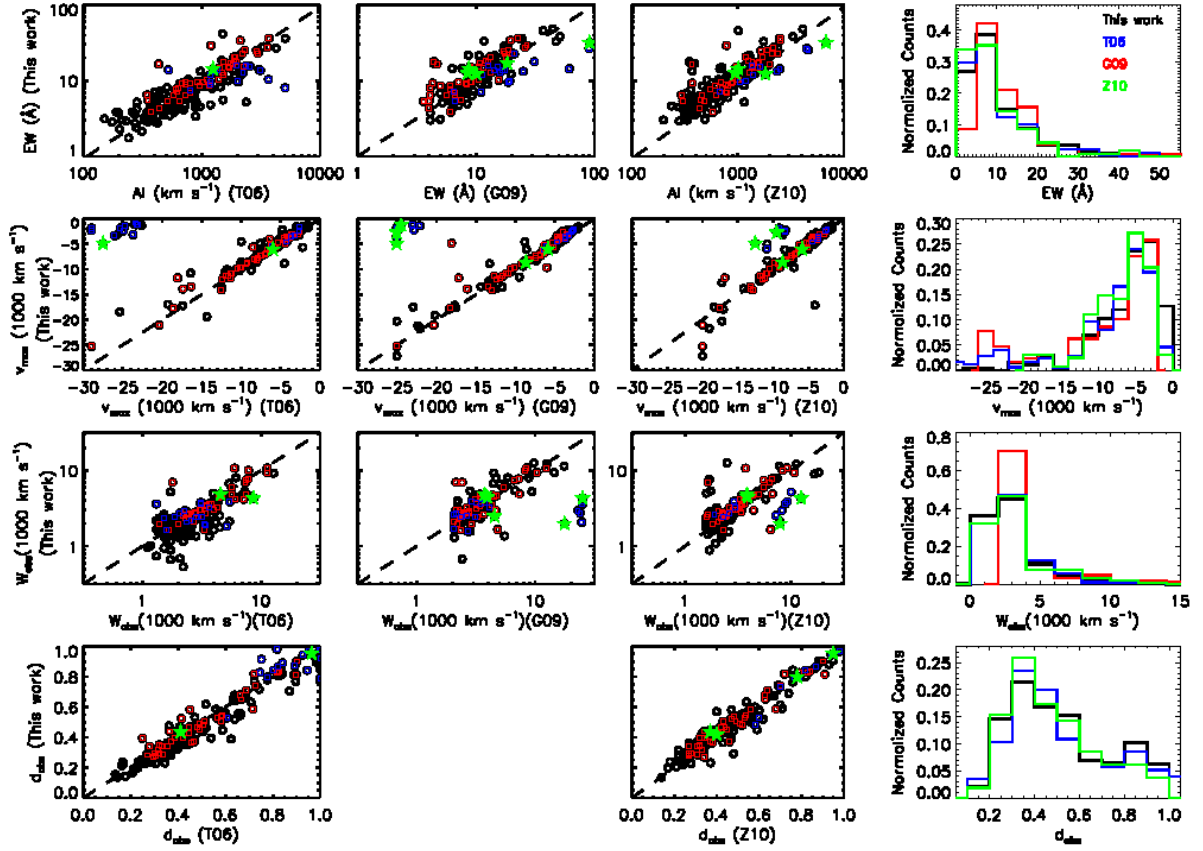
Fig. 3.— *Left*: Comparison of Mg II BAL parameters between our measurements and those by T06, G09, and Z10. Red dots are sources common in the three samples; green pentagrams are the six sources shown in Figure 2; blue circles are FeLoBAL quasars of which the Mg II absorption region is difficult to determine and thus the measurements are the most divergent in the plots. *Right*: Histograms of the BAL parameters measured by these different groups.
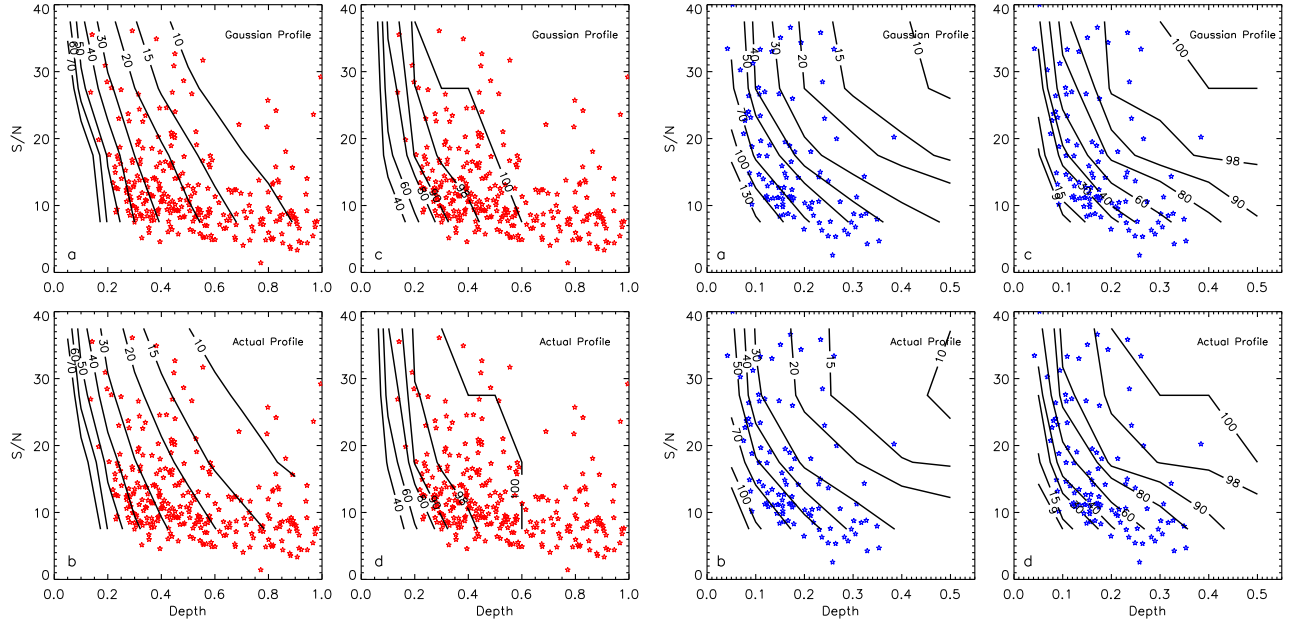
Fig. 4.— Contours of the relative total error (panels a and b) and recovered detected fraction (panels c and d) in the spectral S/N and absorption depth plane based on our simulations (see Appendix A.2), for Mg II (left) and He I* $\lambda 3889$ (right) BALs. The results based on simulated BAL spectra with Gaussian profiles are shown in top panels; those with actual BAL profiles, in bottom panels. Also denoted are the observed parent sample of Mg II BAL quasars (red stars) and the He I* $\lambda 3889$ BAL quasars (blue stars).
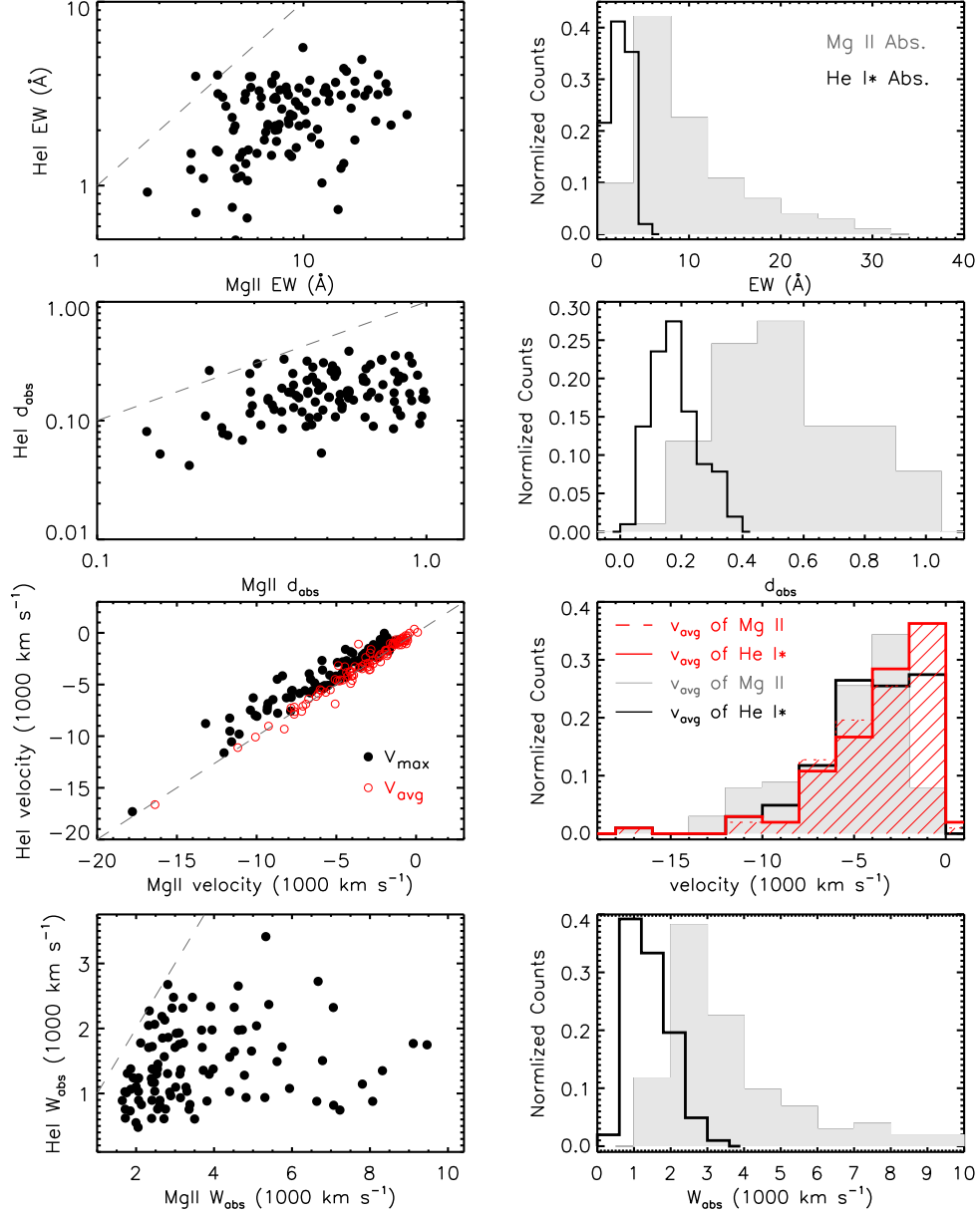
Fig. 5.— *Left*: Comparison of BAL parameters such as EW, depth (d_{abs}), maximum and average velocities (v_{max} and v_{avg}), and width (W_{abs}, namely $|v_{max} - v_{min}|$) between Mg II and He I* λ3889 in the He I* BAL sample. *Right*: The normalized histograms of these parameters.
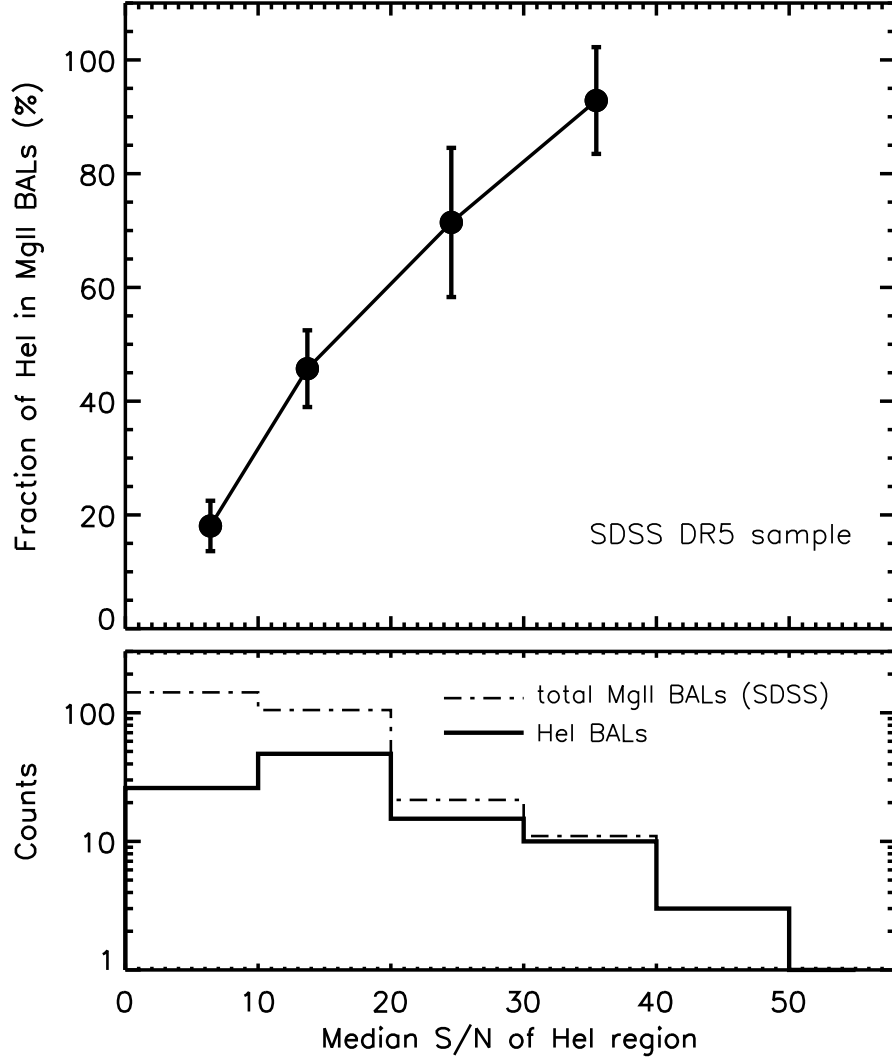
Fig. 6.— *Top*: The detected fraction of He I* λ3889 BALs in the parent Mg II BAL sample, as function of the spectral S/N. Also plotted are the $\pm 1 - \sigma$ error. *Bottom*: Histograms of the spectral S/N of the He I* BAL sample (solid line) and the parent Mg II sample (dashed line).
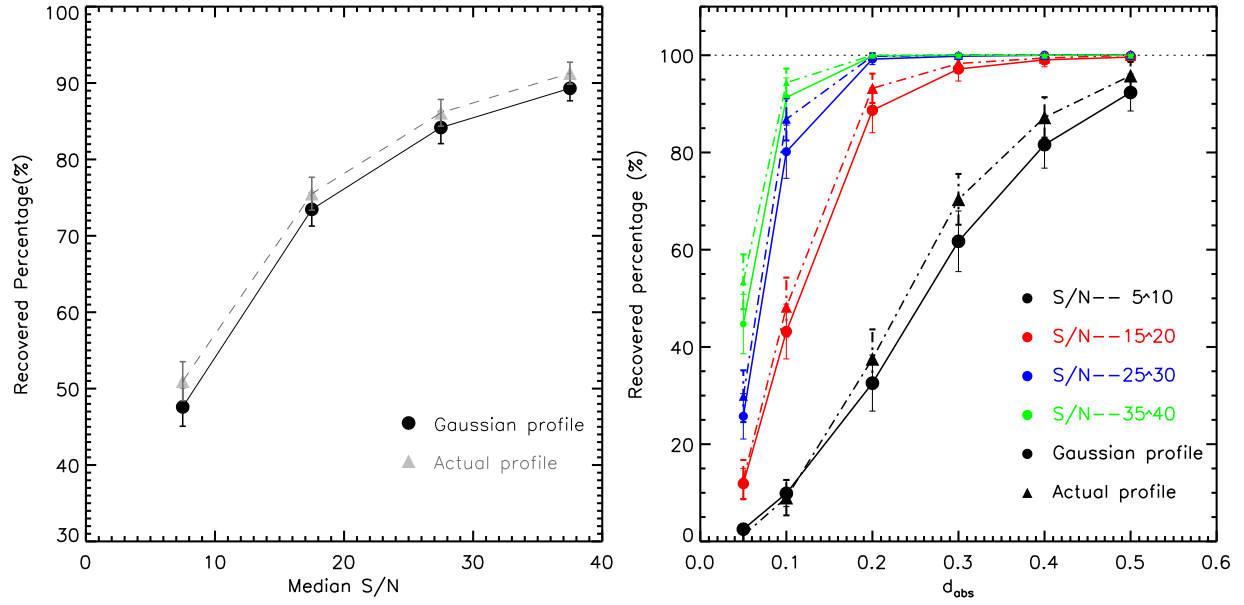
Fig. 7.— *Left*: The recovered fraction of He I* BALs as a function of S/N based on the simulated spectra (see Figure 4 and Appendix A.2). *Right*: The recovered fraction of He I* BALs as a function of absorption depth, based on simulated spectra of different spectra S/N (see Appendix A.2 for details).
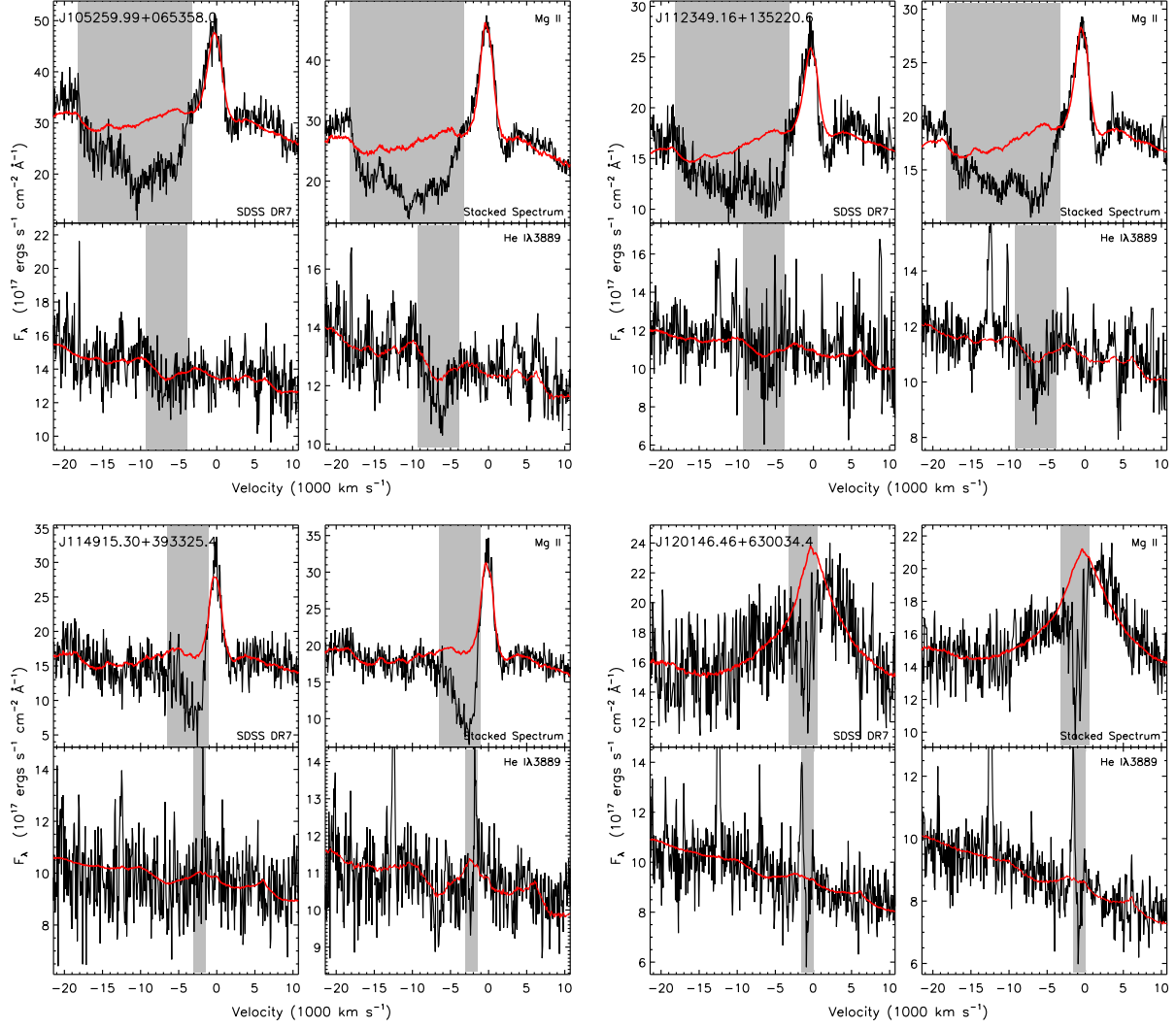
Fig. 8.— Demonstration of the four sources in the parent Mg II BAL sample, whose He I* λ3889 absorption lines are not able to be detected in their SDSS DR7 spectra, but are detected from the higher-S/N spectra by combining multiple observations in the SDSS and BOSS data set. Also shown are the modeled intrinsic spectra by the pair-matching method.

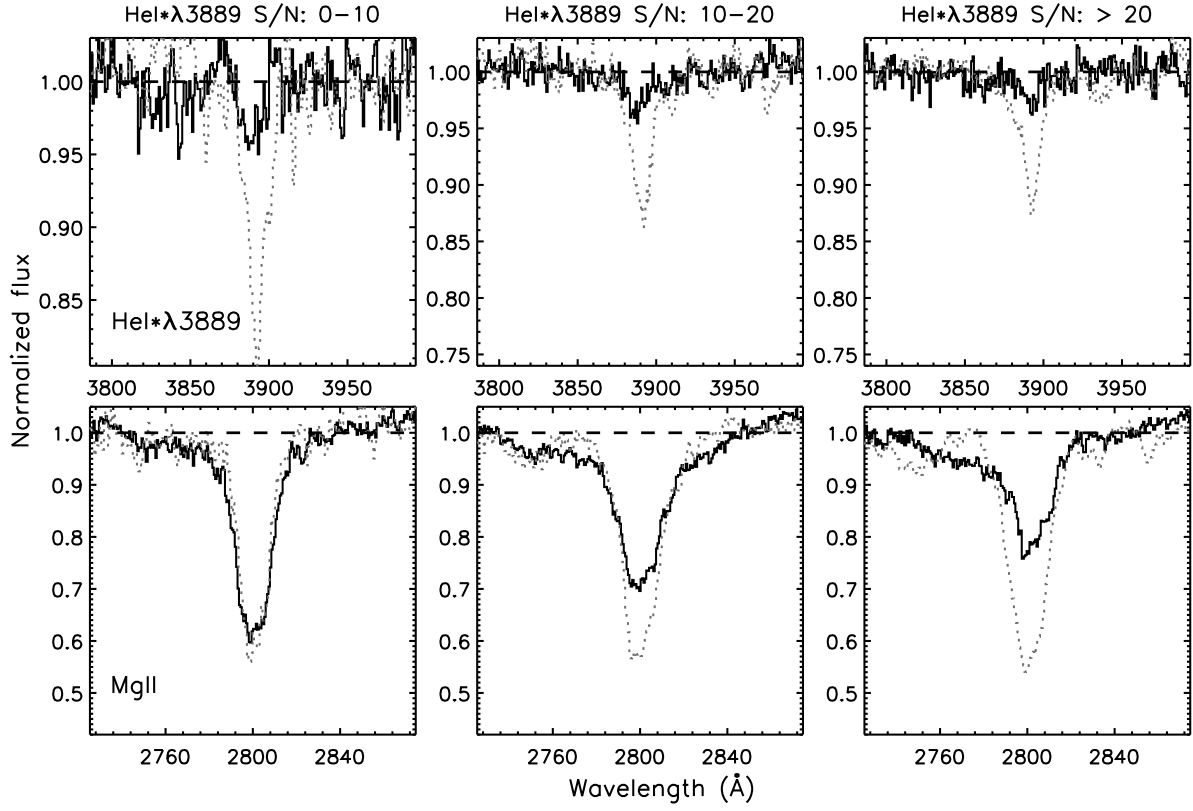Fig. 9.— *Top*: Stacked spectra of three bins of spectral S/N in the He I* $\lambda3889$ region for the sources in the parent sample yet without detected He I* $\lambda3889$ absorption (black solid lines) and those with (gray dotted lines), *Bottom*: The stacked spectra in the Mg II region correspondingly.
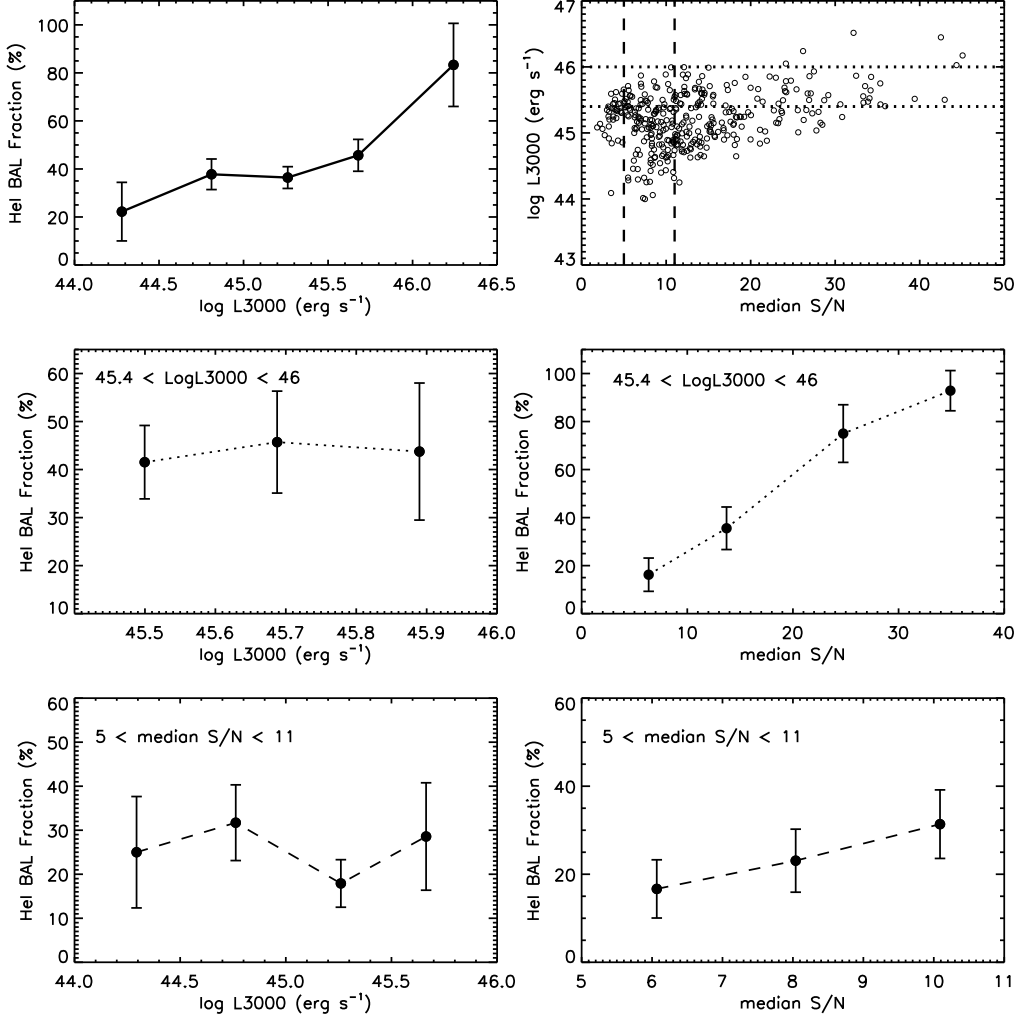
Fig. 10.— *Top-left panel*: Dependence of the He I* λ3889 BAL fraction on the AGN luminosity in the parent Mg II BAL sample. *Top-right panel*: Distribution in the plane of luminosity and spectral S/N. *Middle panels*: Dependence of the He I* λ3889 BAL fraction on the AGN luminosity (left) and on the spectral S/N (right), for the sources in the narrow luminosity bin as denoted by the dotted lines in the top-right panel. *Bottom panels*: For the sources in the narrow S/N bin as denoted by the dashed lines in the top-right panel.
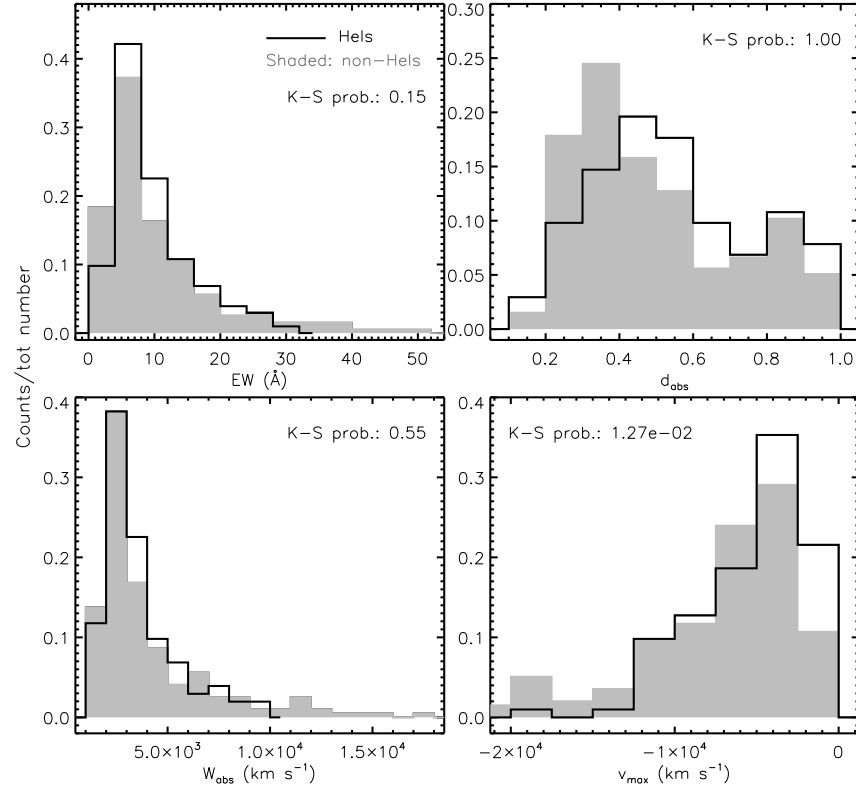
Fig. 11.— Comparison of the normalized distribution of the Mg II BAL parameters between the sources with He I* λ3889 absorption and those without in the parent sample. Also denoted are the chance probabilities by K-S test, which indicate that the two have the same distribution.
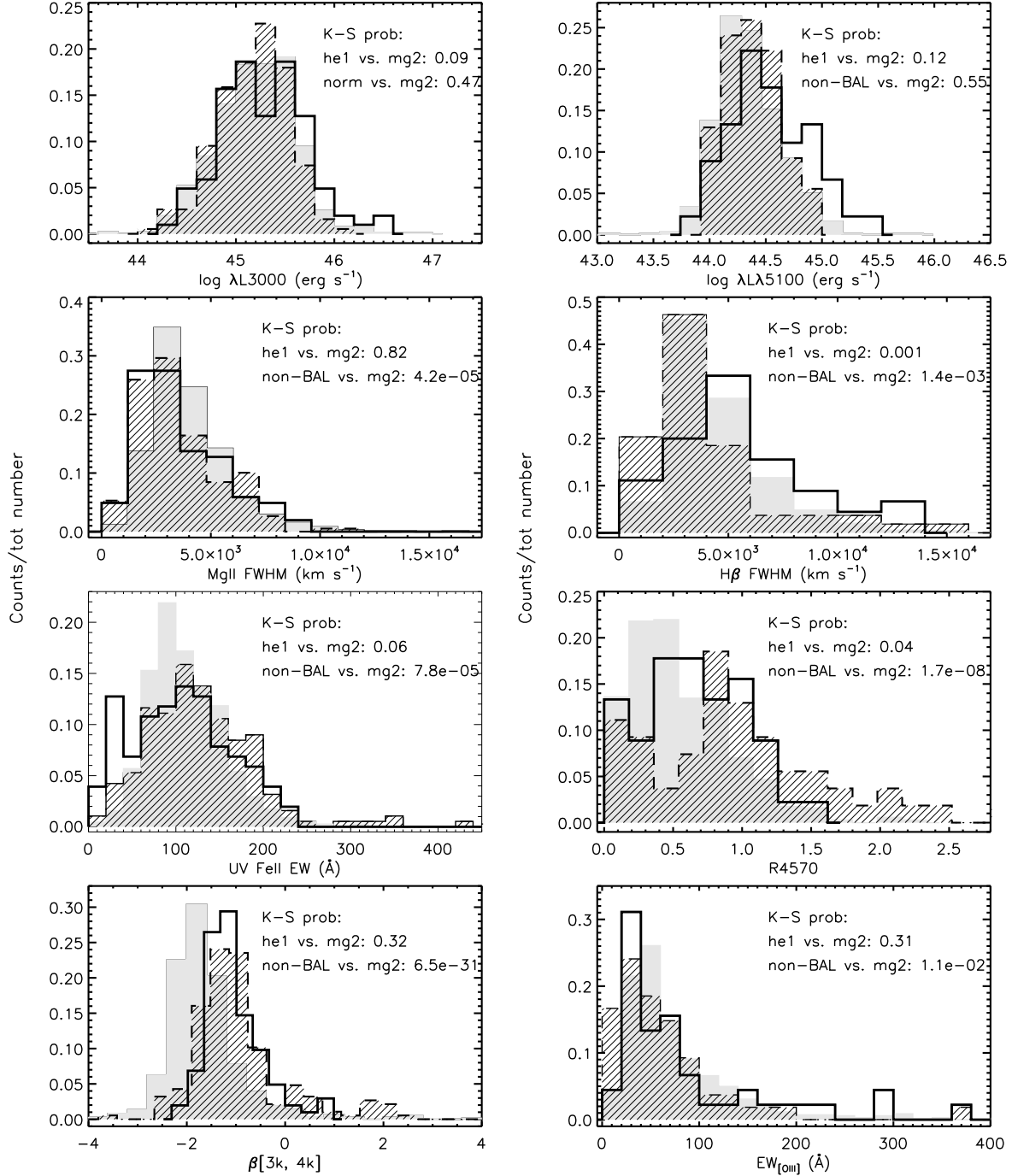
Fig. 12.— comparison of normalized distributions of continuum and emission-line properties between the He I* λ3889 BAL sample (solid line), the parent Mg II BAL sample (filled with tilted lines), and non-BAL quasars (gray shaded). Also denoted are the chance probabilities by K-S test between the He I* BAL sample and the parent Mg II BAL sample, and those between the Mg II BAL sample and non-BAL quasars.
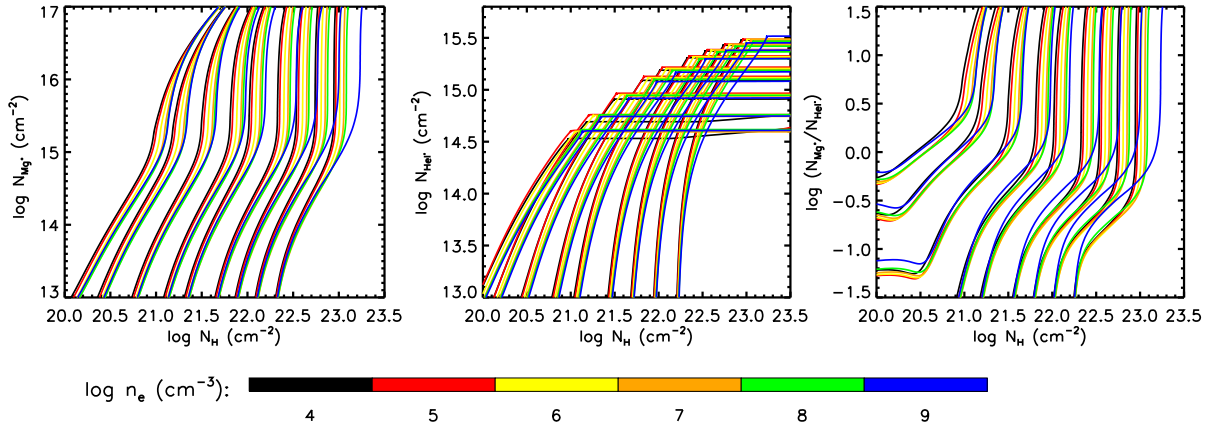
Fig. 13.— Ionization structure of Mg$^+$ (left) and He I* (middle), and the ratio of the number of the two species (right) for a cloud slab calculated by CLOUDY. Here the distance from the illuminated surface of the cloud (r, x-axis) is represented by N_H that is the total column density integrated from the illuminated surface to r. The column densities of Mg II and He I* (y-axis) are calculated in the same way. Models with different hydrogen number densities (n_H) are marked by different colors. Bundles from left to right in each panel denote models with different ionization parameters: log U = -2.0, -1.8, -1.5, -1.2, -1.0, -0.7, -0.5, -0.3. Note that the ionization structure of both species are almost insensitive to n_H, yet fairly sensitive to U.
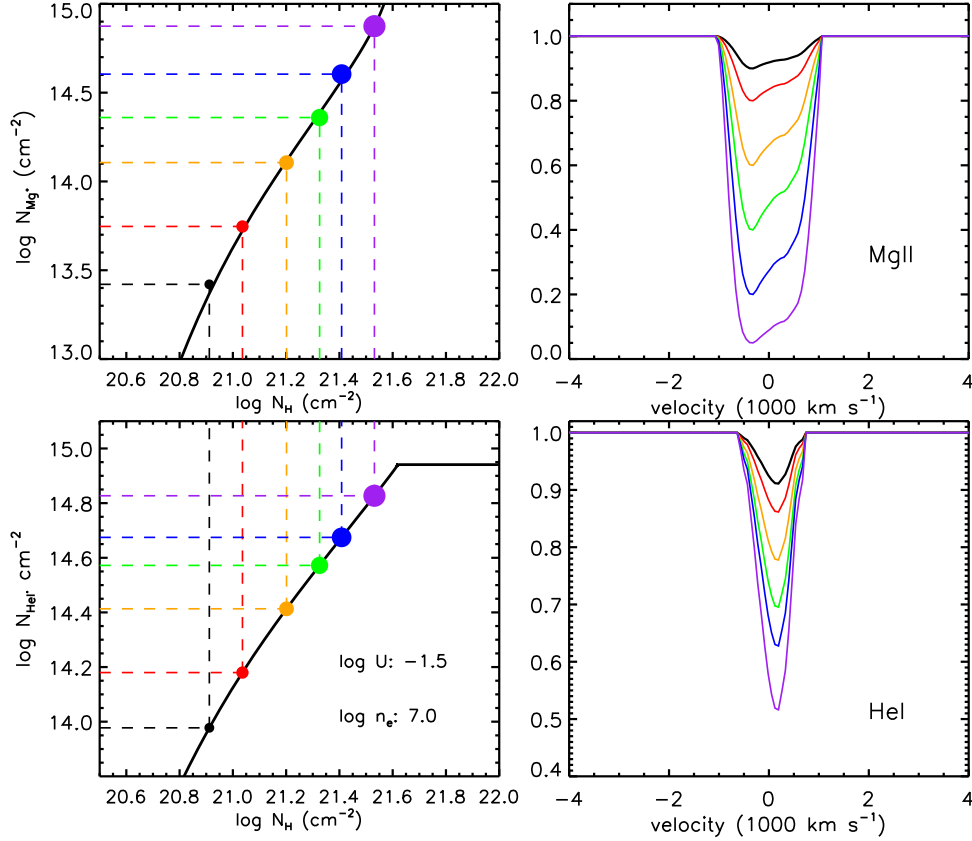
Fig. 14.— Illustrating the procedure that generates the corresponding He I* $\lambda3889$ absorption lines (bottom right panel) from Mg II BALs with given absorption depths (top right panel). This example is for an absorbing cloud with typical physical parameters: $\log n_e = 7.0$ and $\log U = -1.5$. The velocity width of MgII absorption line constructed from the sample is ~ 2000 km s^{-1}, and the corresponding He I* absorption line is ~ 1000 km s^{-1}. From the observed Mg II BAL, the Mg$^+$ column density and then the total column density can be derived according to the CLOUDY calculation (top left panel; cf. Figure 13), then the He I* column density (bottom left panel). Based on these cloud parameters, the He I* BAL can finally be generated.
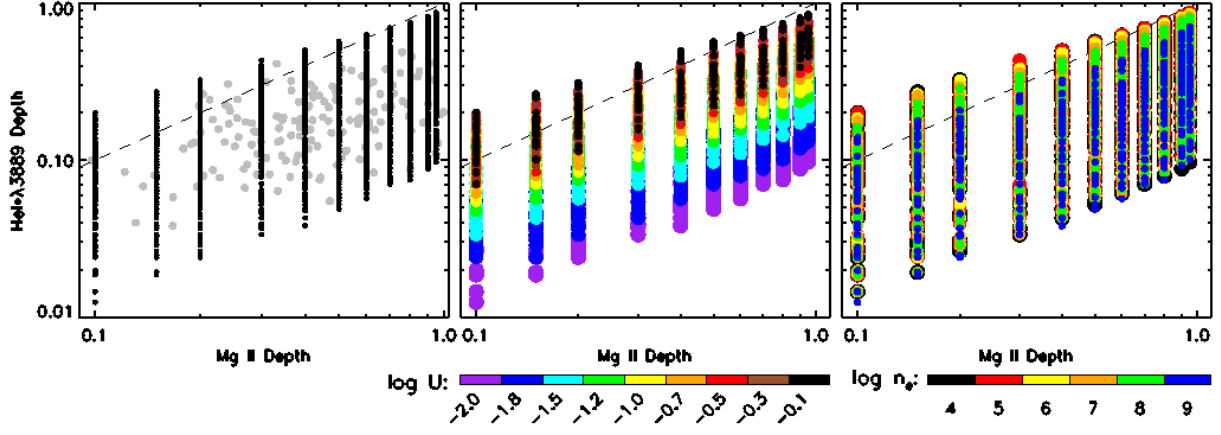
Fig. 15.— The CLOUDY calculations reveal the relationship of absorption depth between Mg II and He I*λ3889 BALs. In left panel, black dots show the relation between Mg II and He I*λ3889 predicted by the calculations. Gray dots are the measurements of the He I* BAL sample as shown in Figure 5. The next two panels are the same with the left panel, but with different colors denoting ionization parameters (log$U$) and electron density (n_e), respectively. Note the strong dependence of He I*λ3889 absorption depth on ionization parameter, yet little on electron density.
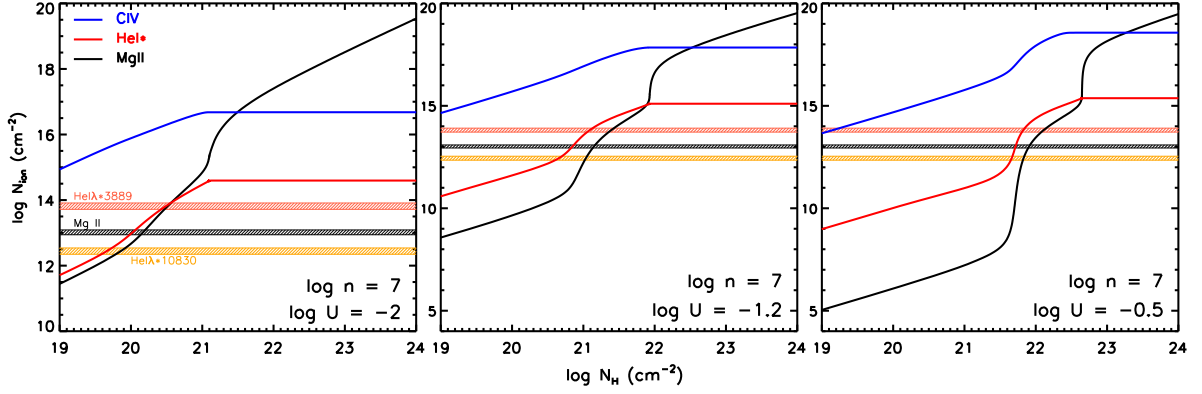
Fig. 16.— Ionization structure in a cloud slab of C IV (blue), Mg II (black) and HeI* (red) calculated by CLOUDY, which depend strongly on ionization parameter (log U). Horizontal shaded stripes represent the ion column density ranges corresponding to the absorption troughs with different widths and with a depth of 0.05, the lower limit by the pair-matching method, for He I*λ3889 (red) , He I*λ10830 (orange), and Mg II (black), respectively.
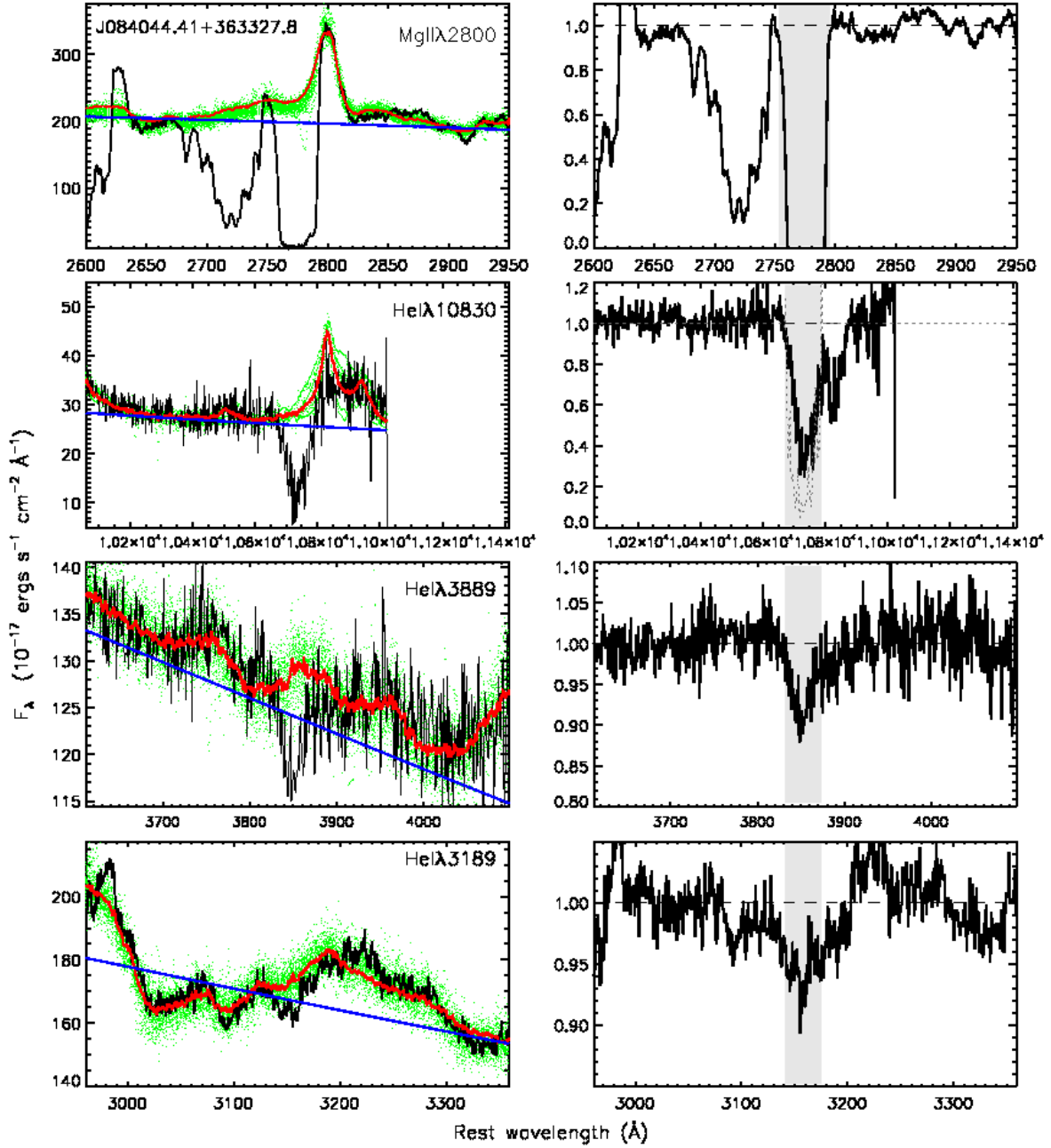
Fig. 17.— *Left*: Demonstration of the absorption troughs in Mg II, He I*$\lambda\lambda$10830, 3889, 3189 (black) of FBQS 0840+3633, and the acceptable fittings (green) and the mean spectrum (red) by the pair-matching method, as well as the intrinsic AGN continuum (blue) determined according to several line-free regions. *Right*: Normalized versions corresponding to the left panels. The gray shades indicate the absorption line regions. The gray dotted line in the second panel from the top shows the He I*λ10830 absorption profile as predicted from the He I*λ3889 absorption trough under the full coverage assumption.
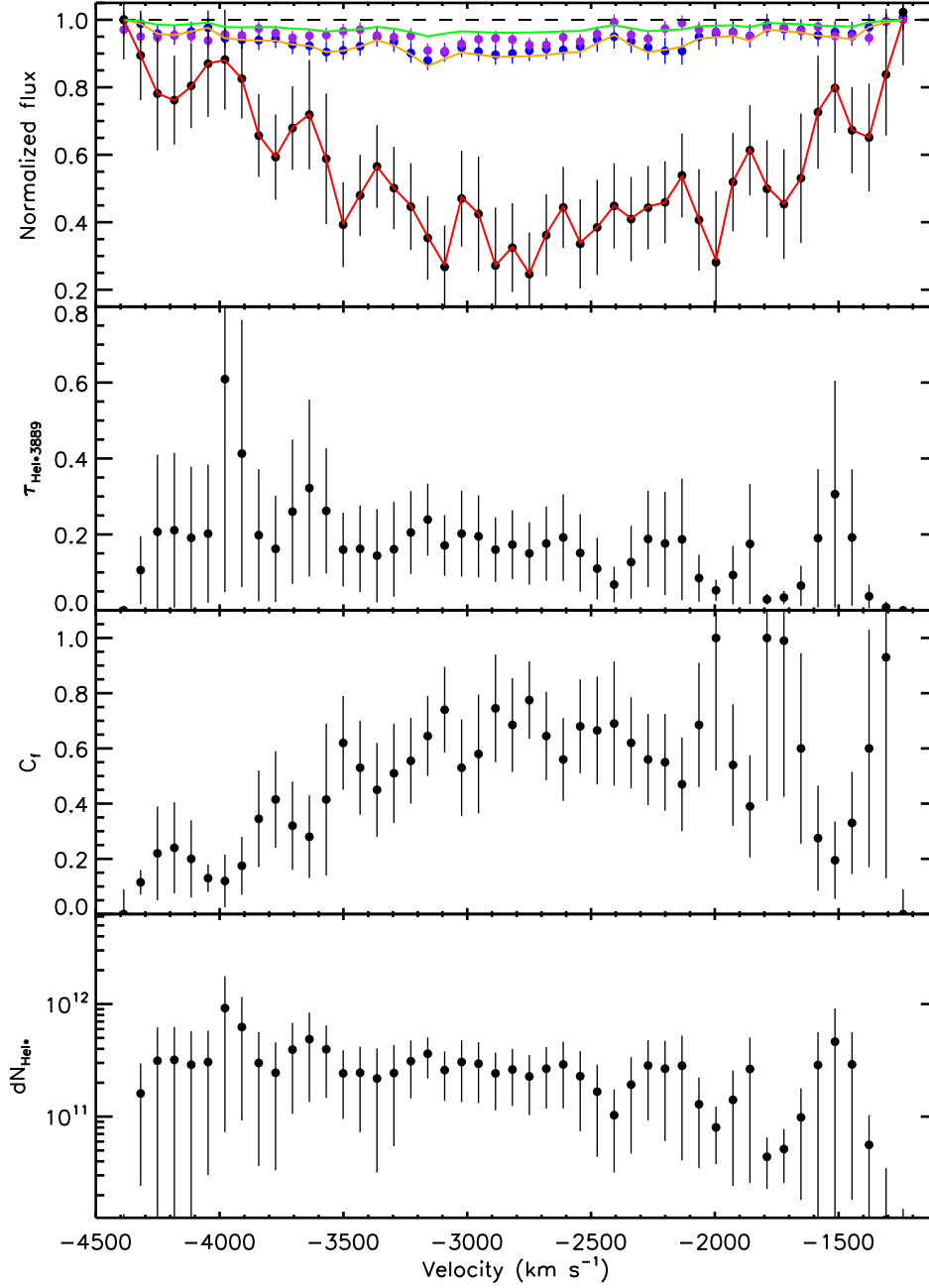
Fig. 18.— Calculation results (top panel) of the He I absorption lines of FBQS 0840+3633 under partial coverage model. The top panel shows the observed profiles with ± 1-σ error bars of He I* $\lambda 3189$ (purple dots), $\lambda 3889$ (blue dots) and $\lambda 10830$ (black dots), and their models as reproduced by the model parameters. The model parameters (the optical depth, covering fraction and column density of the outflow gas) are shown in the other 3 panels as functions of velocity.
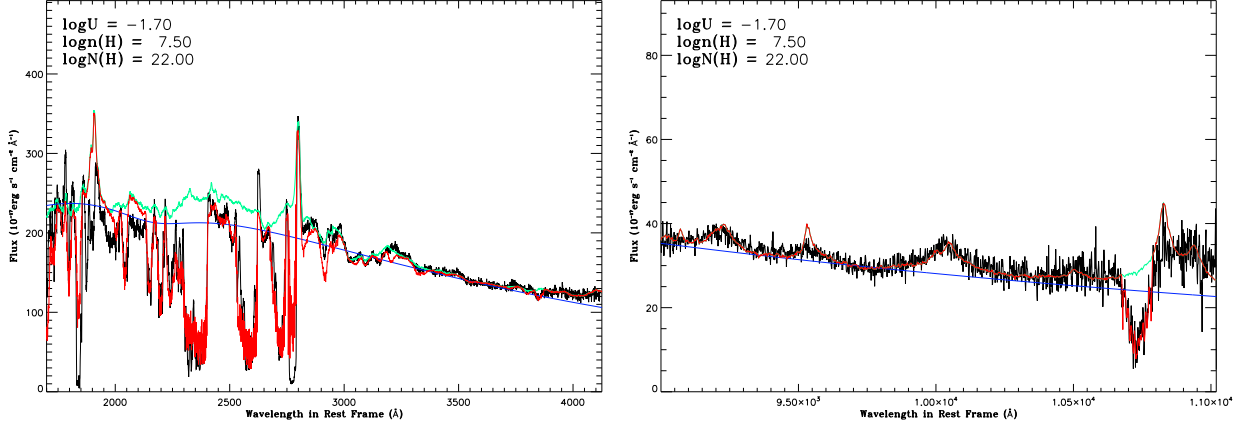
Fig. 19.— Best-fit model for FBQS J0840+3633 by the method of synthetic-spectra fitting, with the model spectra synthesized by CLOUDY.

Table 1.   Physical parameters of known He I* BALs

Object	z	$\log N_{\rm H}$ (cm^{-2})	$\log U$	$\log n_{\rm e}$	$\log N_{\rm HeI*}$	r(kpc)	Ref.
SDSSJ0300+0048	0.89	$\cdots$	$\cdots$	$\cdots$	≤ 14.9	$\cdots$	1
SDSSJ0802+5513	0.664	$21\sim21.5$	-1.8	5	14.73	$0.1\sim0.25$	2
SDSSJ1106+1939	3.038	$22.1^{+0.3}_{-0.1}$	$-0.5^{+0.3}_{-0.2}$	$4.1^{+0.14}_{-0.37}$	$14.68^{+0.23}_{-0.02}$	$0.32^{+0.20}_{-0.14}$	3
FBQSJ1151+3822	0.335	$21.7\sim21.9$	-1.5	5.5-8	14.9	0.0072-0.127	4,5
LBQSJ1206+1052	0.396	$21\sim22$	> -1.5	$6\sim8$	15.01	$\cdots$	6
Mrk231	0.042	22.7	-0.5	3.75	14.96	~ 0.1	7,8
SDSSJ1512+1119[a]	2.106	$21.9^{+0.1}_{-0.1}$	$-0.9^{+0.1}_{-0.1}$	$5.4^{+2.70}_{-0.60}$	$14.84^{+0.03}_{-0.01}$	0.3-0.01	3,9
AKARIJ1757+5907	0.615	> 20.82	>-2.15	3.8	14.2	>3.7	10
NVSSJ2359-1241	0.868	20.556	-2.418	4.4	14.14 ± 0.3	1.3 ± 0.4	11,12,13

References. — (1) Hall et al. (2003); (2) Ji et al. (2014); (3) Borguet et al. (2013); (4) Leighly et al. (2011); (5) Lucy et al. (2014); (6) Ji et al. (2012) ; (7) Rudy et al. (1985); (8) Leighly et al. (2014); (9) Borguet et al. (2012); (10) Aoki et al. (2011); (11) Arav et al. (2008); (12) Korista et al. (2008); (13) Bautista et al. (2010)

[a]For SDSSJ1512+1119, we show the physcial properties of component 2 (C2) of absorption trough, which is associated with He I* absorption lines (see Figure 4 in Borguet et al. (2013)).

Table 2.   Absorption Line information

Ion	λ (Å) Vacuum	f_{ik}	E_{low} cm^{-1}	E_{up} cm^{-1}	g_{low}	g_{up}
He I*	2764.63	0.004	159856	196027	3	9
He I*	2829.91	0.007	159856	195193	3	9
He I*	2945.96	0.012	159856	193801	3	9
He I*	3188.67	0.028	159856	191217	3	9
He I*	3889.75	0.064	159856	185565	3	9
He I*	10833.1	0.539	159856	169087	3	9
Mg II	2796.35	0.608	0	35761	2	4
Mg II	2803.53	0.303	0	35669	2	4
C IV	1548.20	0.190	0	64592	2	4
C IV	1550.77	0.095	0	64484	2	4

Table 3. The parent sample of Mg II BAL Quasars in the SDSS DR5

SDSS Name[a]	z	Spectrum[b]	Mg II[c] EW (Å)	Mg II[d] AI (km s^{-1})	Mg II[e] d_{abs}	Mg II[f] v_{max} (km s^{-1})	Mg II[g] v_{min} (km s^{-1})	Mg II[h] v_{avg} (km s^{-1})	Mg II[i] S/N	Ref.
J000009.26+151754.5	1.197	52251-0751-354	10.15±0.86	1282	0.80	-4104	-126	-1457	9.1	T06,Z10
J002623.78+135523.5	1.319	52233-0753-002	24.81±1.71	2547	0.45	-17685	-6550	-11943	14.0	T06,G09,Z10
J004610.17+000449.7	0.826	52199-0691-494	4.92 ±1.20	391	0.33	-1846	567	-699	10.3	Z10
J005722.48+010101.8	1.146	51783-0395-417	3.75 ±0.66	420	0.40	-5249	-3001	-4204	11.3	T06,Z10
J010352.46+003739.7	0.705	51816-0396-471	5.34 ±0.44	556	0.28	-11571	-8433	-10071	23.7	T06,G09,Z10
J011117.34+142653.6	1.155	51821-0423-310	4.51 ±0.51	510	0.39	-4427	-2652	-3614	20.3	T06
J013816.16+140431.6	0.877	51882-0426-494	6.25 ±1.08	657	0.64	-5167	-2850	-4050	6.6	T06
J013853.94-101125.7	1.305	52145-0663-217	7.86 ±1.07	702	0.29	-10090	-5311	-7844	16.8	T06,G09,T06
J014012.07+130241.8	1.188	51882-0426-081	8.30 ±1.21	887	0.55	-4994	-2196	-3697	5.4	T06,G09
J014534.36+143136.9	0.636	51820-0429-372	4.67 ±0.84	517	0.50	-1888	-29	-1016	10.1	T06
J014950.96-010314.1	1.082	51793-0402-260	4.69 ±0.50	467	0.25	-9342	-5841	-7640	27.3	T06,Z10
J015636.03+135212.3a	1.129	51900-0427-354	7.70 ±0.83	877	0.73	-4044	-2267	-3209	10.0	T06,Z10
J015636.03+135212.3b	1.129	51900-0427-354	5.06 ±0.95	456	0.54	-6420	-4793	-5603	10.0	T06,Z10
J020105.14+000617.9	1.205	51871-0403-593	6.47 ±0.76	643	0.34	-3684	715	-1827	23.4	T06,G09,Z10
J023102.49-083141.2	0.587	51908-0454-582	5.36 ±0.91	552	0.30	-4939	-1660	-3167	12.9	T06,G09,Z10

(This table is available in its entirety in a machine-readable form in the online journal. A portion is shown here for guidance regarding its form and content.)

[a]The SDSS designation, hhmmss.ss+ddmmss.s (J2000). Sources with the same designation but postfixed with a/b/c denote sources with multiple Mg II absorption components.

[b]The SDSS spectra are designated as mjd-plate-fiberid.

[c]The total error σ_{total} as defined in §2.2 .

[d]Absorption Index (AI) measured according to the definition of Zhang et al. (2010).

[e]Maximum depth of Mg II absorption troughs.

[f]Maximum velocity of Mg II absorption troughs from the zero velocity.

[g]Minimum velocity of Mg II absorption troughs from the zero velocity.

[h]Weighted average velocity of Mg II BAL troughs.

[i]Median signal to noise (S/N) in the range 2400–3000 Å.

Table 4. The He I* λ3889 BAL Quasars

SDSS Source[a]	z	Spectrum[b]	He I EW (Å)	He I[c] d_{abs}	He I[d] v_{max} (km s^{-1})	He I[e] v_{min} (km s^{-1})	He I[f] v_{avg} (km s^{-1})	He I[g] S/N
000009.26+151754.5	1.197	52251-0751-354	2.57 ±1.13	0.35	-1821	-445	-1024	4.7
010352.46+003739.7	0.705	51816-0396-471	0.67 ±0.29	0.07	-10548	-9614	-10089	30.3
011117.34+142653.6	1.155	51821-0423-310	2.35 ±0.54	0.17	-1598	-290	-1088	16.9
013816.16+140431.6	0.877	51882-0426-494	3.01 ±1.33	0.23	-4734	-2687	-3733	7.4
013853.94-101125.7	1.305	52145-0663-217	2.61 ±1.08	0.25	-7988	-6707	-7281	5.4
014950.96-010314.1	1.082	51793-0402-260	0.51 ±0.21	0.08	-7504	-6897	-7187	20.7
020105.14+000617.9	1.205	51871-0403-593	1.77 ±0.82	0.14	-2702	-1673	-2213	11.1
023102.49-083141.2	0.587	51908-0454-582	1.06 ±0.51	0.13	-2868	-1771	-2377	13.5
023153.64-093333.6	0.555	51908-0454-017	4.00 ±1.43	0.32	-1282	-42	-774	8.5
023445.76-085908.5	1.275	51909-0455-238	3.20 ±1.36	0.33	-8079	-7001	-7608	4.3
024220.10-085332.7	0.800	51910-0456-291	2.00 ±0.73	0.19	-3894	-2665	-3238	14.2
073122.84+430241.0	0.975	53312-1865-044	3.92 ±1.14	0.30	-3962	-2664	-3164	8.8
074554.74+181817.0	1.054	52939-1582-256	1.03 ±0.46	0.14	-1962	-1207	-1665	11.2
075927.12+363431.5	0.983	52238-0757-474	1.24 ±0.56	0.16	-4160	-3341	-3780	12.7
080248.19+551328.8	0.664	53384-1871-440	2.64 ±0.52	0.24	-684	767	52	23.0
080934.64+254837.9	0.545	52670-1205-588	2.00 ±0.31	0.27	-40	790	366	20.0

(This table is available in its entirety in a machine-readable form in the online journal. A portion is shown here for guidance regarding its form and content.)

[a]The SDSS designation, hhmmss.ss+ddmmss.s (J2000). Sources with the same designation but postfixed with a/b is corresponding to that of Mg II in table 3.

[b]The SDSS spectrum is designated by its mjd-plate-fiber.

[c]Maximum depth of He Iλ3889 absorption trough.

[d]Maximum velocity of He Iλ3889 absorption trough from the zero velocity (3889.74 Å).

[e]Minimum velocity of He Iλ3889 absorption trough from the zero velocity (3889.74 Å).

Table 5. He I*λ3189 BAL Quasars

SDSS Name[a]	z	Spectrum[b]	He Iλ3189 EW (Å)	He Iλ3189[c] d_{abs}	He Iλ3189[d] v_{max} (km s^{-1})	He Iλ3189[e] v_{min} (km s^{-1})	He Iλ3189[f] v_{avg} (km s^{-1})	He Iλ3189[g] S/N
J000009.26+151754.5	1.197	52251-0751-354	1.65 ±0.68	0.24	-1539	-437	-894	10.6
J020105.14+000617.9	1.205	51871-0403-593	0.76 ±0.34	0.07	-2968	-1666	-2335	25.0
J023102.49-083141.2	0.587	51908-0454-582	1.20 ±0.59	0.10	-3339	-2107	-2714	14.1
J023153.64-093333.6	0.555	51908-0454-017	1.15 ±0.50	0.15	-1343	-241	-766	9.4
J023445.76-085908.5	1.275	51909-0455-238	1.41 ±0.64	0.16	-7937	-6724	-7380	10.5
J024220.10-085332.7	0.800	51910-0456-291	1.20 ±0.56	0.19	-3682	-2520	-3153	11.4
J073122.84+430241.0	0.975	53312-1865-044	1.12 ±0.48	0.13	-4022	-2725	-3269	11.1
J074554.74+181817.0	1.054	52939-1582-256	0.77 ±0.32	0.14	-1886	-1268	-1583	16.5
J075927.12+363431.5	0.983	52238-0757-474	1.64 ±0.67	0.14	-3811	-2033	-2932	14.6
J080934.64+254837.9	0.545	52670-1205-588	1.42 ±0.38	0.12	106	798	404	19.9
J081820.31+200046.1	0.986	53327-1925-040	0.72 ±0.29	0.10	-2126	-1371	-1735	17.8
J082231.53+231152.0	0.653	53317-1926-546	2.53 ±0.35	0.15	-1811	256	-805	29.9
J083522.77+424258.3	0.807	52232-0762-085	0.59 ±0.17	0.10	-564	58	-249	24.7
J084044.41+363327.8	1.235	52320-0864-149	1.01 ±0.22	0.07	-4448	-2262	-3325	43.8
J084824.14+034542.3	0.699	52224-0564-575	0.85 ±0.41	0.15	-1104	-346	-691	12.3
J085053.12+445122.4	0.542	52605-0897-359	1.55 ±0.53	0.09	-4716	-2532	-3632	31.5
J085215.65+492040.8	0.567	51993-0551-274	1.67 ±0.51	0.22	-1615	-514	-1051	10.8
J085357.88+463350.6	0.549	52238-0764-248	1.04 ±0.37	0.08	-4098	-2458	-3271	20.7
J093759.60+453801.8	0.429	52672-1202-330	1.13 ±0.53	0.08	-1715	-131	-901	14.2
J094355.00+560649.0	1.055	52253-0557-299	1.62 ±0.52	0.18	-1545	-443	-966	12.5
J102839.11+450009.4	0.585	52990-1429-401	0.49 ±0.21	0.13	-1054	-503	-806	33.3
J102943.75+370127.2	1.344	53415-1957-601	1.98 ±0.78	0.37	-997	176	-452	5.1
J103255.37+083503.2	0.894	52734-1240-316	0.68 ±0.29	0.07	-3398	-2782	-3094	23.3
J104459.60+365605.1	0.701	53463-2090-329	0.40 ±0.16	0.05	-4413	-3458	-3936	30.3
J104705.08+590728.4	0.392	52427-0949-326	1.28 ±0.49	0.18	-1380	690	-474	7.9
J104845.83+353110.7	1.011	53463-2090-131	0.95 ±0.31	0.08	-3365	-2681	-3030	23.8

Table 5—Continued

SDSS Name[a]	z	Spectrum[b]	He Iλ3189 EW (Å)	He Iλ3189[c] d_{abs}	He Iλ3189[d] v_{max} (km s^{-1})	He Iλ3189[e] v_{min} (km s^{-1})	He Iλ3189[f] v_{avg} (km s^{-1})	He Iλ3189[g] S/N
J105404.72+042939.3	0.579	52338-0579-072	1.95 ±0.69	0.26	-1499	-329	-870	5.7
J105638.08+494943.3	1.148	52669-0876-110	0.45 ±0.18	0.05	-11546	-10681	-11134	36.5
J111628.00+434505.8	0.801	53061-1364-095	1.04 ±0.25	0.09	-4636	-3204	-3901	22.8
J114043.62+532438.9	0.530	52734-1015-085	2.45 ±0.67	0.15	-2704	-850	-1873	11.6
J115553.87+012427.6	1.010	52051-0515-043	1.87 ±0.51	0.12	-5277	-2755	-4074	20.5
J120924.07+103612.0	0.395	52723-1229-489	1.77 ±0.19	0.10	-1548	383	-662	40.7
J122614.97+120925.4	0.871	53120-1614-145	3.17 ±0.40	0.28	-1768	-392	-1164	18.1
J122703.19+505356.2	0.765	52644-0971-459	0.85 ±0.33	0.09	-1276	-657	-1001	10.2
J124300.87+153510.6	0.562	53502-1769-584	1.46 ±0.36	0.10	-1466	673	-423	14.6
J130952.89+011950.6	0.547	52295-0525-250	0.69 ±0.20	0.09	-630	405	-103	28.0
J135226.34+024549.4	1.222	52026-0530-588	1.71 ±0.67	0.13	-3879	-2375	-3077	13.1
J142647.47+401250.8	0.749	52797-1349-348	1.40 ±0.55	0.14	-3700	-2401	-2974	8.8
J142927.28+523849.5	0.595	52781-1327-343	2.53 ±0.34	0.14	-5431	-2226	-3954	23.0
J143144.91+391910.2	1.091	52797-1349-257	1.21 ±0.41	0.10	-1560	-1147	-1396	20.5
J150847.41+340437.7	0.788	53108-1385-173	1.46 ±0.22	0.17	-1202	109	-606	27.3
J151053.63+574055.1	1.037	52079-0612-424	1.15 ±0.31	0.09	-5656	-3889	-4706	25.6
J153036.83+370439.2	0.417	53144-1401-367	2.73 ±0.39	0.14	-4621	-2025	-3263	19.2
J153646.88+515755.2	1.132	52378-0795-095	1.78 ±0.58	0.13	-5613	-3641	-4711	16.9
J155905.39+250047.2	0.933	53523-1655-085	1.15 ±0.42	0.17	-1811	-159	-1047	9.6
J160329.72+502722.2	0.638	52375-0620-126	2.16 ±0.93	0.17	-4599	-2826	-3596	9.7
J163255.46+420407.8	0.728	52379-0816-569	2.30 ±0.76	0.18	-2929	-526	-1858	11.3
J163656.84+364340.4	0.852	52782-1174-337	5.62 ±0.95	0.39	-5919	-3266	-4303	9.5
J171032.23+214451.3	0.867	53177-1689-069	1.46 ±0.44	0.18	-2041	-45	-1243	12.6
J210757.67-062010.6	0.644	52174-0637-610	2.41 ±0.27	0.17	-1741	464	-509	30.2
J214118.78-070957.4	0.869	52824-1177-484	2.50 ±0.91	0.25	-3853	-2349	-3236	8.1
J232550.73-002200.4	1.011	51818-0383-142	0.89 ±0.30	0.09	-2419	-1320	-1846	21.9

Table 6.   Low-z BAL AGNs

SDSS Name	z	Spectrum	He I*λ3889 EW (Å)	He I*λ3889 d_{abs}	He I*λ3889 v_{max}(km s^{-1})	He I*λ3889 v_{min}(km s^{-1})	He I*λ3889 v_{avg}(km s^{-1})	He I*λ3889 S/N
J013117.14+162535.5	0.274	55833-5137-627	2.54±0.68	0.27	-1805	-291	-897	15.19
J014219.00+132746.5	0.267	51820-0429-303	3.17±0.35	0.23	-621	553	-57	26.49
J075217.84+193542.2	0.117	52939-1582-612	1.78±0.23	0.10	-661	444	-94	43.72
J081527.29+445937.4	0.268	51877-0439-034	3.06±0.65	0.14	-3398	-515	-2180	17.89
J081542.53+063522.9	0.244	52934-1295-580	1.98±0.72	0.09	-5106	-1485	-3303	21.14
J081652.88+241612.5	0.276	52962-1585-178	0.70±0.25	0.06	-7291	-6278	-6790	28.11
J092247.03+512038.0	0.161	52247-0766-614	0.95±0.32	0.06	-7421	-6611	-7035	26.16
J093653.84+533126.8	0.228	52281-0768-473	1.20±0.22	0.11	-1404	-302	-851	34.85
J101325.43+221229.4	0.275	53739-2365-389	0.69±0.36	0.07	-7524	-6647	-7099	29.39
J105311.38+261522.6	0.249	53793-2357-388	1.32±0.27	0.16	-1249	-422	-826	20.85
J113804.88+400118.9	0.292	53466-1972-484	1.48±0.50	0.22	-838	-218	-503	12.01
J130534.49+181932.8	0.118	54479-2603-443	1.86±0.13	0.24	-1023	-196	-563	34.66
J130712.33+340622.5	0.148	53476-2006-628	2.21±0.30	0.16	-1856	-66	-896	21.18
J134704.91+144137.6	0.135	53858-1776-612	1.39±0.19	0.16	-7510	-6498	-6996	41.80
J140136.63+041627.2	0.164	52339-0856-010	0.84±0.27	0.09	-7479	-6399	-6918	24.73
J153539.25+564406.5	0.208	52072-0617-352	2.82±0.21	0.20	-1939	-425	-984	25.86
J163459.82+204936.0	0.129	53224-1659-542	4.70±0.49	0.34	-4498	-2860	-3638	15.53
J215408.71-002744.4	0.218	52078-0371-106	2.75±0.58	0.17	-2438	-307	-1211	17.68
J222024.58+010931.2	0.213	52140-0375-361	5.44±0.36	0.42	-1672	-88	-724	31.15

A.   Appendix material

A.1.   Overview of existing Mg II BAL samples

As descried in §2.1, we combine the Mg II BAL quasars in the T06, G09 and Z10 samples, from which a parent sample of 285 objects is built. Below we overview and compare those three samples.

The traditional definition for C IV BAL, "balnicity index" (BI), was first introduced by Weymann et al. (1991), which is defined as

$$BI \equiv \int_{v_l=3,000}^{v_u=25,000} [1 - \frac{f(-v)}{0.9}] \, C \, dv \;, \tag{A1}$$

where f(v) is the continuum-normalized spectral flux. The dimensionless factor C is initially set to 0, and changes to 1 only when an absorption trough continuously dips 10% or more below the estimated continuum over an interval of 2000 km s^{-1}. $BI = 0$ means no BAL, while a positive BI indicates not only the presence of one or more BAL troughs but also the strength of the total absorption. Using BI-based criteria and spectroscopic data set from the SDSS DR5, G09 identified 5039 BAL quasars. In their work, the v_l in the BI definition was simply revised to be 0 km s^{-1} instead of the blueshifted 3000 km s^{-1}, to avoid omitting the BAL features at low outflow velocities.

T06 identified 4784 quasars in the SDSS DR3 quasar catalog Schneider et al. (2005). In their work, a different definition of BALs, termed "intrinsic absorption index" (AI), was devised; the original definition of AI was first introduced by Hall et al. (2002) to select LoBAL quasars. AI is essentially an equivalent width (EW) to measure all the absorption flux within the absorption trough. The definition of T06 is as follow,

$$AI \equiv \int_{v_l=0}^{v_u=29,000} [1 - f(-v)] \, C' \, dv \tag{A2}$$

where f(v) is the normalized template-subtracted flux spectrum. $C'(v) = 1$ in continuous troughs that exceed the minimum depth (10%) and the minimum width (1000 km s^{-1}); otherwise, $C'(v) = 0$.

Z10 have searched specifically for Mg II BAL quasars in the SDSS DR5 data set, and obtained 68 Mg II BAL quasars at $0.4 \leq z \leq 0.8$, with a median S/N ≥ 7 pixel^{-1} of the SDSS spectra. They used an AI-based selection criteria, with setting a maximum velocity of Mg II BALs to 20,000 km s^{-1}, and a minimum velocity width of 1600 km s^{-1}. The latter is a trade-off between the completeness and consistency with respect to the canonical definition (i.e., the velocity width of the trough being ≥ 2000 km s^{-1}). Because the published Mg II BAL quasars in Z10 are only at $0.4 \leq z \leq 0.8$, we use the same pipeline of Z10 to enlarge this sample to 175 Mg II BALs at redshifts of $0.4 \leq z \leq 1.35$ in the SDSS DR5.

For the ease of comparison, we select only the sources in those samples satisfying the following criteria: (1) from the SDSS DR3 only, which is common in the three samples; (2) with median spectral S/N > 7 pixel^{-1}; (3) the width of the continuous Mg II absorption trough $\geq$ 2000 km s^{-1}, which is the strictest BAL width criterion among the three samples. The thus culled samples have 106 (T06), 77 (G09), and 70 (Z10) sources, respectively. Forty-nine sources are common in the three samples and the combined sample have 134 sources in total. Thirty-three percent objects of T06, 19.5 percent of G09, and 11.4 percent of Z10 are rejected by the other two samples respectively (See Figure 20). This indicates the degree of incompleteness of the samples caused by different selection procedures and criteria.
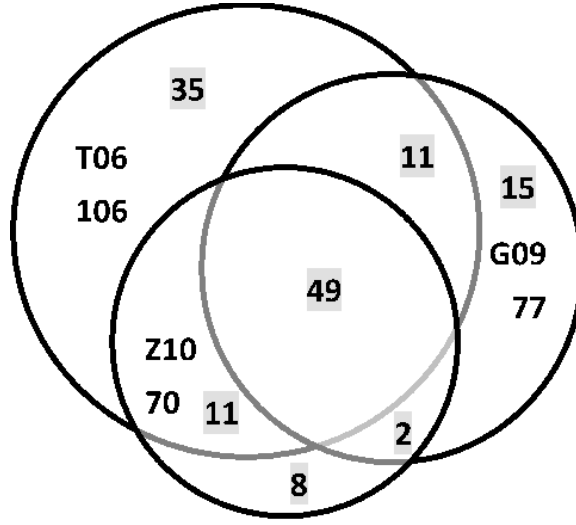

Fig. 20.— Venn diagram displaying the relationships of the Mg II BAL quasars among the T06, G09 and the original Z10 samples. The sources of the three samples used here are reselected according to the same BAL criteria based on our measurements (see § 2.1). The numbers with a shaded box denote the number of sources in every minimum regions enclosed by the arcs.

A.2.   Reliability of the pair-matching method

We perform a series of tests to evaluate the pair-matching method. The tests aim at three aspects: to identify the major factors influencing the BAL measurements, to assess the efficiency of our selection procedure (particularly the completeness of the thus selection sample), and to check the accuracy of our measurements of BAL parameters (namely, assessing the total error σ_{tot} and the systematic error σ_{sys} described in §2.2).

According to the BAL definitions (BI and AI; see Appendix A.1), the depth (d_{abs}) and width (W_{abs}) of absorption troughs are the two quantities that impact the BAL measurement. Obviously,

the spectral S/N is another influencing factor to any measurements. So in the following tests, we focus on evaluating the three factors.

We carry out the tests using Monte Carlo simulations, first for the parent Mg II BAL sample and then for the He I* BAL sample. We generate 200 spectra for each (S/N, d_{abs}, W_{abs}) grid, by randomly combining a BAL spectrum to an unabsorbed quasar spectrum. Firstly, for simplicity the BAL spectra are assumed to be of Gaussian profile, with the centroid values (namely the blueshifted offset relative to the emission line) following the distribution of the parent Mg II BAL sample. The distributions in every d_{abs} and W_{abs} intervals also follow the observed distributions of the parent Mg II BAL sample. The first d_{abs} bin is [0.05, 0.1], and the rest range from 0.1 to 0.9 with a bin size of 0.1. The W_{abs} bins are centered at 1600, 2000, 4000, 6000, 8000 and 10000 km s^{-1}. The blueshift of absorption line is fixed at -5000 km s^{-1}, since the v_{avg} of Mg II and He I* absorption roughs are mainly between -10000 $\sim$ 0 km s^{-1}. We will also adopt actual absorption profiles later. The unabsorbed quasar spectra are selected from the SDSS DR7 data set, with decent spectral S/N. Gaussian noises may be added to the generated spectra to meet the S/N of every bins. The S/N bins are [5,10], [15,20], [25,30] and [35,40], covering the spectral S/N range of our sample.

Then we apply the pair-matching method to the simulated spectra, using the same procedure as described in § 2.2. Based on the fitting results of all the (S/N, d_{abs}, W_{abs}) grids, we can evaluate the measurement uncertainties, the detection ability, etc., as functions with the three influencing factors. First of all, we analyze the fitting results of the 200 spectra in every single grids. We consider the relative difference between the input absorption EW (EW_i) and the recovered one (EW_o), $\frac{EW_o - EW_i}{EW_i}$. These relative differences in every grids turn out to be normally distributed, which is illustrated in Figure 21. This figure, with the blueshift of absorption lines being fixed to be -5000 km s^{-1}, shows the histograms of $\frac{EW_o - EW_i}{EW_i}$ in the 2-dimensional parameter space of S/N and d_{abs}. We can see that basically it is normally distributed. The other grids are all a similar situation. The dispersion of $\frac{EW_o - x_i}{EW_i}$ is essentially the relative total error of the absorption EW, namely σ_{tot}/EW (see §2.2). The 90% confidence interval is taken as the measurement uncertainty of the pair-matching method, which is set by matching the actually calculated σ_{tot} for the Mg II BAL quasars (see §2.2 and Table 2). Such a confidence interval (namely 1.6-σ instead of the commonly used 1-σ) should be caused by the effects of other—albeit minor—factors (e.g., the profile shape of absorption troughs). The mean of the derived systematic errors (σ_{sys}) of the 200 fittings of a grid is regarded as the typical σ_{sys} of that grid. The detection probability is straightforward to define as the recovered fraction of BALs out of the 200 spectra in every grids.

The relative total error and detection probability as functions of S/N, d_{abs} and W_{abs} are shown in Figure 22 (left panel) for Mg II BALs. We can clearly see that the relative total error decreases, and the detection probability increases, with both increasing S/N and d_{abs}, while the effect of W_{abs} is not so significant. Therefore we can reasonably conclude that the spectral S/N and the absorption

depth are the two most principal factors influencing the pair-matching method. That is why we consider the S/N–d_{abs} plane only, by collapsing the W_{abs} dimension, in Figure 4. The detection probability of the pair-matching method is almost complete for Mg II BALs with S/N > 35 or d_{abs} > 0.5. Figure 22 shows σ_{sys} and σ_{sys}/EW as functions with S/N, d_{abs} and W_{abs}. σ_{sys} increases with W_{abs} in every grids of (S/N, W_{abs}), yet is less sensitive to S/N and d_{abs}. However, similar to what the relative total error, σ_{sys}/EW bears a positive dependence on d_{abs}, although the dependence on S/N is not so significant.

The above conclusions are based on the simulated spectra with BALs assumed to be of Gaussian profile. Now we build simulated spectra with actual absorption lines from the parent Mg II sample. The BAL spectra are normalized and the lines are corrected into zero velocity shift. Consistent with the above W_{abs} bins, we categorize the Mg II BAL spectra into six subsamples. Then we build an arithmetic mean composite spectrum of normalized Mg II BALs for each, using the composite spectrum method of Dong et al. (2010). The composite spectra have very high S/N, and serve as the templates of Mg II BAL profiles for the six W_{abs} bins (see the upper panel of Figure 24). Following the procedure in the case of Gaussian profile, a series of simulated spectra are generated for all the 3-dimensional grids of (S/N, d_{abs}, W_{abs}), and the pair-matching method is applied to them. The results are also shown in Figures 22, 23 and 4. The general trends are almost the same as in the case of Gaussian profile. This confirm that the most principal influencing factors to the pair-matching method are S/N and d_{abs}.

We repeat the above tests for for He I* λ3889 absorption. To fully cover the measured parameter space of the He I* BALs, the grids in the tests are are 0.05, 0.1, 0.2, 0.3, 0.4, 0.5 for d_{abs}, 500, 1000, 1500, 2000, 3000 km s^{-1} for W_{abs}. The centroid of the He I* absorption line is simply fixed to be the blueshifted 5000 km s^{-1}, the typical blueshift of the Mg II BALs of the parent sample. The test results are illustrated in Just like the tests for Mg II, both Gaussian profiles and actual profiles (Figure 24, bottom panel) for the simulated BAL spectra are tried. The test results are illustrated in Figures 4, 22 and 23, which are similar to the case for Mg II BAL quasars.

As to testing the possibility of false identification of He I* λ3889 BALs , the most reliable way is to observe other He I* absorption troughs at corresponding velocities. In our He I* λ3889 BAL sample, the He I*λ3189 absorption line is detected in over half the sample from the SDSS spectra. Moreover, in our follow up NIR observations, 5 of 5 He I* λ3889 BAL quasars (100%) have the expected He I*λ10830 BALs (see also §2.3 and Appendix A.6). Thus the false identification rate should be very low. More NIR observations of He I*λ10830 are needed to investigate this issue.
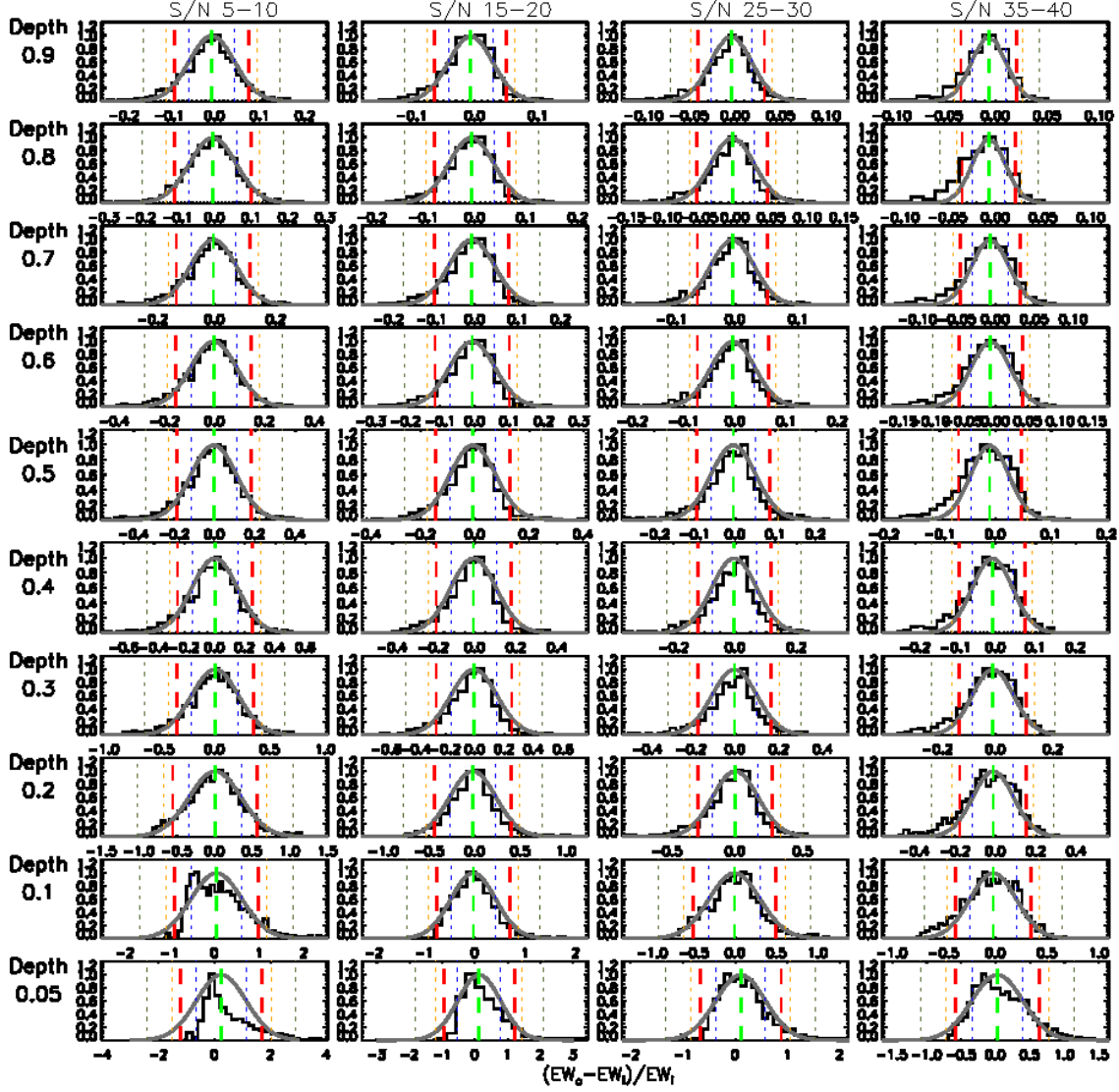
Fig. 21.— Histograms of the relative difference between input and output EW of the Mg II BALs, $\frac{EW_o - x_i}{EW_i}$, in every 2-dimensional grids of spectral S/N and absorption depth (d_{abs}) with the absorption blueshift being fixed to -5000 km s^{-1}. In every panels, the green dashed line denotes the mean value of the distribution, which is almost zero; the blue, orange and gray dotted lines denote the measured 1-σ (standard deviation), 2-σ and 3-σ of the distribution, respectively; the red dashed line denotes the 1.6-σ, which corresponds to the 90% confidence level and is regarded as the relative total measurement uncertainty (namely σ_{tot}/EW) of the pair-matching method. Note that, except for the panel of the shallowest width and poorest S/N, the distributions are close to Gaussian (dark gray lines).
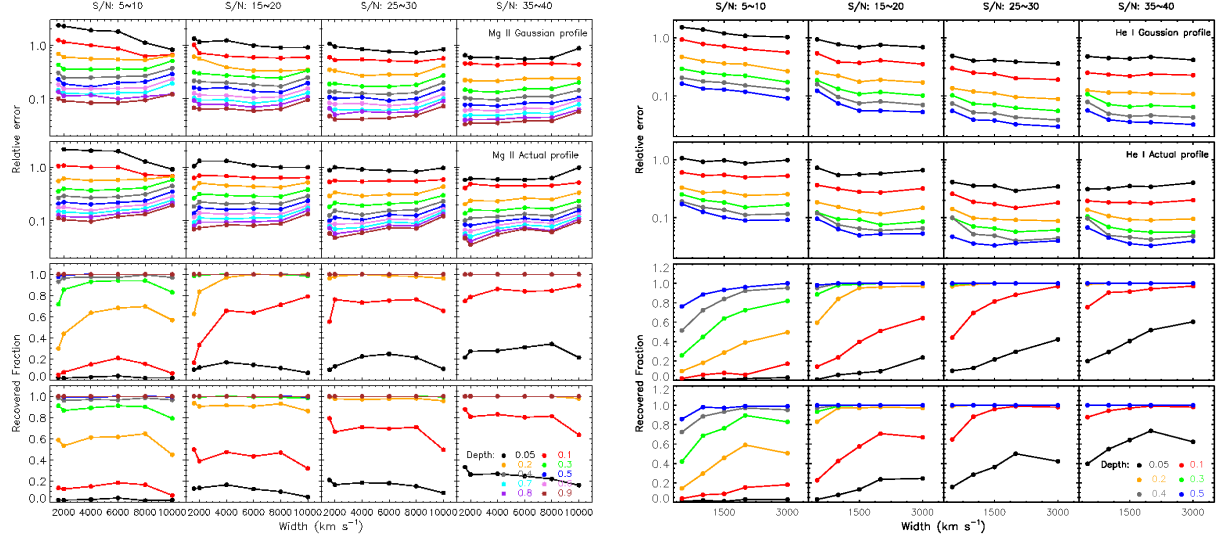
Fig. 22.— Relative total errors (measure of σ_{rmtot}/EW; the top 2 rows) and the recovered fraction (the bottom 2 rows) as functions of the spectra S/N, and depth and width of the BALs, for Mg II (*left*) and for He I* λ3889 (*right*). Rows 1 and 3 from the top are for the tests with simulated BAL of Gaussian profiles; the other 2 rows are of actual BAL profiles. Different absorption depths are denoted with different colors.

Fig. 23.— The same as Figure 22, but for the systematic error (σ_{sys}) and the relative systematic errors (σ_{sys}/EW) .
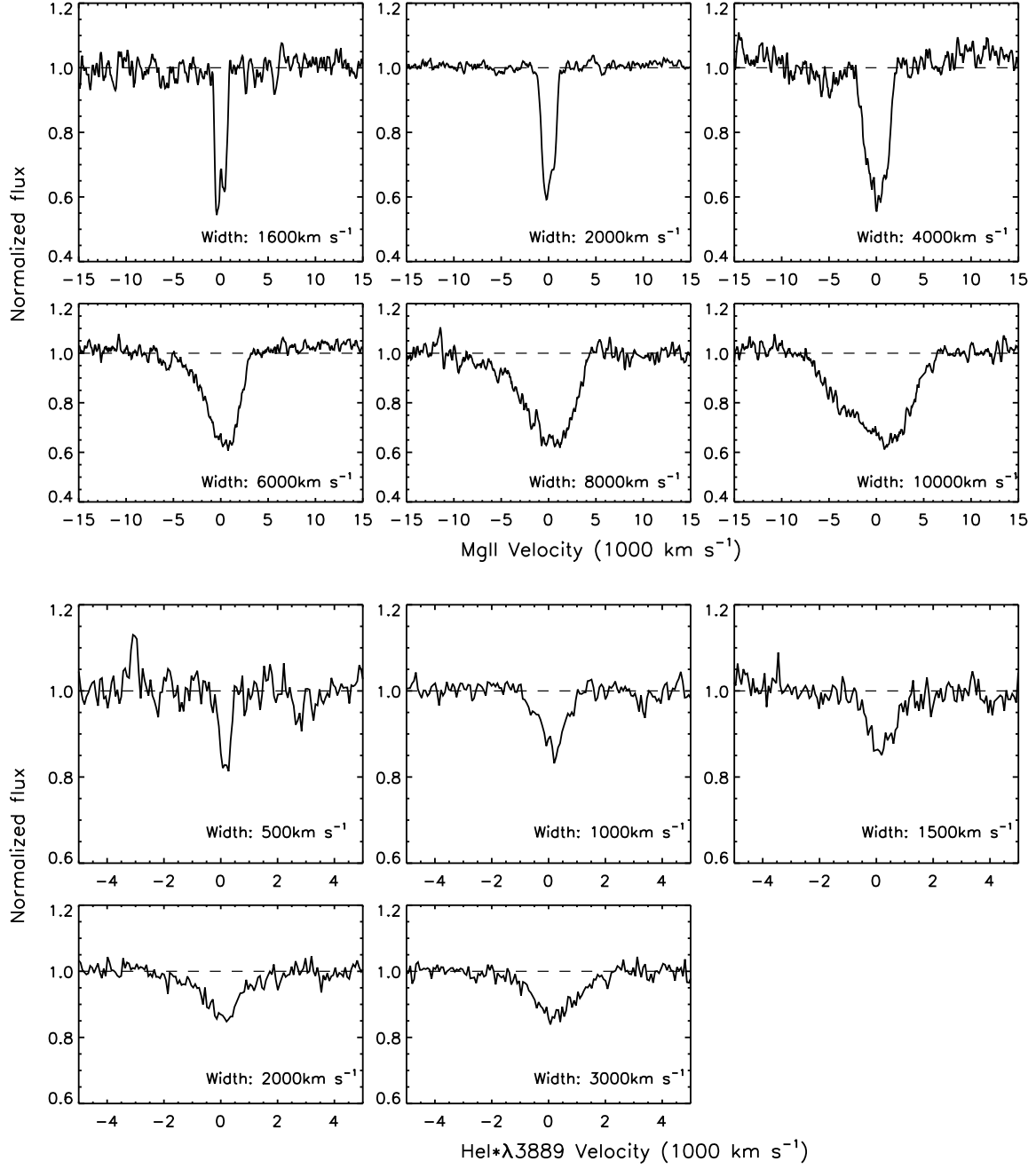
Fig. 24.— Composite normalized absorption-line spectra for Mg II (*top*) and He I*λ3889 (*bottom*), serving as templates of BAL profiles of different absorption widths in the tests.

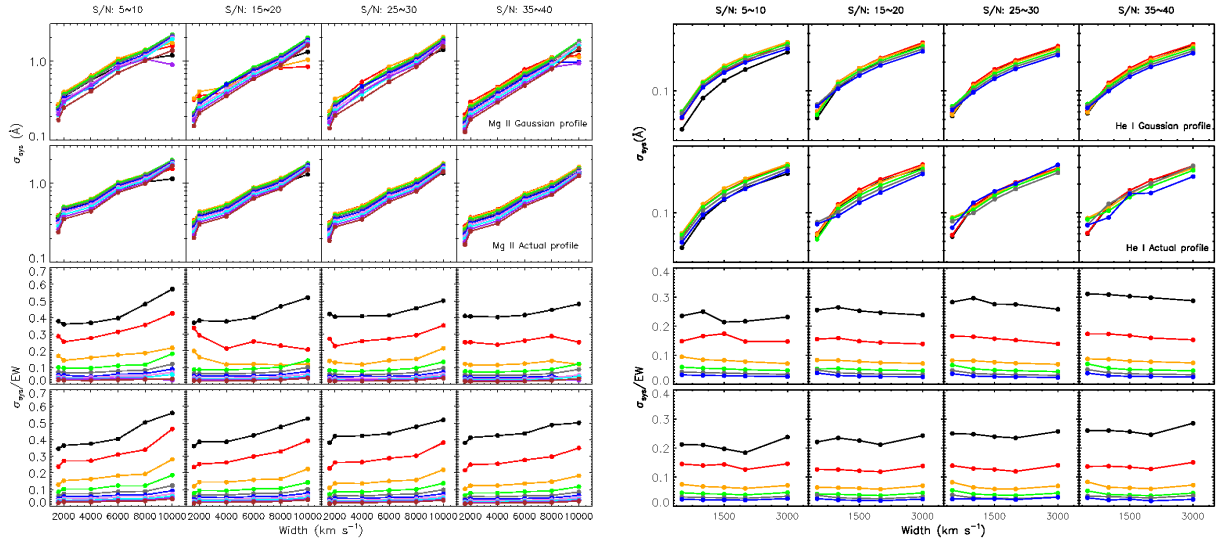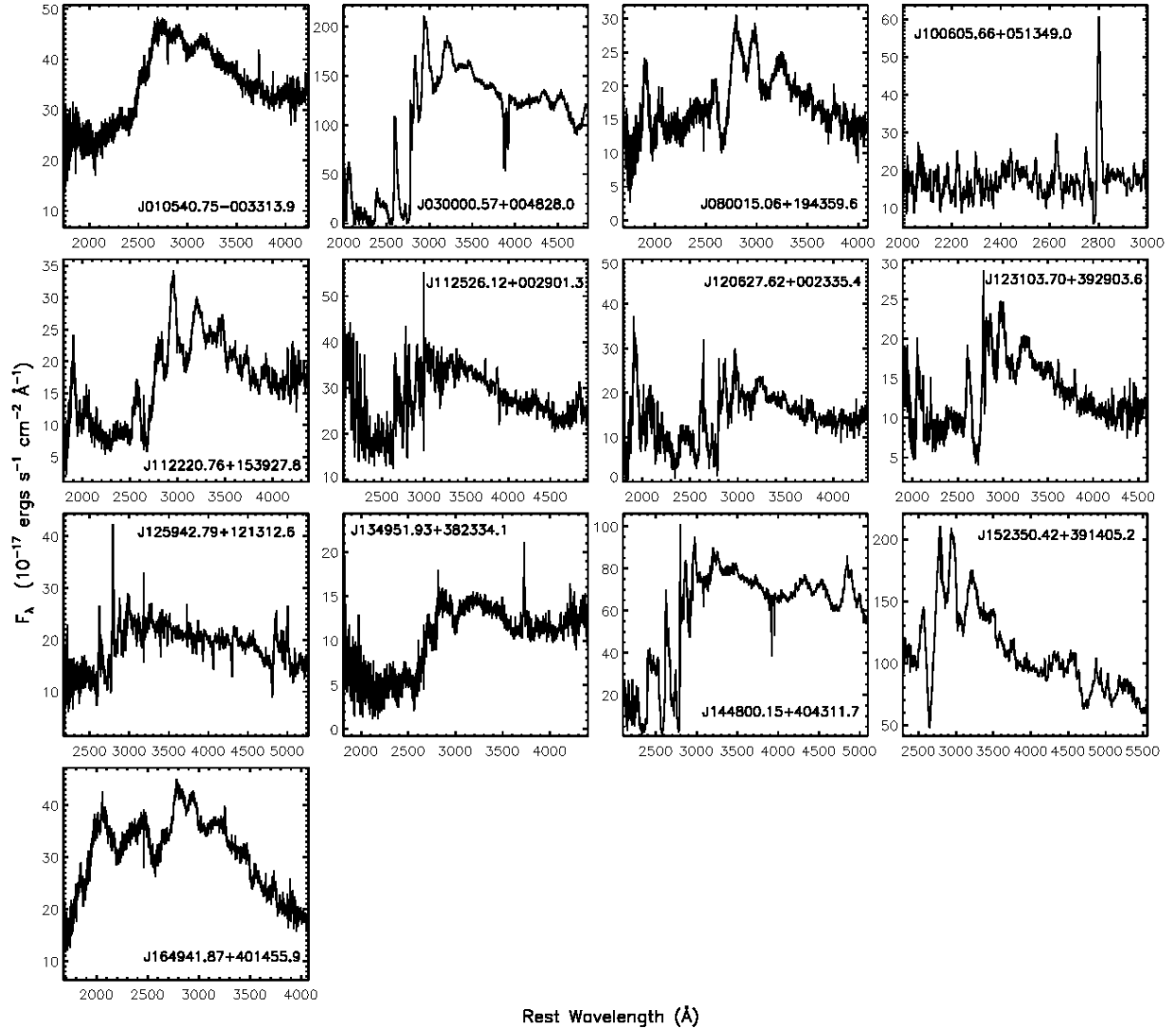Fig. 25.— Mg II BAL quasars with unusual spectral features. These spectra are smoothed by 5-pixel boxcar.

A.3. Unusual quasars not included in our parent sample

Thirteen sources compiled as Mg II BAL quasars in the T06, G09 or Z10 samples show unusual spectra features. It is difficult to use our pair-matching method to recover their unabsorbed spectra. Here we list those quasars in Table 7, and their SDSS spectra are shown in Figure 25. Among them, J010540.75−003313.9, J030000.57+004828.0, and J112526.12+002901.3 have been investigated in detail by Hall et al. (2002); for J112526.12+002901.3, we have studied recently the physical conditions of its outflow gas using the method mentioned in §4.2 Shi et al. (2014).

A.4. UV and optical measurements for the parent sample

The analysis for the near-UV spectra is performed with the routine described detailedly in Wang et al. (2009). Here the pseudocontinuum consists a local power-law continuum, an Fe II template, but also an additional component for the Balmer continuum, which is assumed to be produced in partially optically thick clouds with a uniform temperature. The Fe II emission is modeled with the semi-empirical template for I Zw 1 generated by Tsuzuki et al. (2006). To match the width and possible velocity shift of the Fe II lines, the template is convolved with a Gaussian and is shifted in velocity space. Each of the lines of the Mg II doublet is modeled with two components, one broad and the other narrow. The broad component is fit with a truncated, five-parameter Gauss-Hermite series; a single Gaussian is used for the narrow component. The fitting results for the entire Mg II BAL sample are summarized in Table 8.

For the optical spectra of the objects at $z < 0.8$, the fitting is performed with the routine described detailedly in Dong et al. (2008). In the spectra of these BAL quasars the starlight is negligible. As the broad emission lines, particularly the Fe II multiplets, are so broad and strong that they are in blend and essentially leave no line-free wavelength regions, so we fit the nuclear continuum, the Fe II multiplets, and other emission lines simultaneously. The AGN continuum is approximated by a single power law with a free index. The optical Fe II emission is modeled with two separate sets of analytic spectral templates, one for the broad-line system and the other for the narrow-line system, constructed from measurements of I Zw 1 by Véron-Cetty et al. (2004). Within each system, the respective set of Fe II lines is assumed to have no relative velocity shifts

Table 7. Unusual Mg II BAL quasars not included in the parent sample

SDSS NAME	z	MJD	Plate	Fiberid	He I* Detection	Source
J010540.75-003313.9	1.179	51816	0396	156	no	T06
J030000.57+004828.0	0.900	51816	0410	621	yes	T06,G09
J080015.06+194359.6	1.252	53315	1922	474	no	G09,Z10
J100605.66+051349.0	0.968	52641	0996	243	yes	T06,G09
J112220.76+153927.8	1.109	53383	1753	404	no	G09
J112526.12+002901.3	0.863	51614	0281	427	yes	T06,G09
J120627.62+002335.4	1.114	51999	0286	499	yes	T06,G09
J123103.70+392903.6	1.004	53466	1992	529	no	G09
J125942.79+121312.6	0.752	53473	1695	075	yes	G09,Z10
J134951.93+382334.1	1.094	53460	2014	477	no	G09
J144800.15+404311.7	0.808	53119	1397	198	yes	G09
J152350.42+391405.2	0.658	52765	1293	234	no	T06,G09,Z10
J164941.87+401455.9	1.266	52050	0630	482	no	T06,G09

and the same relative strengths as those in I Zw 1. Emission lines are modeled as multiple Gaussians. Following Dong et al. (2011), we assume that the broad Fe II lines have the same profile as the broad Hβ. The results of the optical fittings for the Mg II BAL quasars at $z < 0.8$ are summarized in Table 9.

Table 8.   UV continuum and emission-line parameters of the entire parent sample

SDSS Name	z	$\beta_{[3k-4k]}$[a]	$\log L3000$ erg s^{-1}	$\log F_{2500}$ ergs s^{-1} cm^{-2} Å^{-1}	$\log F$(UV Fe II) ergs s^{-1} cm^{-2}	FWHM(Mg II^b) [b] km s^{-1}	$\log F$(Mg II^b) [c] ergs s^{-1} cm^{-2}	$\log F$(Mg II^n) [d] ergs s^{-1} cm^{-2}	$\log M_{BH}$ [e] $M_\odot$	L/L_{Edd}
J000009.26+151754.5	1.197	-1.30	45.4	-15.93	-14.40	2435	-14.68	-15.61	8.38	0.51
J002623.78+135523.5	1.319	5.03	45.39	-15.95	-13.47	2812	-14.38	-15.92	8.50	0.46
J004610.17+000449.7	0.826	-1.65	44.96	-15.93	-14.48	7771	-14.39		9.16	0.03
J005722.48+010101.8	1.146	-1.27	45.52	-15.74	-13.91	3239	-14.36	-15.94	8.69	0.33
J010352.46+003739.7	0.705	-0.75	45.43	-15.34	-13.08	2747	-13.66	-15.77	8.50	0.39
J011117.34+142653.6	1.155	-0.25	45.76	-15.64	-13.77	4131	-14.19	-15.91	9.03	0.20
J013816.16+140431.6	0.877	-1.17	44.93	-15.98	-13.97			-16.69		
J013853.94-101125.7	1.305	-1.56	45.47	-15.90	-13.69	2081	-14.39	-15.53	8.28	0.84
J014012.07+130241.8	1.188		45.20	-15.98	-13.90	3036	-14.65	-15.76	8.47	0.35
J014534.36+143136.9	0.636	-0.94	44.63	-15.99	-13.93	1984	-14.93		7.80	0.35
J014950.96-010314.1	1.082	-1.44	45.85	-15.26	-13.14	2622	-14.01		8.68	0.90
J015636.03+135212.3	1.129	-1.40	45.40	-15.90	-13.59	3055	-14.25	-16.12	8.58	0.29
J020105.14+000617.9	1.205	-2.23	45.88	-15.40	-13.66	6453	-13.88	-16.33	9.48	0.14
J023102.49-083141.2	0.587	-1.70	44.83	-15.65	-13.49	2755	-14.36	-15.60	8.19	0.25
J023153.64-093333.6	0.555	-0.74	44.55	-15.96	-14.20	4724	-14.83	-16.22	8.51	0.05

(This table is available in its entirety in a machine-readable form in the online journal. A portion is shown here for guidance regarding its form and content.)

[a]Continuum slope between ~ 3000 Å and ~ 4000Å.

[b]ine widths (FWHM) of broad component of Mg II emission line.

[c]Flux of broad component of Mg II emission line.

[d]Flux of narrow component of Mg II emission line.

[e]Mass of SMBH derived by width of Mg II emission lines, and the formula we used is the equation 10 in Wang et al. (2009).

Table 9.　Optical continuum and emission-line parameters of the $z < 0.8$ objects in the parent sample

SDSS NAME	z	$\log L5100$ erg s^{-1}	$FWHM(\mathrm{H}\beta^{\mathrm{b}})$ [a] km s^{-1}	$\log F(\mathrm{H}\beta^{\mathrm{b}})$ [b] ergs s^{-1} cm^{-2}	$\log F(\mathrm{H}\beta^{\mathrm{n}})$ [c] ergs s^{-1} cm^{-2}	FWHM([O III]) km s^{-1}	$\log F([\mathrm{O\,III}])$ ergs s^{-1} cm^{-2}	$\log F(\mathrm{Optical Fe\,II})$ ergs s^{-1} cm^{-2}	$\log M_{\mathrm{BH}}$ [d] $M_{\odot}$	L/L_{Edd}
J010352.46+003739.7	0.705	44.97	4964	-13.57	-15.54	-13.91	2913	-13.66	8.63	0.15
J014534.36+143136.9	0.636	44.27	7005	-14.37	-15.81	-15.03	803	-14.60	8.45	0.05
J023102.49-083141.2	0.587	44.18	3812	-14.23	-16.36	-14.78	1058	-14.16	8.11	0.08
J023153.64-093333.6	0.555	44.13	5557	-14.27	-16.08	-15.23	707	-14.50	8.27	0.05
J024220.10-085332.7	0.800	44.43	5939	-14.08	-15.37	-14.40	354	-14.50	8.45	0.07
J025026.66+000903.3	0.597	44.45	8448	-14.28	-16.15	-14.53	521	-14.58	8.62	0.05
J033438.28-071149.0	0.635	44.92	4620	-13.53		-14.18	527	-13.65	8.58	0.16
J080248.19+551328.8	0.664	44.75	2264	-14.09	-14.98	-14.34	782	-13.84	8.15	0.28
J080934.64+254837.9	0.545	44.54	8778	-13.88	-15.38	-14.62	719	-14.20	8.69	0.05
J081655.34+074311.5	0.645	44.37	3964	-14.19	-16.07	-14.56	992	-14.23	8.23	0.10
J082231.53+231152.0	0.653	44.86	9090	-13.76	-15.05	-13.81	598	-15.24	8.87	0.07
J083000.35+343238.7	0.740	44.44	2030	-14.52		-15.24	241		7.94	0.22
J083525.98+435211.3	0.568	44.77	2518	-14.20	-15.01	-14.84	747	-13.67	8.21	0.26
J083613.23+280512.1	0.743	44.33	2004	-14.37		-15.25	388	-14.54	7.88	0.20
J084716.03+373218.0	0.453	44.62	2539	-13.63	-14.88	-13.74	484	-14.21	8.14	0.22

(This table is available in its entirety in a machine-readable form in the online journal. A portion is shown here for guidance regarding its form and content.)

[a]ine widths (FWHM) of broad component of Hβ emission line.

[b]Flux of broad component of Hβ emission line.

[c]Flux of narrow component of Hβ emission line.

[d]Mass of SMBH derived by width of Hβ emission lines, and the formula we used is the equation 11 in Wang et al. (2009).

A.5. Sources with multiple-epoch spectroscopic observations in SDSS and BOSS

In our parent Mg II BAL sample, 61 sources have repeated spectroscopic observations in the SDSS Legacy programme and/or in the SDSS DR10 (SDSS-III/BOSS). The detailed information of these sources are summarized in Table 10. We find that four of them show obvious variability in the absorption profile; they are J083525.98+435211.3, J090825.06+014227.7, J114209.01+070957.7, and J14264704.7+401250.8. The most extreme variability occurs in J14264704.7+401250.8, with both its Mg II and He I* absorption lines being weakening evidently (Figure 26). The other three sources, as Figure 27 shows, the changes of their Mg II absorption line profile are evident. Such changes in the absorption may result from the nuclei continuum, the covering factor of the outflow, or the physical conditions of the outflow gas, which is interesting to investigate further.
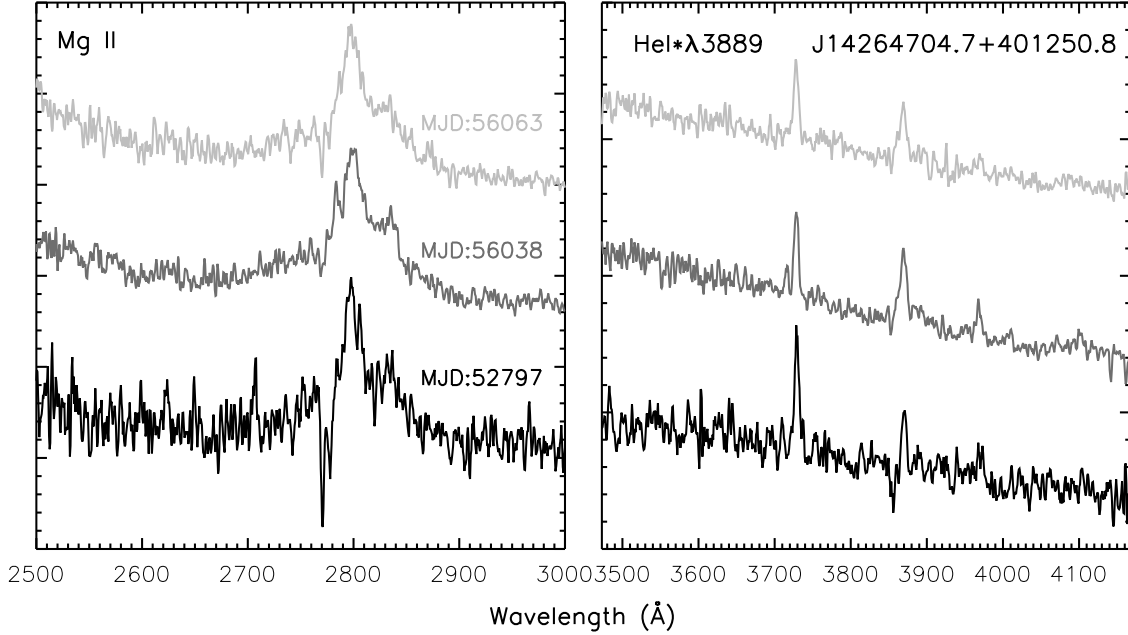

Fig. 26.— Multi-epoch spectra of SDSS J14264704.7+401250.8 in the rest frame, in the Mg II region (left) and the He I*λ3889 region. Spectra are smoothed with a two-pixel boxcar. Note that both the Mg II and He I* absorption become ever weaker with time.

Table 10.   Duplicate spectroscopic observations

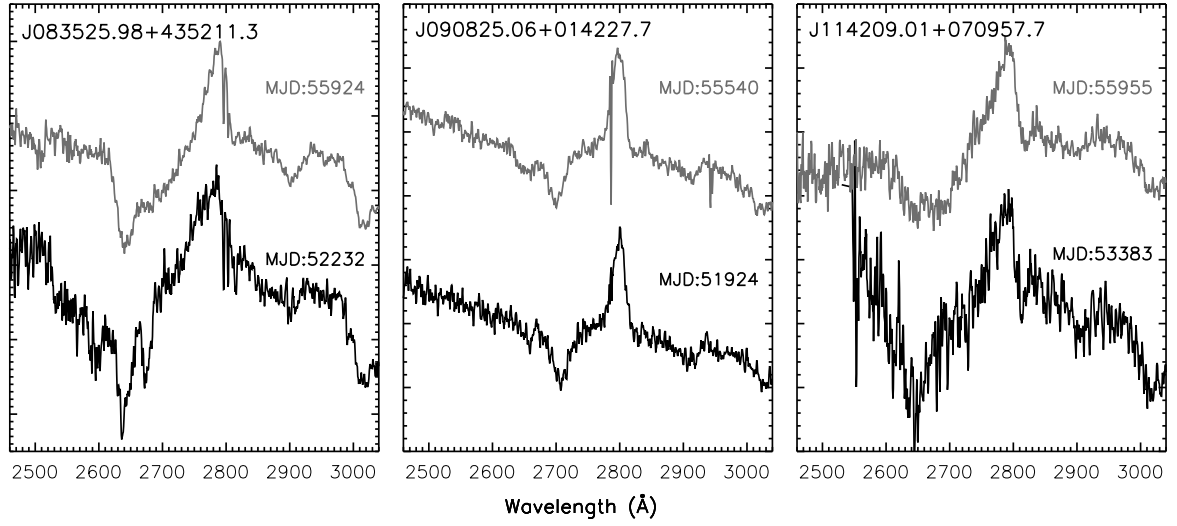| Object	z	MJD	Plate	Fiberid	Observation Date	Source	HeI* Detection[a]
J010352.46+003739.7	0.705	51816	0396	471	2000-09-29	SDSS	1
		53726	2313	384	2005-12-22	SDSS	0
		55214	3736	0522	2010-01-18	BOSS	0
		55475	4226	0600	2010-10-06	BOSS	0
J011117.34+142653.6	1.155	51821	0423	310	2000-10-04	SDSS	1
		55835	5131	0054	2011-10-01	BOSS	0
J014950.96-010314.1	1.082	51793	0402	260	2000-09-06	SDSS	1
		55447	4232	0202	2010-09-08	BOSS	0
J020105.14+000617.9	1.205	51871	0403	593	2000-11-23	SDSS	1
		52179	0701	465	2001-09-27	SDSS	1
		55201	3609	0620	2010-01-05	BOSS	1
J025026.66+000903.3	0.597	51871	0409	553	2000-11-23	SDSS	0
		52175	0708	394	2001-09-23	SDSS	0
		52177	0707	583	2001-09-25	SDSS	0
		55450	4241	0855	2010-09-11	BOSS	0
J025204.17+010710.5	1.223	51816	0410	321	2000-09-29	SDSS	0
		51877	0410	325	2000-11-29	SDSS	0
J074554.74+181817.0	1.054	52939	1582	256	2003-10-27	SDSS	1
		53437	2074	517	2005-03-08	SDSS	0
		54497	2915	543	2008-02-01	SDSS	0
		55565	4492	0798	2011-01-04	BOSS	0
J075325.52+414842.9	1.349	51882	0435	408	2000-12-04	SDSS	0
		51885	0434	011	2000-12-07	SDSS	0
J075927.12+363431.5	0.983	52238	0757	474	2001-11-25	SDSS	1
		55509	3801	0688	2010-11-09	BOSS	0
J080957.38+181804.4	0.969	53319	1923	023	2004-11-10	SDSS	1
		55585	4493	0632	2011-01-24	BOSS	0
J081312.61+432640.1	1.090	51959	0547	242	2001-02-19	SDSS	0
		52205	0546	449	2001-10-23	SDSS	0
		52207	0547	274	2001-10-25	SDSS	0
J083522.77+424258.3	0.807	52232	0762	085	2001-11-19	SDSS	1
		55924	4683	0338	2011-12-29	BOSS	0
J083525.98+435211.3	0.568	52232	0762	175	2001-11-19	SDSS	0
		55924	4683	0683	2011-12-29	BOSS	0
J090154.96+380534.4	1.038	52705	0936	498	2003-03-07	SDSS	0
		55973	4608	0844	2012-02-16	BOSS	0
J090825.06+014227.7	1.002	51924	0471	499	2001-01-15	SDSS	0

Fig. 27.— SDSS spectra of the three sources displaying significant changes in their Mg II absorption line.

Table 10—Continued

Object	z	MJD	Plate	Fiberid	Observation Date	Source	HeI* Detection[a]
		55540	3819	0234	2010-12-10	BOSS	0
J092035.59+524006.2	0.793	51999	0553	612	2001-03-31	SDSS	0
		52252	0767	321	2001-12-09	SDSS	0
J092157.62+103539.0	0.548	53050	1740	170	2004-02-15	SDSS	1
		55926	5306	0196	2011-12-31	BOSS	0
J094225.42+565613.0	0.833	51991	0556	545	2001-03-23	SDSS	0
		52253	0557	359	2001-12-10	SDSS	0
J094443.13+062507.4	0.695	52710	0993	535	2003-03-12	SDSS	1
		55926	4873	0470	2011-12-31	BOSS	0
J095057.56+542919.4	1.194	52282	0769	507	2002-01-08	SDSS	0
		54530	0769	504	2008-03-05	SDSS	0
J095914.91+131639.5	1.009	53055	1744	362	2004-02-20	SDSS	0
		55982	5328	0528	2012-02-25	BOSS	0
J102943.75+370127.2	1.344	53415	1957	601	2005-02-14	SDSS	1
		53432	1973	235	2005-03-03	SDSS	0
J103255.37+083503.2	0.894	52734	1240	316	2003-04-05	SDSS	1
		55924	5344	0796	2011-12-29	BOSS	0
J104459.60+365605.1	0.701	53463	2090	329	2005-04-03	SDSS	1
		55615	4635	0704	2011-02-23	BOSS	0
J104845.83+353110.7	1.011	53463	2090	131	2005-04-03	SDSS	1
		55615	4635	0136	2011-02-23	BOSS	0
J105259.99+065358.0	0.724	52670	1001	080	2003-01-31	SDSS	0
		55685	4854	0598	2011-05-04	BOSS	1
J111628.00+434505.8	0.801	53061	1364	095	2004-02-26	SDSS	1
		56013	4686	0594	2012-03-27	BOSS	0
J112349.16+135220.6	0.928	53383	1753	093	2005-01-13	SDSS	0
		56003	5370	0688	2012-03-17	BOSS	1
J112828.31+011337.9	0.893	51614	0281	523	2000-03-11	SDSS	0
		51992	0512	123	2001-03-24	SDSS	0
		55630	4730	0172	2011-03-10	BOSS	0
J112901.71+050617.0	1.282	52376	0836	626	2002-04-12	SDSS	0
		52642	0837	400	2003-01-03	SDSS	0
J113349.81+361027.3	1.158	53468	2113	608	2005-04-08	SDSS	0
		55618	4615	0762	2011-02-26	BOSS	0
J114111.61-014306.6	1.266	52282	0328	417	2002-01-08	SDSS	1
		55207	3775	0820	2010-01-11	BOSS	0
J114209.01+070957.7	0.497	53383	1621	306	2005-01-13	SDSS	0

Table 10—Continued

Object	z	MJD	Plate	Fiberid	Observation Date	Source	HeI* Detection[a]
		55955	4848	0546	2012-01-29	BOSS	0
J114915.30+393325.4	0.630	53386	1970	137	2005-01-16	SDSS	0
		55659	4654	0080	2011-04-08	BOSS	1
J115852.87-004301.9	0.983	51663	0285	184	2000-04-29	SDSS	0
		51930	0285	189	2001-01-21	SDSS	0
J120049.55+632211.8	0.887	52320	0777	609	2002-02-15	SDSS	0
		52337	0778	377	2002-03-04	SDSS	0
J120146.46+630034.4	0.659	52337	0778	439	2002-03-04	SDSS	0
		54525	0778	477	2008-02-29	SDSS	0
J122614.97+120925.4	0.871	53120	1614	145	2004-04-25	SDSS	1
		55979	5403	0524	2012-02-22	BOSS	0
J125507.12+634423.8	1.067	52316	0601	043	2002-02-11	SDSS	0
		52320	0782	445	2002-02-15	SDSS	0
J131323.25+151309.6	1.262	53089	1772	627	2004-03-25	SDSS	1
		56033	5424	0206	2012-04-16	BOSS	0
J131823.73+123812.5	0.589	53142	1697	600	2004-05-17	SDSS	0
		56001	5427	0574	2012-03-15	BOSS	0
J132401.53+032020.6	0.926	52312	0526	609	2002-02-07	SDSS	0
		55633	4761	0136	2011-03-13	BOSS	0
J133603.65+511733.6	1.327	53433	1668	593	2005-03-04	SDSS	0
		53433	1669	339	2005-03-04	SDSS	0
J140025.53-012957.0	0.584	52443	0915	380	2002-06-18	SDSS	0
		55363	4038	0558	2010-06-16	BOSS	0
J142010.28+604722.3	1.345	52365	0606	110	2002-04-01	SDSS	0
		52368	0607	293	2002-04-04	SDSS	0
J142647.47+401250.8	0.749	52797	1349	0348	2003-06-07	SDSS	1
		56038	5171	0532	2012-04-21	BOSS	0
		56063	5170	0928	2012-05-16	BOSS	0
J142927.28+523849.5	0.595	52764	1326	057	2003-05-05	SDSS	1
		52781	1327	343	2003-05-22	SDSS	0
J143144.91+391910.2	1.091	52797	1349	257	2003-06-07	SDSS	1
		56038	5171	0340	2012-04-21	BOSS	0
J143826.73+642859.8	1.222	51988	0499	623	2001-03-20	SDSS	0
		54533	2947	557	2008-03-08	SDSS	0
J144436.58+425508.6	1.101	52734	1289	087	2003-04-05	SDSS	0
		53112	1396	612	2004-04-17	SDSS	0
J145333.01+002943.6	1.291	51666	0309	424	2000-05-02	SDSS	0

A.6.   He I*λ3889 BAL quasars with supportive NIR and UV spectra

We have performed followup near infrared (NIR) spectroscopic observations for sources the He I*λ3889 BAL sample to check their expected He I*λ10830 BAL features. The NIR observations were made by the Palomar P200 telescope with the Triple-Spec spectroscopy on 2012 April 15–16th, 2013 February 22–23th, and 2014 January 17–19th. All spectra were taken in an A-B-B-A dithering mode, in the primary configuration of the instrument (a spectral resolution of R $\sim$ 3500 through a 1″ slit). The telluric standard stars were taken quasi-simultaneously. The data were reduced with the IDL program SpexTool (Cushing et al. 2004). The flux calibration and telluric correction were performed with the IDL program that adopts the methods as described in Vacca et al. (2003).

On the other hand, some sources have UV spectra in the HST or IUE archives, where C IV BAL is present, confirming our detection of their He I*λ3889 absorption line.

A.6.1.   *Four sources in the He I* λ3889 BAL sample*

J074554.74+181817.0

J0745+1818 is a FeLoBAL quasar at $z = 1.054$, which is first identified by G09. In its rest frame UV spectrum, broad Mg II and Fe II absorption lines are seen. The Mg II absorption trough, spans from -613 km s^{-1}to -3971 km s^{-1}, with a weighted average velocity of -1887 km s^{-1}. The associated He I*$\lambda\lambda$3889, 3189 absorption lines are first identified in this work, the detections of which are also confirmed by the NIR observation using TripleSpec on Palomar P200 telescope. This NIR observation is performed on 2014 January 19th, and four 240s exposures were taken in A-B-B-A dithering mode. One telluric standard stars was taken quasi-simultaneously.

J080248.18+551328.9 (Ji et al. 2014)

J0802+5513 is identified as a LoBAL quasar by G09 according to detection of Mg II absorption lines. Plenty of absorption lines are detected, including He I*, Fe II* and Ni II* that arise from metastable or excited levels, as well as resonant lines in Mg II, Fe II, Mn II, Ca II and Mg I. All these absorption lines are associated with the same profile of $\sim$ 2000 km s^{-1}width centered at a common redshift of the quasar emission lines. Ji et al. (2014) detailedly studied this target and determined that the absorber has a density of $n_e \sim 10^5$ cm^{-3} and a column density of $N_H \sim 10^{21} - 10^{21.5}$cm^{-2}, and is located at $\sim 100 - 250$ pc from the central SMBH. J0802+5513 is also included in our He I*λ3889 absorption line sample.

J084044.41+363327.8

Table 10—Continued

Object	z	MJD	Plate	Fiberid	Observation Date	Source	HeI* Detection[a]
		51994	0309	433	2001-03-26	SDSS	0
		52029	0538	202	2001-04-30	SDSS	0
J150847.41+340437.7	0.788	53108	1385	173	2004-04-13	SDSS	1
		55691	4720	0591	2011-05-10	BOSS	0
J152438.79+415543.0	1.230	53433	1678	106	2005-03-04	SDSS	0
		56067	5164	0894	2012-05-20	BOSS	0
J163656.84+364340.4	0.852	52782	1174	337	2003-05-23	SDSS	1
		56048	5195	0930	2012-05-01	BOSS	0
J170341.82+383944.7	0.554	52071	0632	632	2001-06-11	SDSS	1
		54232	2192	058	2007-05-12	SDSS	0
J212017.00+004841.7	1.288	52523	0987	408	2002-09-06	SDSS	0
		55469	4192	0874	2010-09-30	BOSS	0
		55825	5142	0341	2011-09-21	BOSS	0
J220931.92+125814.5	0.814	52519	0735	501	2002-09-02	SDSS	1
		55749	5041	0390	2011-07-07	BOSS	1
J223424.10+005227.1	0.884	52143	0376	615	2001-08-22	SDSS	0
		52201	0674	370	2001-10-19	SDSS	0
J224028.14-003813.1	0.658	53261	1901	298	2004-09-13	SDSS	1
		55470	4204	0232	2010-10-01	BOSS	0
J232550.73-002200.4	1.011	51818	0383	142	2000-10-01	SDSS	1
		52199	0681	269	2001-10-17	SDSS	0
J233635.75-010733.7	1.303	51821	0384	011	2000-10-04	SDSS	0
		52525	0682	202	2002-09-08	SDSS	0

[a]Detection of He I*λ3889 absorption line. '1' denotes a spectrum with He I*λ3889 absorption line. '0' denotes a spectrum failed to detect He I*λ3889 absorption line.

This FBQS quasar was first reported by Becker et al. (1997) as a radio-moderate LoBAL. A spectropolarimetry study by Brotherton et al. (1997) reveals that it is a highly polarized BAL quasar. The spectrum of this quasar in the rest frame wavelength range is dominated by absorption lines of Fe II, and it also contains lines of other singly ionized iron group elements, Si II, Mg II, Al III, and Fe III. According to de Kool et al. (2002), the outflow gas of this quasar covers a range of velocity from -700 km s^{-1} to -3500 km s^{-1}, with two component centered at -900 and -2800 km/s. The low-velocity gas is determined as a low-density gas ($n_e < 500$ cm^{-3}) and is ~ 230 pc away from the AGN nuclei. The high-velocity gas shows a high density and ~ 1 pc away from the AGN nuclei. This distance is determined by the absence of detectable He I*λ2830 absorption line. In our sample, this quasar is classified as a He I*λ3889 BAL, which is also confirmed by the NIR observation for He I*λ10830 absorption line. The total column density and location of the absorption gas can be better determined via the He I* lines join with other lines. The NIR observation is carried out on 2014-01-17 using TripleSpec at P200 telescope, and 4×180 s exposures were taken in A-B-B-A mode.

J120924.07+103612.0

LBQS 1206+1052 is reported by Ji et al. (2012) as a rare Balmer broad absorption line quasar, and it also displays He I* Mg II absorption lines in SDSS spectrum taken on March 24, 2003. Joshi et al. (2011) reported the significant variations over their observational run of ~ 4 h. We performed a series of follow up observations for this quasar. On May 7th, 2012, LBQS 1206+1052 was taken by Yunnan Faint Object Spectrograph and Camera (YFOSC) mounted on Lijiang GMG 2.4m telescope in a rest wavelength range of 2500–5400Å. Compare with the SDSS spectrum, the absorption troughs fade during nine years. On April 23, 2014, this quasar was taken by Double Spectrograph (DBSP) at P200 telescope in a rest wavelength range of 2250–4180 and 5620–7450 Å. The states of the absorption lines show little variability relative to the YFOSC observation. A NIR observation was carried out on February 22, 2013 to obtain He I*λ10830 absorption line profile, which show a narrow faded He I*λ10830 absorption trough. This target is detailed studied in Sun et al. (2015, in preparation).

A.6.2. Two example C IV BAL quasars with evident He Iλ3889 absorption yet weak Mg II absorption*

J035230.55-071102.3

J0352-0711 is known as 3C094, which is a steep-spectrum radio-loud quasar. The FUV spectrum for this quasar, which was obtained with Faint Object Spectrograph (FOS) on board the HST by Tytler & Davis (1995) using G270H grating, shows a broad C IV absorption line. We detected
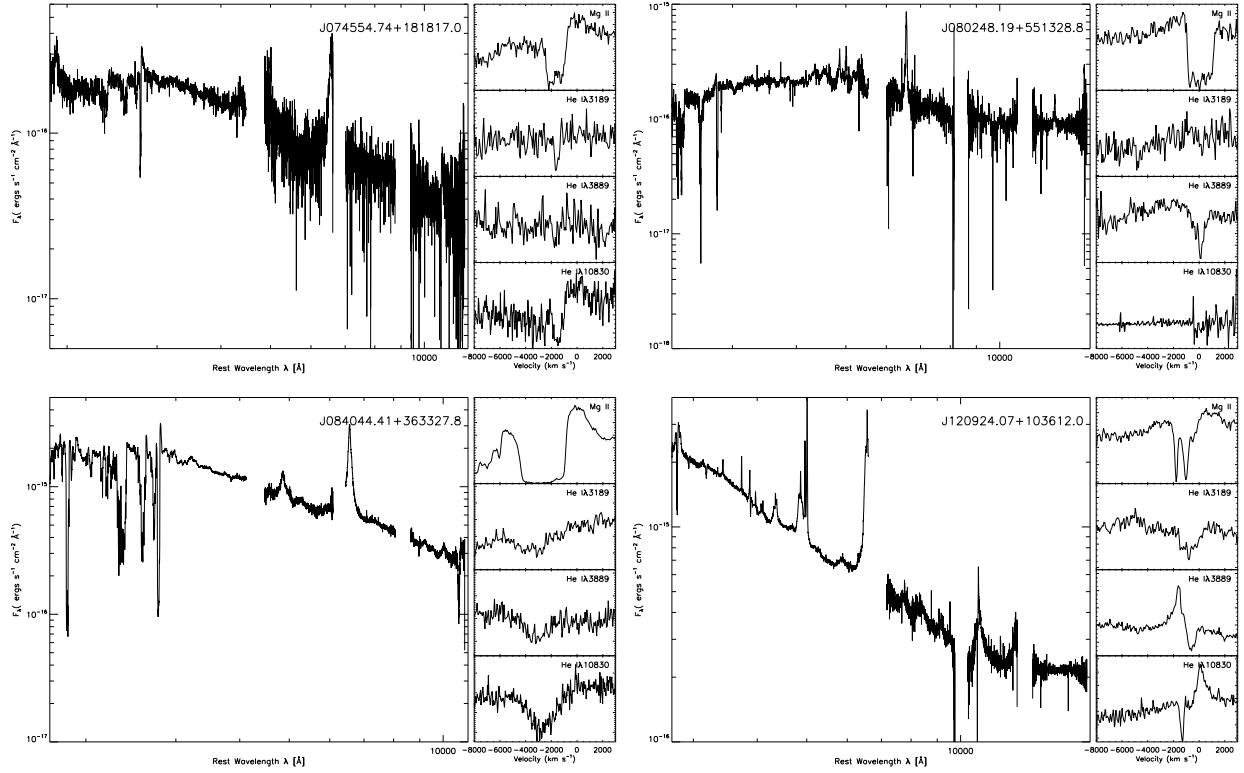
Fig. 28.— Sources in our main sample that have NIR spectra. (continue)

the He I*λ3889 absorption line in SDSS spectrum. However, this quasar is not in our parent Mg II BAL sample because of the weakness of Mg II absorption line. We observe this quasar using TripleSpec at P200 telescope on February 23, 2012, and 4×180 s exposures were taken in A-B-B-A mode. The significant He I*λ10830 absorption trough are seen in the NIR spectrum.

J141348.33+440014.0

PG 1411+442 is one of nearest HiBAL quasars (z_{em} = 0.0896). It shows broad Lyα, N V, Si IV, C IV absorption features in UV spectrum (Malkan et al. 1987; Wang et al. 1999). It is also known as a X-ray quiet quasar due to substantial intrinsic absorption with $N_H > 10^{23}$ cm^{-2} (e.g., Brinkmann et al. 1999). PG 1411+442 is also a luminous infrared quasar with a total infrared luminosity of logL_{IR}=11.6 $L_\odot$(Weedman et al. 2012). On January 17, 2014, this quasar was observed by TripleSpec at P200 telescope, and 4×180 s exposures were taken in A-B-B-A mode. He I*λ10830 absorption trough are seen in the NIR spectrum, which share the common blueshift with the C IV absorption line. On April 23, 2014, this quasar was observed by DBSP at P200 telescope in a rest wavelength range of 3000–5400 and 7200–9500 Å, and 2 × 300s exposure were taken. He I*λ3889 absorption trough is detected in the NUV spectrum.
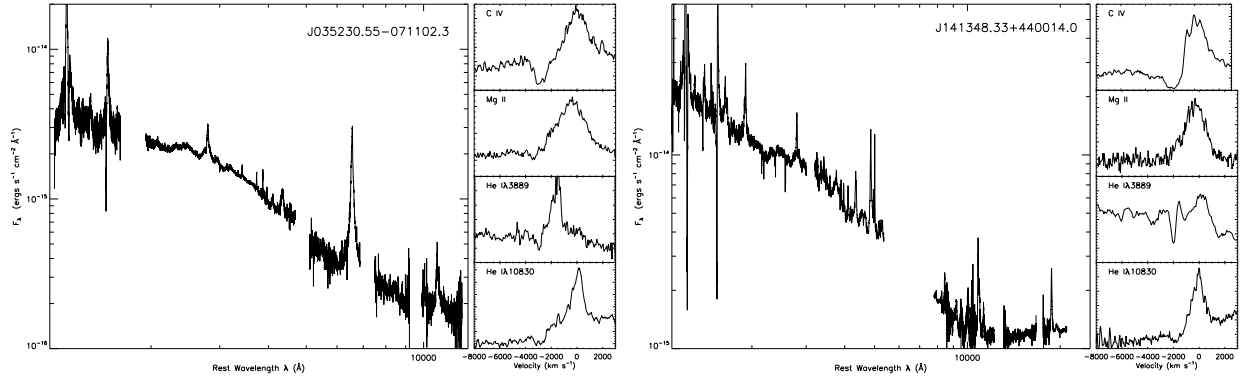
Fig. 29.— C IV BALs that have obvious He I* absorption line and have weak Mg II absorption line

A.6.3. Six sources in the low-z BAL sample identified with He I*λ3889

J075217.84+193542.2

J075217.84+193542.2 is a Seyfert I galaxy at $z = 0.117$, which is the most nearest targets in our low-z He I* sample. We observed this target using TripeSpec at P200 telescope on February 23th, 2013, and 4×120s exposures were taken in A-B-B-A mode. The He I*λ10830 absorption line is detected in the NIR spectrum.

J093653.81+533127.0

J0936+5331 is a Seyfert 1 galaxy at $z = 0.227$. It is a low-z C IV HiBAL according to the detection of C IV absorption trough and absence of Mg II absorption feature in UV observations by HST. FUV and NUV spectrum for this quasar were obtained with Cosmic Origins Spectrograph (COS) G140L grating and Space Telescope Imaging Spectrograph (STIS) G430L grating on board the HST respectively by Lusso et al. (2014). We detected the He I*λλ3189, 3889 lines in its SDSS spectrum, which have the common blueshift with that of C IV. The NIR observation was carried out using TripleSpec at P200 telescope on February 23th, 2013, and 4×180s exposures were taken in A-B-B-A mode. The expected He I*λ10830 absorption line are seen in the NIR spectrum.

J130534.49+181932.8

J130534.49+181932.8 is a low-z ($z = 0.118$) quasar. We detect the He I*λ3889 absorption line in its SDSS spectrum. This source is also observed by COS G140L grating and STIS G430L grating on board the HST telescope in 2011 by Lusso et al. (2014). C IV and Mg II absorption lines are detected in the FUV and NUV spectrum, and they have common blueshift with the He I*λ3889 absorption line.

J153539.25+564406.5

J1535+5644 is a Seyfert I galaxy at $z = 0.208$. He I*$\lambda\lambda 3189, 3889$ and rare Hα absorption line are detected in the SDSS spectrum. The NIR observation was carried out using TripleSpec at P200 telescope on Feburay 23th, 2013, and 4×180s exposures were taken in A-B-B-A mode. The expected He I*$\lambda 10830$ absorption line are seen in the NIR spectrum.

J163459.82+204936.0

J1634+2049 is a nearby ($z = 0.1295$) ultra-luminous infrared galaxy with a total infrared luminosity of $\sim 1 \times 10^{12} L_{\odot}$ according to the photometry of IRAS. The star forming rates (SFR) gets from L_{IR} is $\sim 120 M_{\odot}$, but the [OII] shows the SFR is normal. This quasar shows a red broad band spectra energy distribution (SED) relative to that of composite spectra of quasars. The reddening calculated from decrement for narrow lines is much lager than that for broad lines, with $E(B-V)_{narrow} = 1.13$ and $E(B-V)_{broad} = 0.75$. These narrow lines are mainly from HII region according to the BPT diagram. These properties suggest this quasar is an obscured starburst quasar. He I*$\lambda 3889$ is detected in the SDSS spectrum, and interestingly broad Na D absorption line is also detected, which indicate a large column density of the outflow gas. The NIR observation is carried out on April 15, 2012 using TripleSpec at P200 telescope, and 4×120s exposures were taken in A-B-B-A dithering mode. The expected He I*$\lambda 10830$ absorption line is seen in the NIR spectrum, and strong Pα, Pγ emission lines are also detected. We will detailedly investigate this quasar in later paper (Liu et al. 2015, in preparation).

J222024.58+010931.2

J2220+0109 is a type I quasar in the SDSS Stripe 82, and it shows significant variability (Meusinger et al. 2011). We detected deep and broad He I*$\lambda\lambda 3189, 3889$, and weak Balmer absorption lines in the SDSS spectrum. The NIR observation was carried out using TripleSpec at P200 telescope on October 21th, 2011, and 4×300s exposures were taken in A-B-B-A mode. The expected He I*$\lambda 10830$ absorption line are seen in the NIR spectrum.
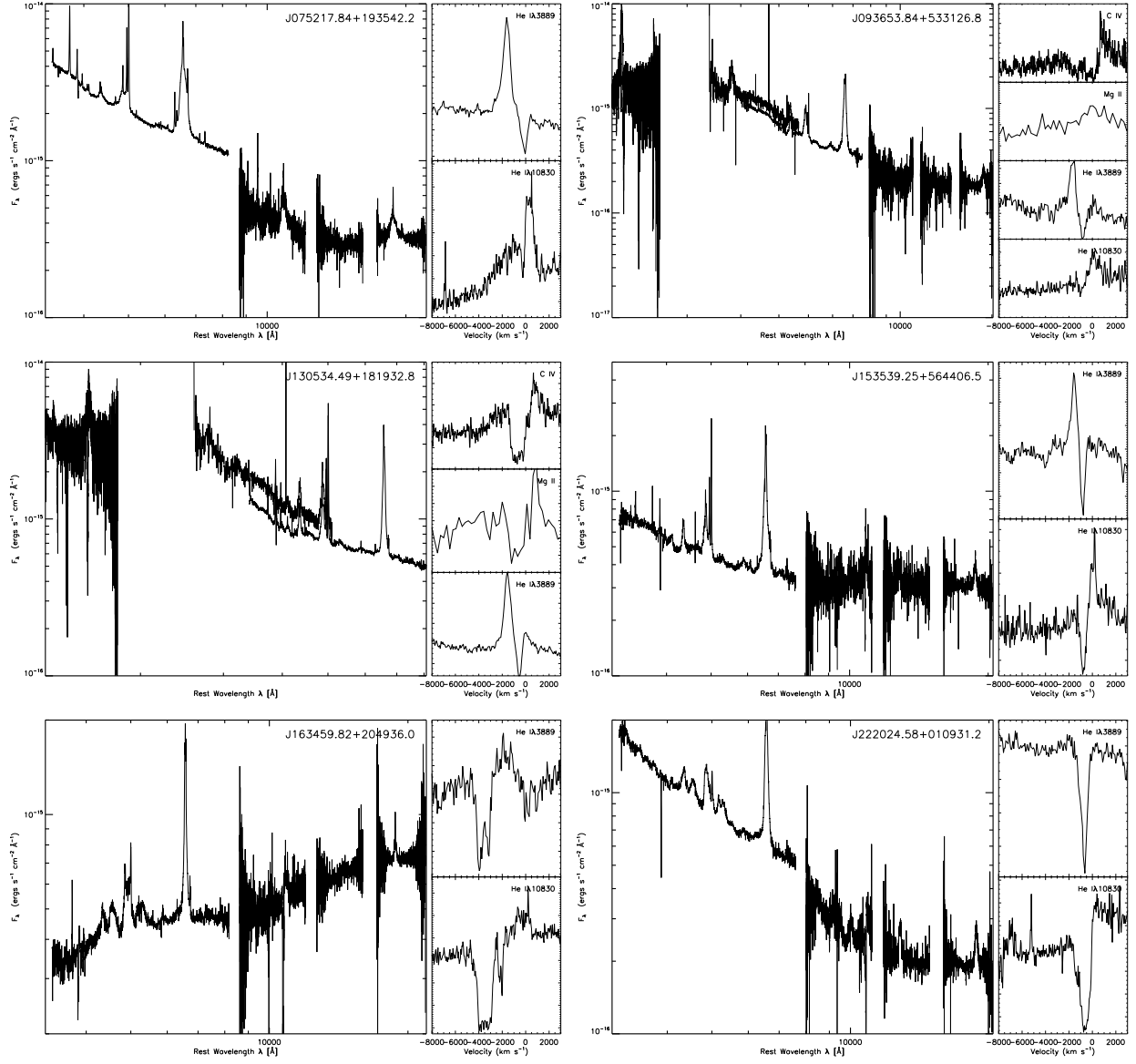
Fig. 30.— Low-z He I* BALs that have UV or NIR spectra.

A.7. Demonstration of fitting the He I*λ3889 BAL quasars
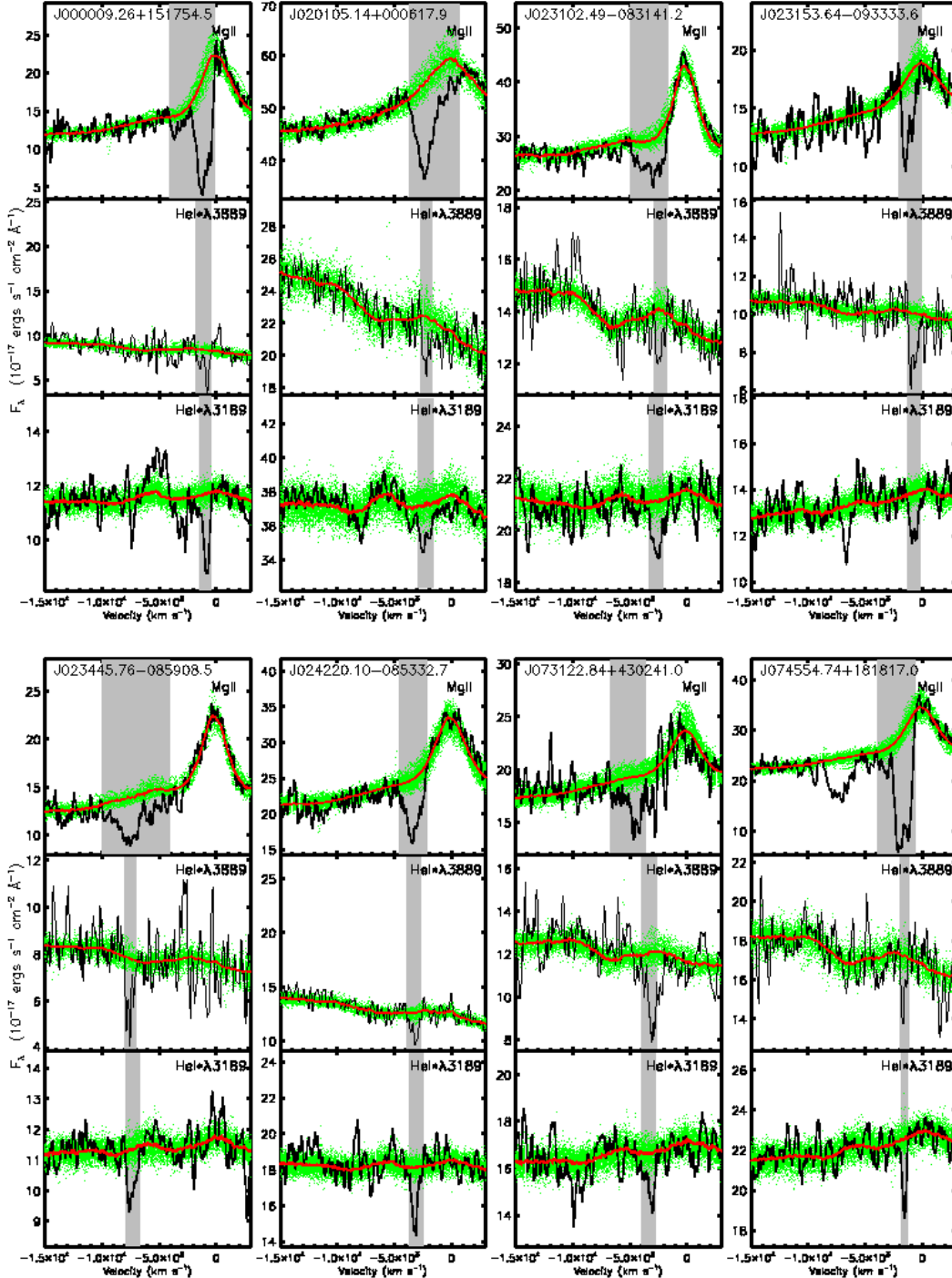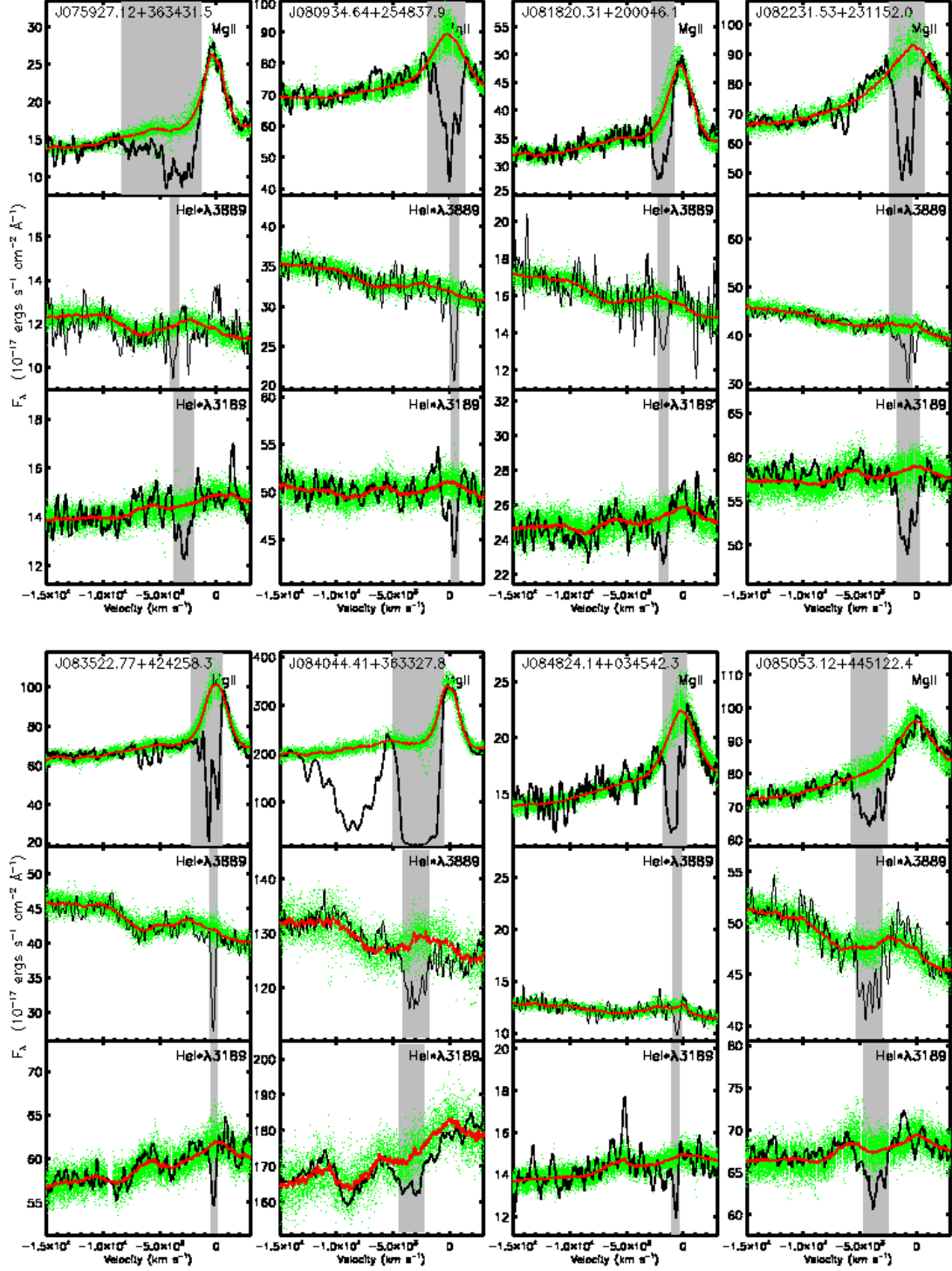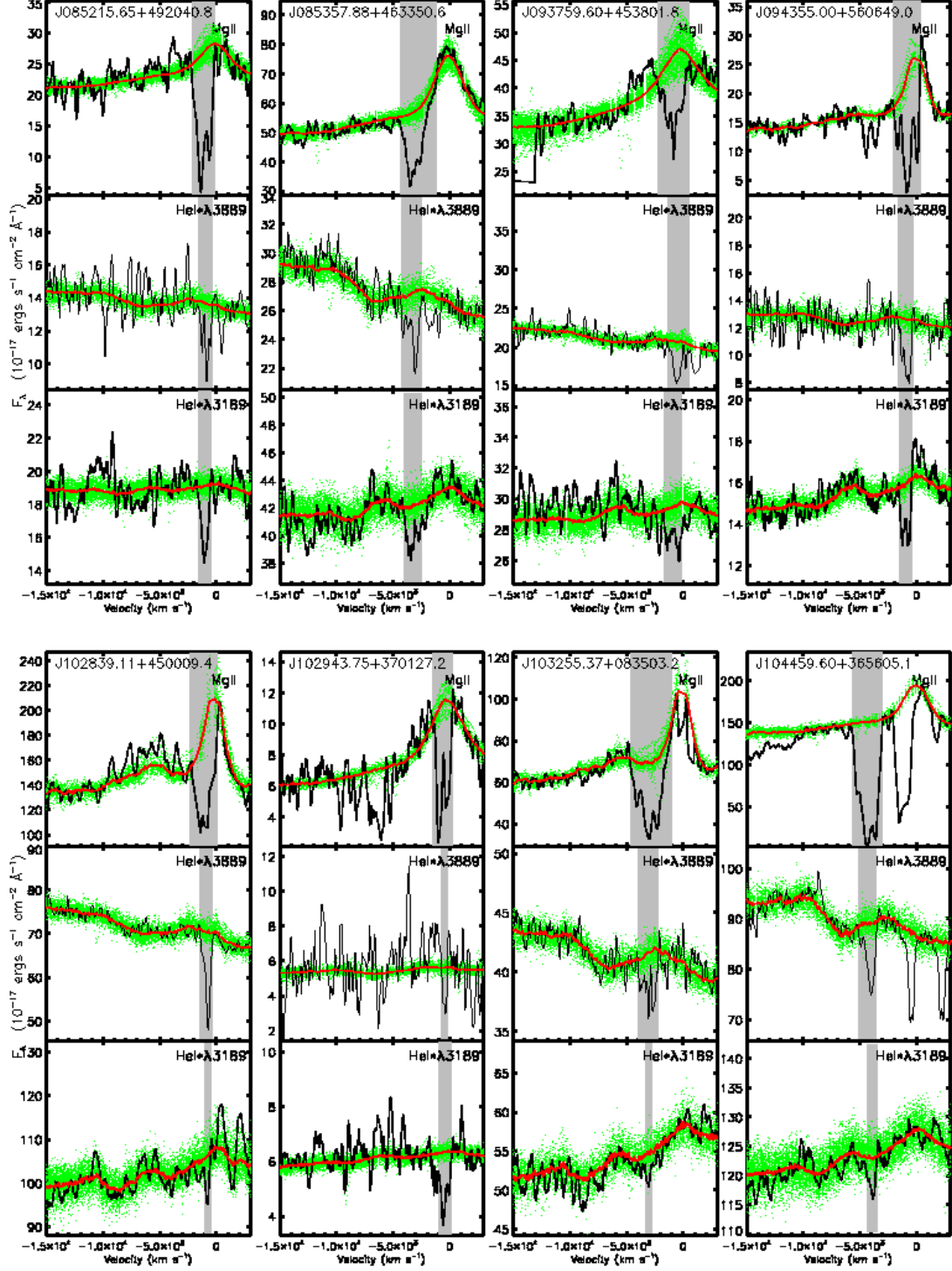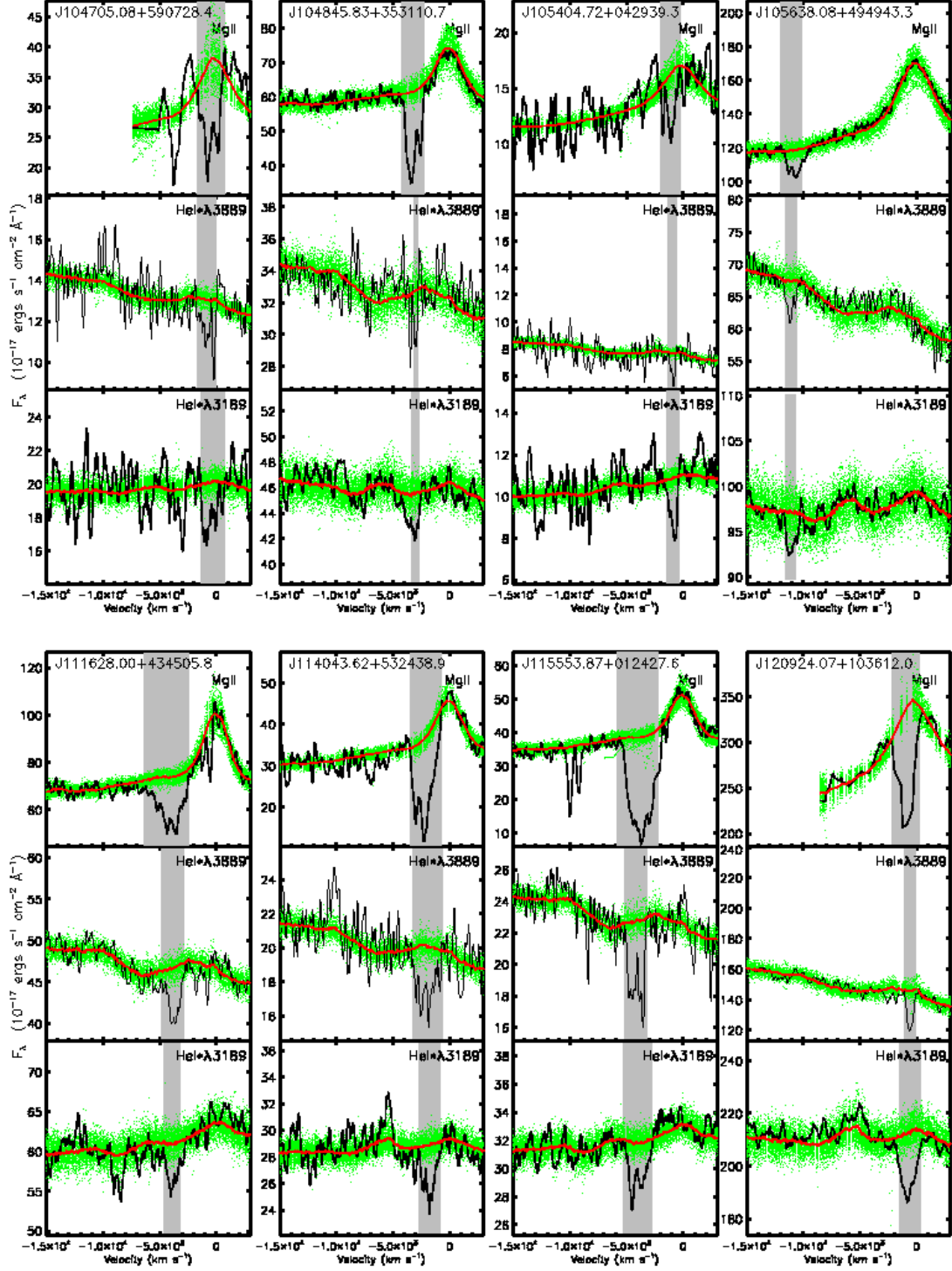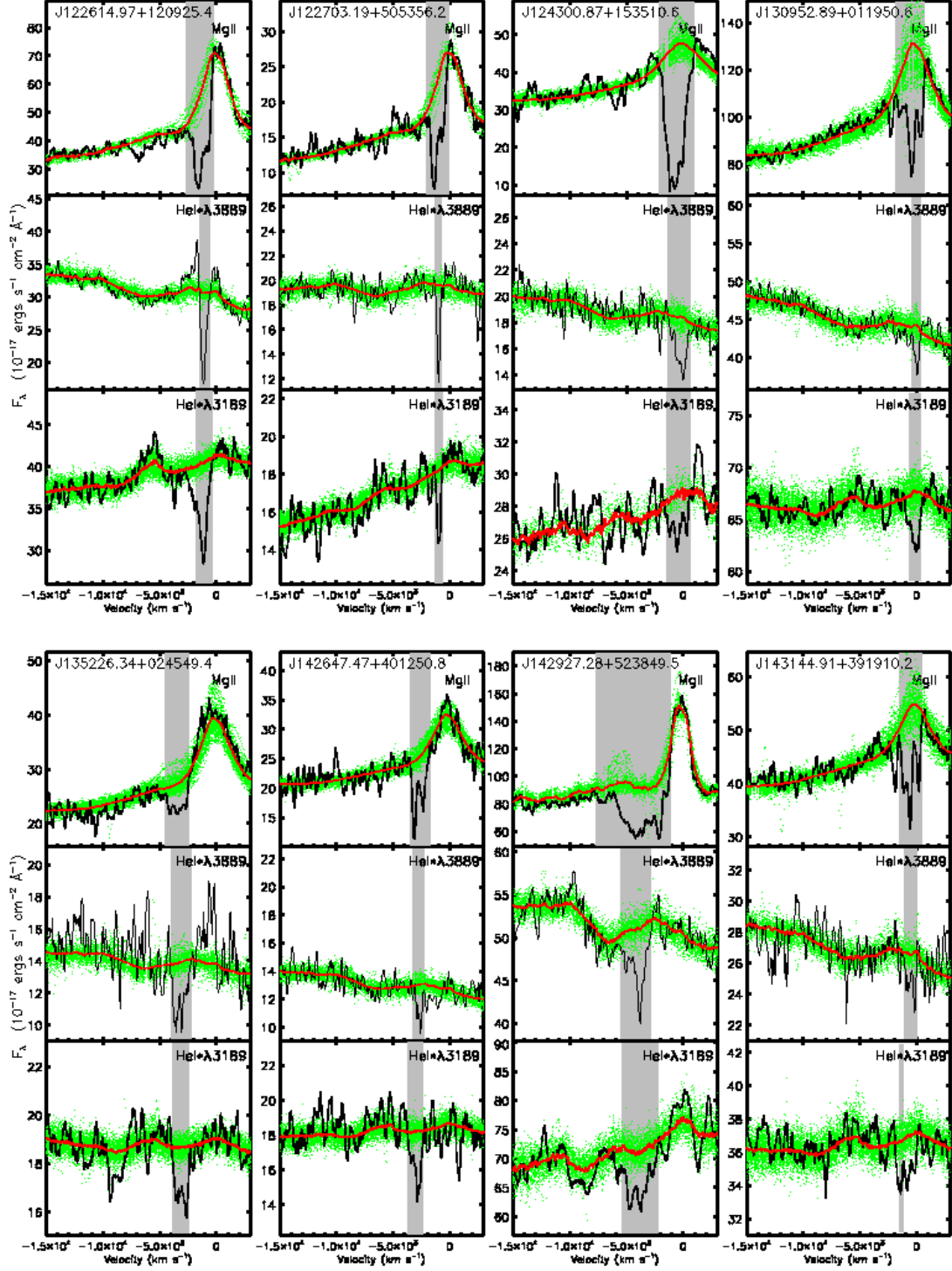
A.7.1. Sources also with He I*λ3189 absorption line

Fig. 31.— Demonstration of the spectral fitting for all the 52 sources that have Mg II, He I*λ3889 and He I*λ3189 absorption troughs. The acceptable fittings of the unabsorbed spectrum of an object are denoted as green dotted lines, and their mean spectrum denoted as a red solid line.
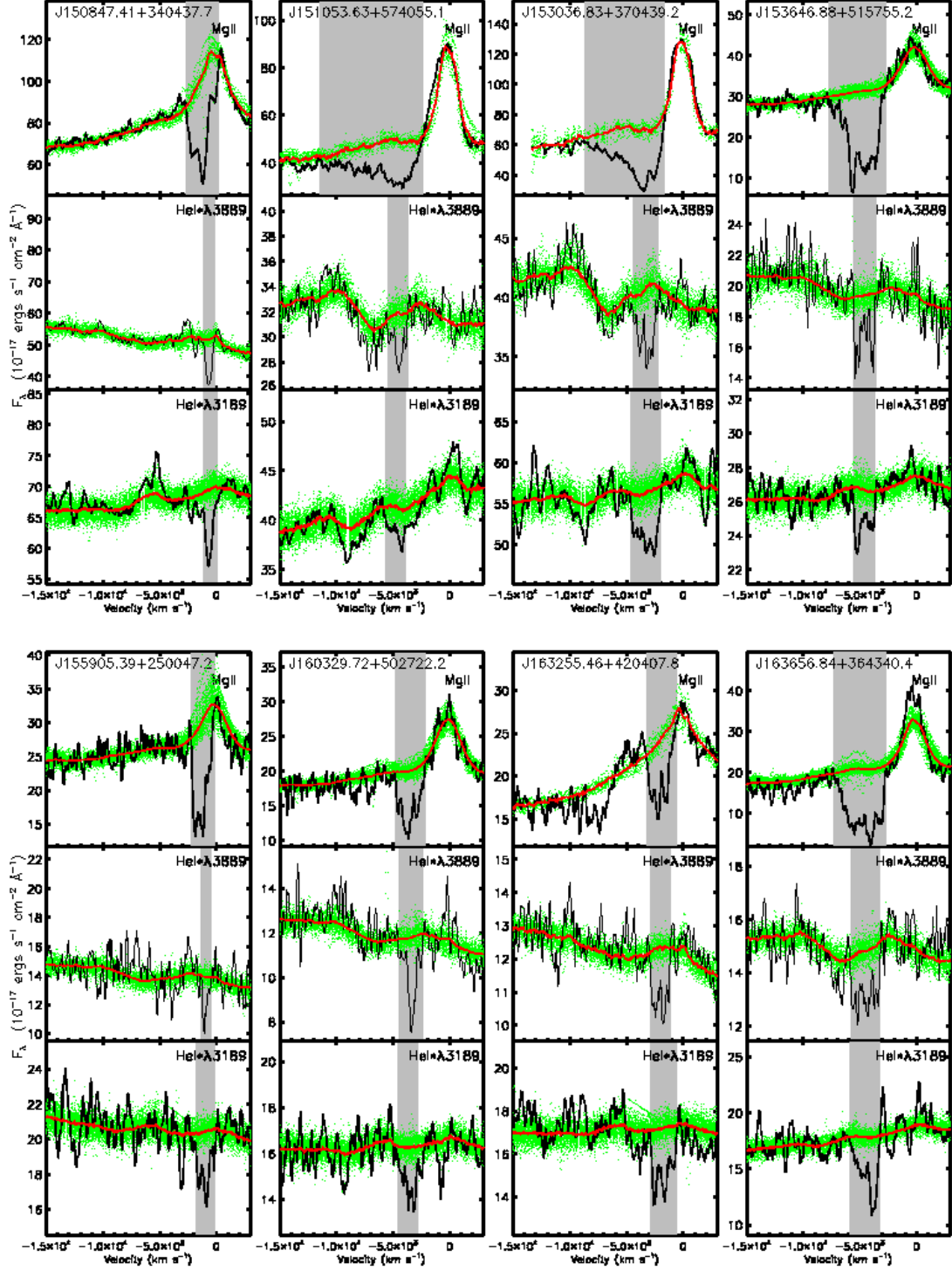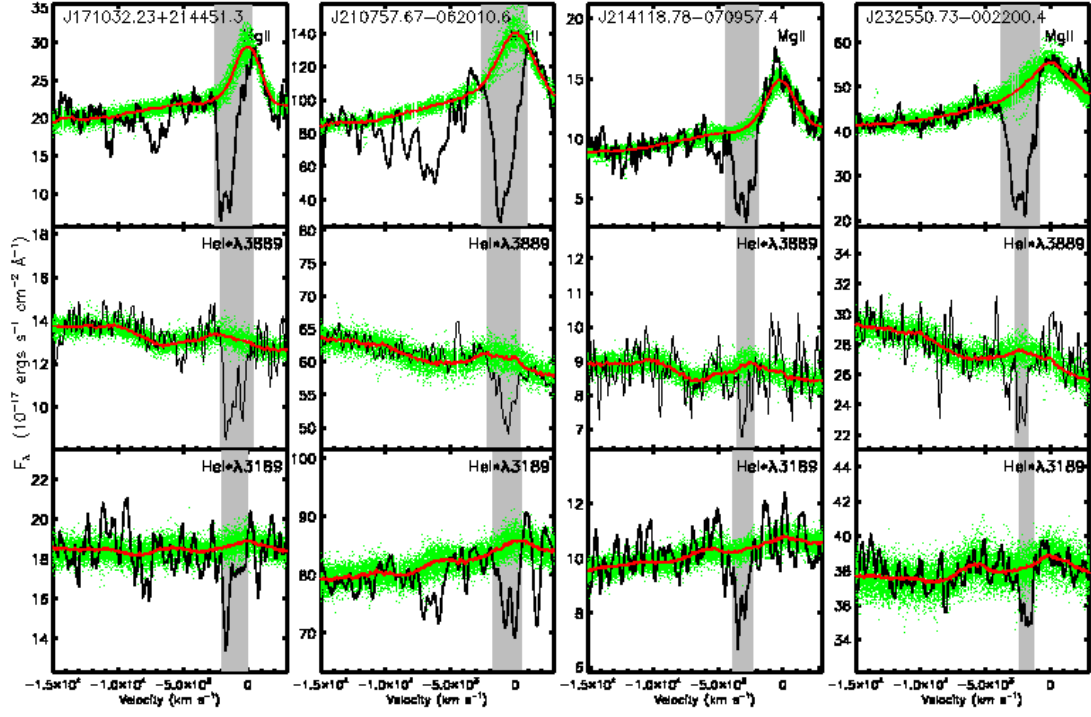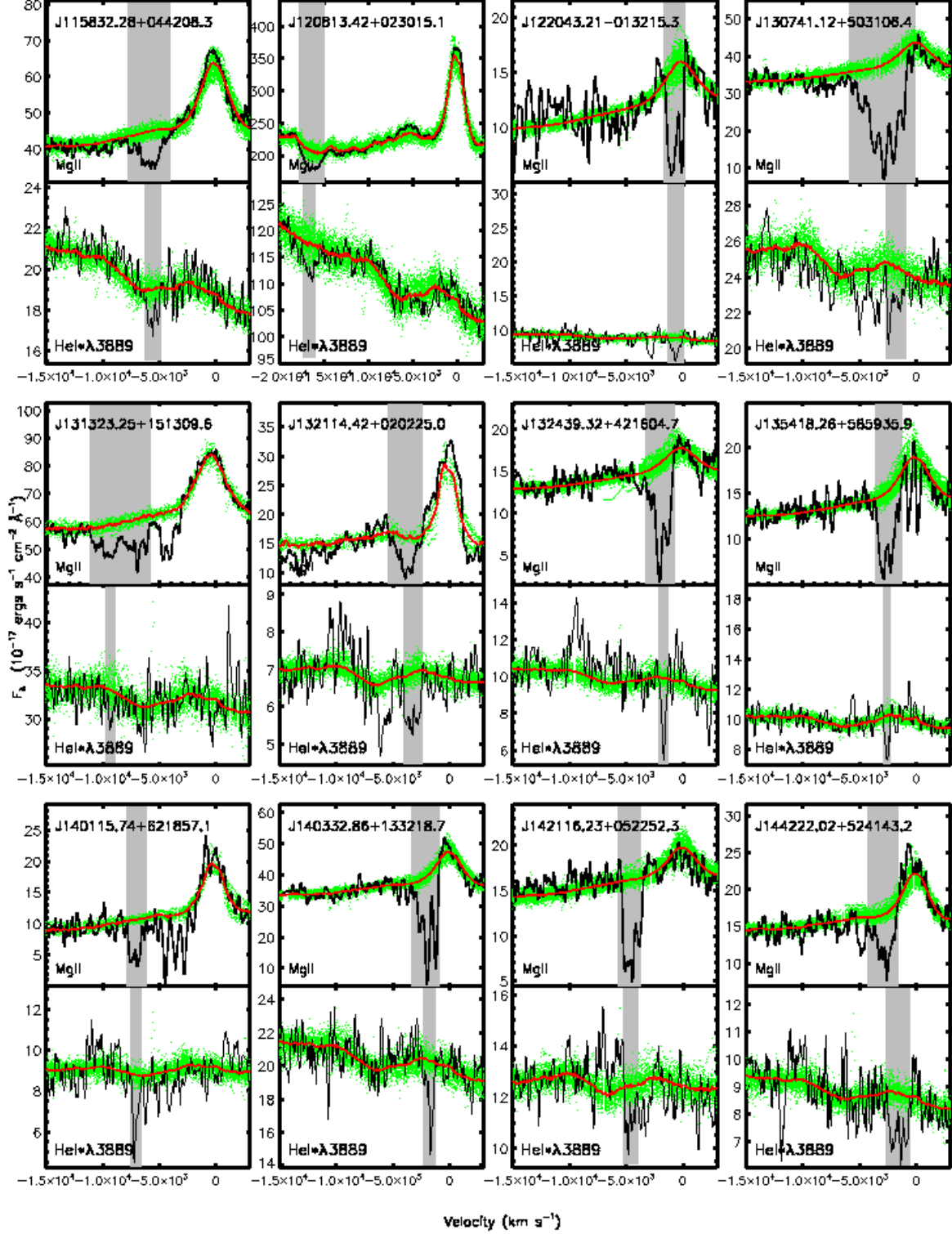
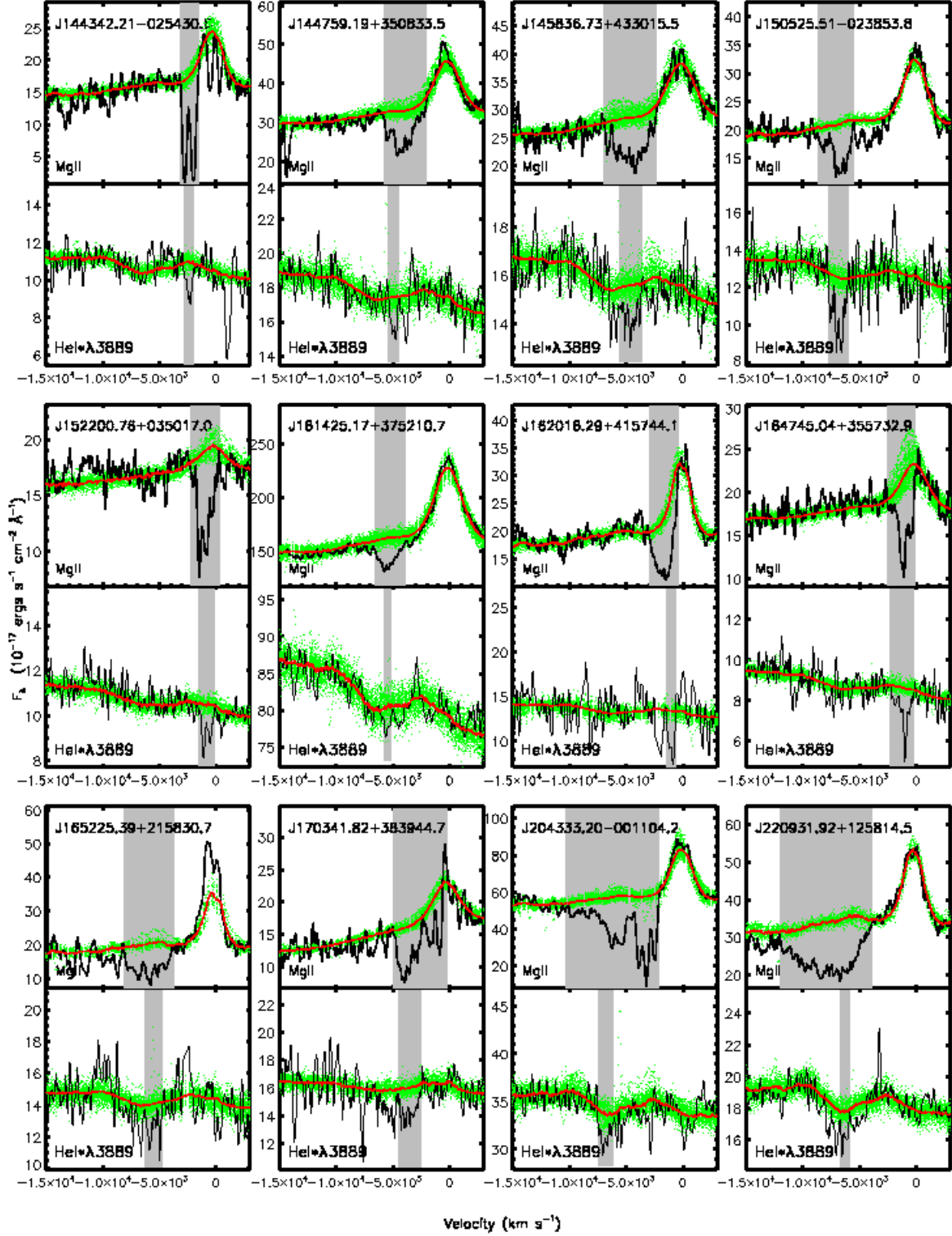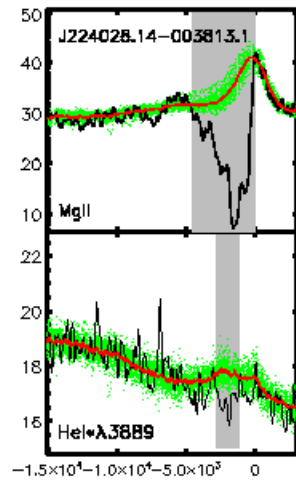*A.7.2.   Sources without He I*λ3189 absorption line*

– 88 –
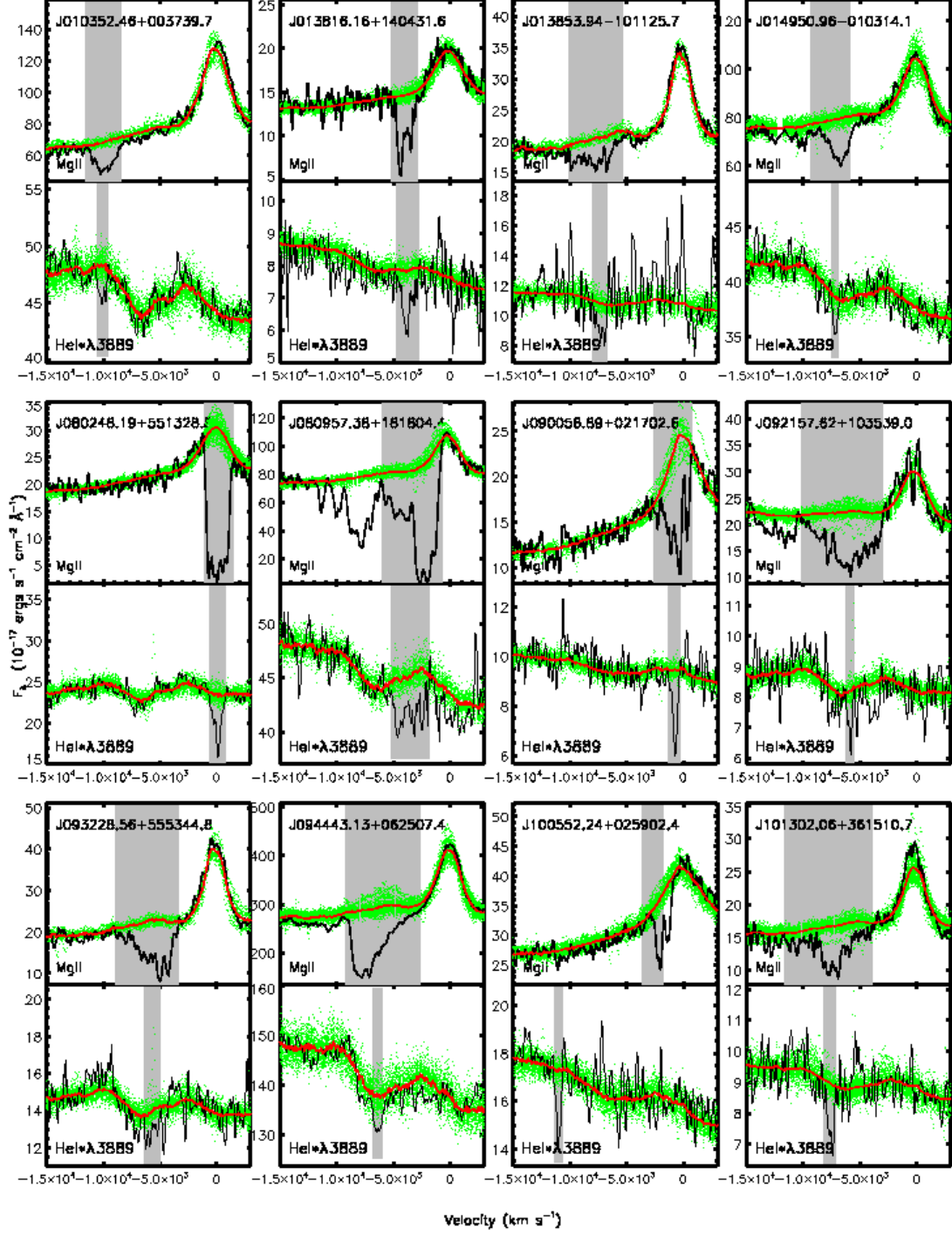
Fig. 32.— Demonstration of the spectral fitting of the 49 He I*λ3889 BAL quasars without a He I*λ3189 absorption line detected. The symbols are the same as Figure 31.

Velocity (km s⁻¹)
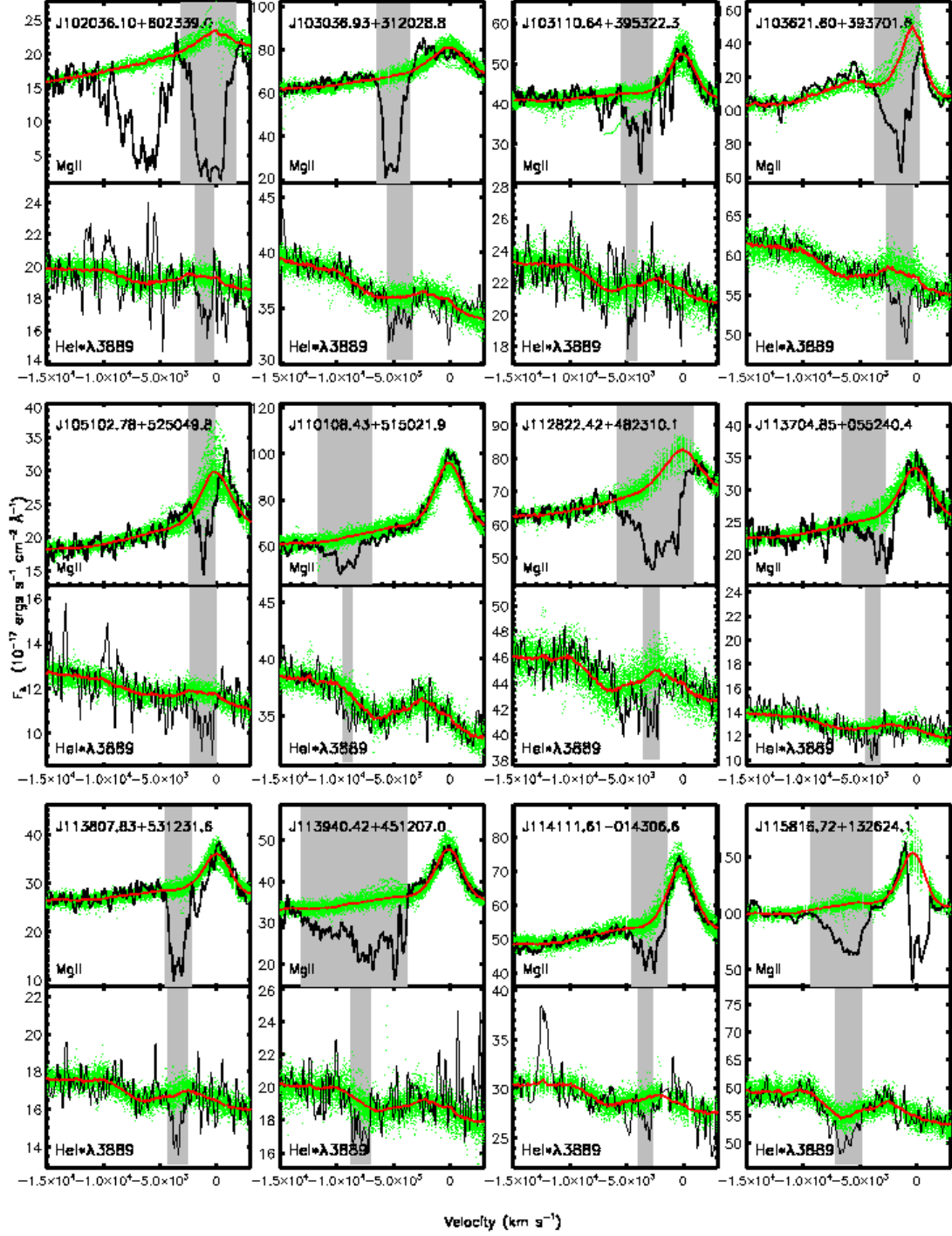
Velocity (km s^{-1})

F_λ (10^{-17} ergs s^{-1} cm^{-2} Å^{-1})

Velocity (km s^{-1})